

2015

NCREE

Research Programs and Accomplishments



May 31, 2016

National Center for Research on Earthquake Engineering
National Applied Research Laboratories

Contents

- 1 **Seismic Attenuation Structures in Southwestern Taiwan**
Strong Wen, Yizen Chang, Che-Min Lin and Kuo-Liang Wen
- 5 **The Monitoring of Crustal Activities in the Yun-Chia-Nan Area, Taiwan (II)**
Yizen Chang, Strong Wen, Yi-Ying Wen and Che-Min Lin
- 9 **An Important Update for the Engineering Geological Database for TSMIP**
Chun-Hsiang Kuo, Che-Min Lin, Kuo-Liang Wen and Hung-Hao Hsieh
- 13 **Shallow Shear-wave Velocity Structure of Strong-Motion Stations in the Kaohsiung-Pingtung Area Using Receiver Function Analysis**
Che-Min Lin , Chun-Hsiang Kuo , Jyun-Yan Huang , Ching-Chang Si and Kuo-Liang Wen
- 17 **Site Correction of a High-Frequency Strong-Ground-Motion Simulation Based on an Empirical Transfer Function**
Jyun-Yan Huang, Kuo-Liang Wen, Che-Min Lin and Chun-Hsiang Kuo
- 21 **In-plane Load Tests for Confined and Infilled Masonry Panels in Reinforced Concrete Frames with Eccentric Openings**
Yi-HsuanTu, Yu-Syuan Lin, Tsung-Chih Chiou and Lap-Loi Chung
- 25 **Seismic Evaluation and Fragility Curve of a Typical School Building**
Yeong-Kae Ye and Te-Kuang Chow
- 29 **Soil Gas Continuous Monitoring For Earthquake Precursory Studies**
Vivek Walia, Shih-Jung Lin, Arvind Kumar, Tsung-Han Jimmy Yang, Ching-Chou Fu and Kuo-Liang Wen

- 33 **Reliability Assessment of Using Equivalent Lateral Force Method to Estimate Elastic Seismic Responses with Accidental Torsion Effects**
Jui-Liang Lin, Wei-Chun Wang and Keh-Chyuan Tsai
- 37 **An Experimental Study of the In-Plane Cyclic Behavior of Low Aspect Ratio SC Wall Piers**
Chang-Ching Chang and Yin-Nan Huang
- 41 **Corrosion Hazard Map on Reinforcement of Reinforced Concrete Bridges in Taiwan**
Yu-Chi Sung , Chia-Chuan Hsu, Chian-Kuo Chiu
- 45 **Experimental Study on Post-tensioned Rocking Columns with Replaceable Energy Dissipaters**
Hsiao-Hui Hung, C. W. Huang, C. R. Jiang and P. X. Luo
- 49 **Experimental and Design Investigation of a Viscous Damper Filled with Shear Thickening Fluids**
Fang-Yao Yeh, Chung-Han Yu, Kuo-Chun Chang and Tsung-Wu Chen
- 53 **Reliability-based Design Method for Scoured Bridges**
Chun-Chung Chen, Chun-Jen Liu, Kuo-Chun Chang and Tsu-Chun Tseng
- 57 **Evaluating Current Installation Scheme for Viscous Dampers in Taiwan**
Wang-Chuen Lin, Shiang-Jung Wang, Jenn-Shin Hwang and Cho-Yen Yang
- 61 **Experimental and Analytical Study on Multiaxial Hysteresis Behavior of High-Damping Rubber Bearings**
Wang-Chuen Lin, Shiang-Jung Wang, Jenn-Shin Hwang and Cho-Yen Yang
- 65 **Experimental Study on Building Mass Damper Using Optimum Dynamic Response Control Algorithm**
Bo-Han Lee, Shiang-Jung Wang, Jenn-Shin Hwang and Kou-Chun Chang

- 69 **Development of Simplified Seismic Evaluation Program for Equipment in Hospitals**
Tzu-Chieh Chien, Juin-Fu Chai and Fan-Ru Lin
- 73 **Seismic Fragility Analysis of a Fire Sprinkler Piping System in a Hospital**
Fan-Ru Lin, Pei-Wen Hu, Chang-Chen Yeh, Juin-Fu Chai and Kuo-Chun Chang
- 77 **Modelling Contact and Collapse Behavior of Neighboring Trusses with VESEN**
Wei-Tze Chang and Shang-Hsien Hsieh
- 81 **A Study on Seismic Fragility of Water Distribution Reservoirs and Pipe Bridges**
Gee-Yu Liu
- 85 **Reconstruction of Geographic Information System Module**
Cheng-Tao Yang, Chin-Shun Yeh and Chi-Hao Lin

Seismic Attenuation Structures in Southwestern Taiwan

Strong Wen¹ Yizen Chang² Che-Min Lin³ and Kuo-Liang Wen⁴

、溫士忠¹、張議仁²、林哲民³、溫國樑⁴

Abstract

In this study, we adopt a damping least-square inversion method to investigate Qp and Qs structures of the crust in southwestern Taiwan. Previous studies have shown that the velocity structure can be used as an indicator of the geometry of a fault and the estimate of strong motion. Therefore, the goal of this research is to obtain the seismic attenuation structure and seismic characteristics of this area with respect to wave propagation. The distributions of Qp and Qs and their association with fault activities are also investigated. Our results indicate that variations in the velocity structure of southwestern Taiwan are caused by local geological structures, such as fault crossings. We also find that most earthquakes occur in areas that have greatly varying Qs gradients. In addition, through a simulation of strong earthquakes that have occurred in this area, the obtained 3D velocity structure can be more reliably utilized in seismic hazard assessments.

Keywords: Qp、Qs、complex structure、seismic attenuation

Introduction

In recent years, several major communications and transportation systems have been built in the Yun-Chia-Nan area (Figure 1) to improve its economic development. As such, it is extremely important to analyze the accumulation of seismic energy in the upper crust and the seismic potential of this area. In this study, we investigate with high resolution velocity structure in southwestern Taiwan and its seismic implications. Therefore, using the velocity structure and estimations of strong earthquakes, we want to explore the relationship between seismogenic zones and seismicity in southwestern Taiwan. In addition, we also expect to obtain useful information that will be of great significance for the prevention of earthquake-related disasters in this region.

The National Center for Research on Earthquake Engineering (NCREE) and the Central Weather Bureau Seismic Network (CWBSN) of Taiwan have set up seismic monitoring systems across Taiwan and its outlying islands. This dense seismic network and broadband seismometers have provided us with

high-quality waveform records for P- and S- waves which are necessary for this study. Not only have we been able to analyze this data to precisely determine earthquake locations, but we have also been able to obtain three-dimensional (3-D) models of seismic attenuation structures beneath this area. The Q values for the area of permeable heterogeneity are closely related; therefore, the 3D Q value is an important tool for studying regional geology. The degree of melting of plastic in the region, the nature of the rock, the broken water level, and so on, can then be determined, and then the locations of the potential geothermal area, broken belt, and igneous body can be identified. The obtained 3D Q model can provide a more comprehensive understanding of the complex geological structure. The results can also be used as a reference for the estimation of strong motion and the distribution of PGA in understanding the spatial and temporal variations in southwestern Taiwan.

Data processing

The Attenuation factor (Q) exhibits isotropic characteristics and a quantitative degree of seismic

¹ Associate Researcher, National Center for Research on Earthquake Engineering, scwen@narlabs.org.tw

² Assistant Researcher, National Center for Research on Earthquake Engineering

³ Associate Researcher, National Center for Research on Earthquake Engineering

⁴ Professor, Dept. of Earth Science, National Central Univ., wenkl@narlabs.org.tw

energy attenuation within a certain period. In a perfectly elastic medium, the Q value is infinite. Theoretically, Q values for a certain composition of the medium are a function of frequency. However, in a complex visco-elastic (composite viscoelastic) medium, the Q value in a particular frequency domain can be regarded as a constant. According to the seismic wave amplitude frequency equations in the amplitude spectrum (Scherbaum, 1990), the final value will include source effects, path attenuation effect, regional site effects and instrument effects that are multiplied in the frequency domain. The t^* value can be regarded as attenuating seismic operators in the propagation path. This study seeks to obtain 3D models of Q_p and Q_s values, so the ray paths should be distributed as evenly as possible throughout the study area and seismic data should be selected in appropriate conditions in order to improve the accuracy of the inversion results.

The selected conditions are as follows: (1) seismic data distributed from 22.9°N - 23.8°N and 120.1°E - 121°E ; (2) magnitudes must be larger than 1.5; (3) at least four stations must be recorded; (4) events with poor data quality and inaccurate earthquake location were to be deleted. For the Q -value attenuation tomography, the horizontal and vertical grid spacings are the same as mentioned in Wen et al. (2014), but with fewer data than used in the velocity tomography. In this study, short-period data are used, and we assume that the Q -value is independent of frequency in the band 1-20 Hz (Rietbrock, 2001).

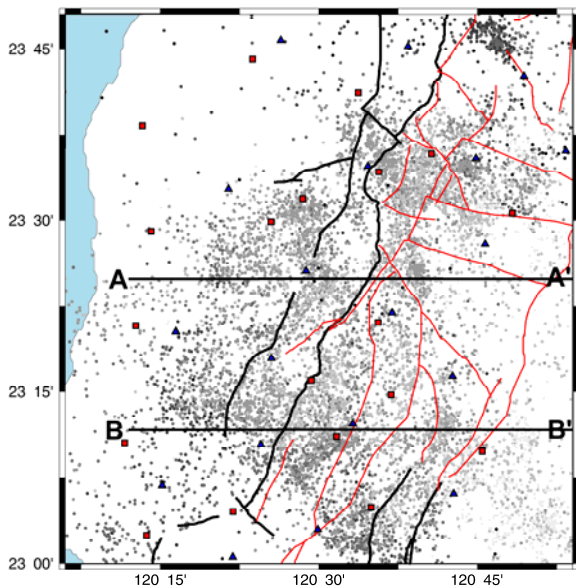


Figure 1. Locations of faults and stations of the CWBSN in our research area.

The t^* values are obtained from the P-wave and S-wave spectra using a standard method (Eberhart-Phillips and Chadwick, 2002; Hansen et al., 2004). We used short time-windows of approximately

2.5s and 4.5s, respectively, to limit the inclusion of noise. To avoid aliasing and side lobes on the spectra, we applied the Parzen window defined as follows:

$$W_j = 1 - \frac{[J - (N - 1) / 2]}{[(N + 1) / 2]}$$

where $J=0,1,\dots,N+1$

Here, W_j is the weighting factor and N is the total number of points. According to Al-Shukri et al. (1988), the spectrum using the Parzen window is smoother than that using a cosine window. Finally, 8021 t^* values are obtained from 2974 events, and are used for the inversion method to determine the Q_p and Q_s structures beneath the southwestern Taiwan.

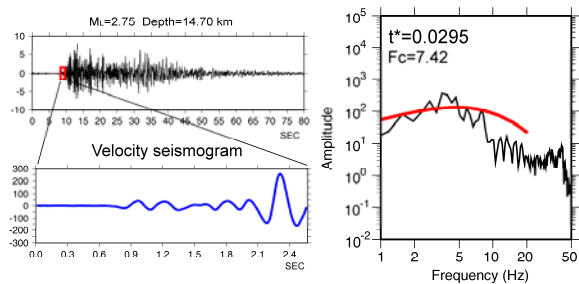


Figure 2. Example of obtaining the t^* value.

3D seismic attenuation model

This study uses waveform data from 2003 to 2011 recorded by the CWBSN and NCREC. A damping least-square inversion method was used to determine the Q_p and Q_s structures in the crust and upper mantle of the region. The programs and techniques used to perform the 3-D inversion were originally developed by Thurber (1983) and Eberhart-Phillips and Michael (1998), and have since been modified by others to obtain both the Q_p and Q_s values. The latitude and longitude ranges of our study area were 22.9°N - 23.8°N and 120.1°E - 121°E . Many seismic events have occurred in the region of interest. To improve the resolution of the tomographic inversion and achieve a uniform ray distribution around the volume source, we chose events with epicenter location errors of less than 5 km and events with more than four readings of the P- and S- waves. To ensure the quality of the seismic data, the ERH (error in the horizontal components) and ERZ (error in the vertical component) were set at less than 5 km and 10 km, respectively. We chose an *a priori* one-dimensional (1-D) Q model parameterized by horizontal layers of constant velocities that could roughly reproduce the main features of the known velocity structure obtained by Wang et al. (2009). An uneven 3-D grid formed through a trial-and-error process parameterized the 3-D structure. Several other cases were also taken into account during the

process: station spacing, estimated resolution, and the desired spatial resolution around the fault plane. The 1D initial attenuation model (Wang et al., 2009) couples with the grid node from the top surface to a depth of more than 75km into the inversion. The dimensions of the mesh were 7km x 7km. The effect of station elevation on the 3-D tomographic inversion was also considered in our calculations.

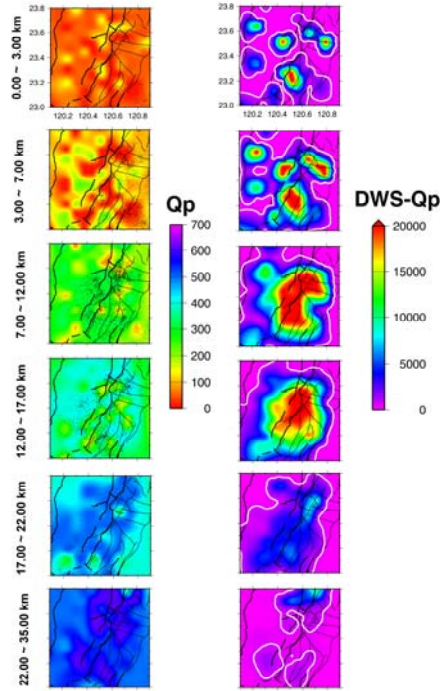


Figure 3a. DWS results for 3-D tomographic Q_p structures at four depth ranges (0-3km, 3-7km, 7-12km, 12-17km, and 17-22km). The black lines represent the locations of the main faults in the research area.

Results and Discussions

We discuss our results in two parts. The first part discusses the results in terms of how the attenuation structures were derived as well as presents an examination of ray density. The second part of our discussion involves examining attenuation structures in the profile. In order to do this for attenuation structures beneath southwestern Taiwan, we examined two profiles across this area (Figure 1). These profiles are almost perpendicular to the Chukou fault. Thus, we can outline the relationships between the attenuation structures, fault zones and seismicity. The derivative weight sum (DWS), which gives a measure of the density of rays that pass near a grid point, was used to estimate whether the distribution density of seismic ray paths was sufficient to resolve structural variations on the spatial scale defined by the nodal distances (Toomey and Foulger, 1989). As the distributions of the seismic events were observed uniformly, the results show high ray density in the selected zones, including the Chukou fault and in a band roughly 15 km wide running along the sides of

the fault (see Figure 3(a) and 3(b), the white solid lines are indicated as 500). However, the ray densities at depths from 0 to 3 km and from 22 to 35 km are relatively poor. At depths between 0 and 3 km, this problem may be due to the incident angles being almost perpendicular to the surface, meaning that the lateral resolutions of velocity are lower.

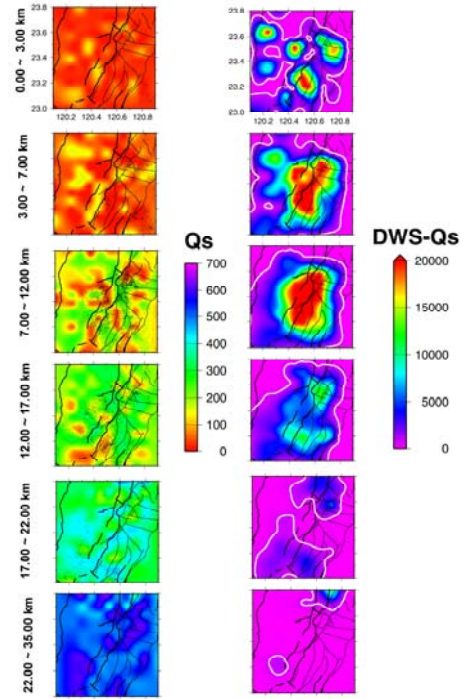


Figure 3b. The same as Figure 3(a), for Q_s .

Between 22 and 35 km, a reasonable explanation may be that only a few selected events actually occurred at such depths. The high resolution indicates that the seismic rays crossed most of the area, and ought to be reliable in helping to determine the geological structures more precisely beneath the Yun-Chia-Nan area.

Figure 3 shows numerous seismic events occurring in each layer. However, most are located in shallow layers at depths from 3 to 22 km. Therefore, in our inversion process, it is not possible to avoid cases where seismicity is not uniform. Between depths of 0 and 7 km, the high and low values of Q_p have a dispersed distribution. We also observed that there exist low Q_p anomalies scattered within the vicinity of the fault zone. At depths between 7 and 17 km, we found that the low Q_p anomalies increase with depth and expand in a southwesterly direction. This may be related to the existence of shallow sediment structures beneath this area (Ho, 1986). There are several cluster events in each layer and most lie within the high Q_p anomalies. In the vicinity of the fault zones, a low Q_s anomaly may be due to the increase in pore pressure, and therefore, the low Q_s anomalies decrease in the S wave velocity. We also observed that a low Q_s anomaly broadens from the Western Foothills to the Western Coastal Plain between 3 and 17 km, and that

the high Q_p zone extends to the Central Mountain Range (CMR) with increasing depth (see Figure 3). The likely reason for this is that rock formations are older and denser beneath the CMR, and so contain less fluid or SiO_2 , which leads to the high Q_p value. Our results indicate that most seismic events are located in areas with Q_s gradients that vary greatly or that have a high Q_s value.

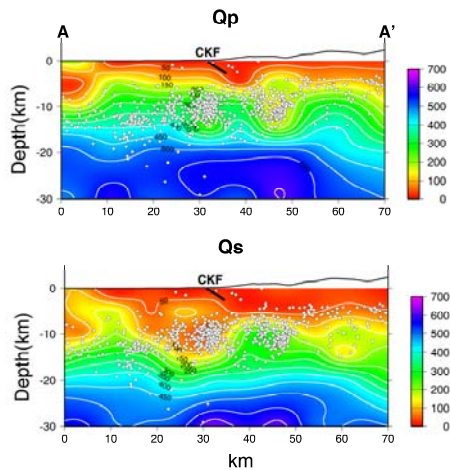


Figure 4. Tomographic Q_p and Q_s structures along the profile AA'. Circles represent events used in the inversion for this profile. "CKF" indicates the location of the Chukou fault.

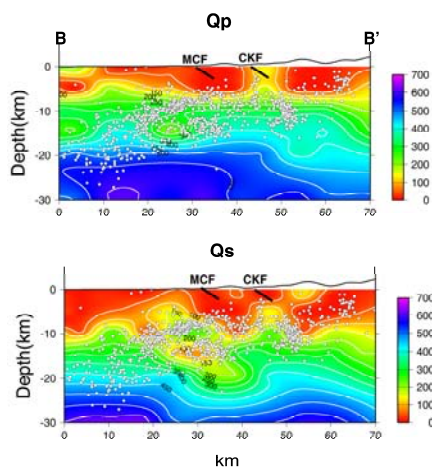


Figure 5. The same as Figure 4, for the profile BB'.

In Figures 4 and 5, the two profiles AA' and BB' (from Figure 1) show that the anomalies exist in the Q_p and Q_s cross sections, and potentially indicate an eastward leaning fault geometry beneath the Chukou fault zone, which implies the fault should be the Chukou fault. On the west side of the fault, there is also a low Q_p and high Q_s anomaly area, and this abnormal area tends to dip toward the west and exhibits an earthquake cluster. The earthquakes mainly occurred at the boundary between the high and low Q_s areas.

The possible reason for this is the impact of heat flow, which would result in a change from ductile to brittle, and thus increase the seismicity rate. We conclude that high seismicity occurs in zones that exhibit a low Q_p value and where the gradients of Q_s vary greatly in each profile. Hence, we can observe a seismic zone dipping toward the west and believe that this may be a blind fault zone that is worth further investigation.

Conclusions

In this study, we applied a damping least-square inversion method to investigate, via 3-D tomographic inversion, the Q_p and Q_s structures of the crust in southwestern Taiwan using body wave t^* data. We found that most earthquakes occurred in areas that have greatly varying Q_s gradients. This is because underground heat flow is a factor affecting low Q value variation and high attenuation of seismic energy, and the porosity of the fault, permeability of rock, the composition and the contained fluid pressure are all factors that affect the Q value. The 3-D numerical model from this study is an important factor in estimating strong motion and is of great significance in earthquake-related disaster prevention and mitigation.

References

- Al-Shukri, H., B. Mitchell, and H.A.A. Ghalib (1988). Attenuation of seismic waves in the New Madrid seismic zone, *Seismological Research Letters*, **59**, 133-140.
- Eberhart-Phillips D., M. Chadwick, 2002. Three-dimensional attenuation model of the shallow Hikurangi subduction zone in the Raukumara Peninsula, New Zealand, *J. Geophys. Res.*, **107(B2)**, p3-1-3-15.
- Ho, C.S. (1986). A synthesis of the geologic evolution of Taiwan, *Tectonophysics* 125, 1-16.
- Rietbrock A., 2001. P wave attenuation structure in the fault area of the Kobe earthquake, *J. Geophys. Res.*, **28**, Jan.
- Scherbaum, F., Combined inversion for the three-dimensional Q structure and source parameters using microearthquake spectra, *J. Geophys. Res.*, 95, 12, 423-12, 428, 1990.
- Thurber, C. H. (1983). Earthquake locations and three-dimension crustal structure in the Coyote Lake area, central California, *J. Geophys. Res.*, **88**, 8226-8236.
- Toomey, D. R., and G. R. Foulger (1989). Tomographic Inversion of Local Earthquake Data From the Hengill-Grensdalur Central Volcano Complex, Iceland, *J. Geophys. Res.*, **94**, 17,497-17,510.
- Wang, Y. J., K. F. Ma, F. Mouthereau and D. Eberhart-Phillips (2009). Three-dimensional Q_p - and Q_s -tomography beneath Taiwan orogenic belt: implications for tectonic and thermal structure, *Geophys. J. Int.*, 180, 891-910.

Monitoring of Crustal Activities in the Yun-Chia-Nan area, Taiwan (II)

Yi-Zen Chang¹ Strong Wen² Yi-Ying Wen³ and Che-Min Lin⁴

張議仁¹、溫士忠²、溫怡瑛³、林哲民⁴

Abstract

Due to the complicated geographic and geological conditions, various natural disasters have struck the Yun-Chia-Nan area over the years, especially very large earthquakes, which are caused by collisions between plates and have caused serious hazards. Therefore, understanding the relationship between seismic activity and seismogenic structures around this area is important. This study uses the seismic network of the National Chung Cheng University to monitor crustal activities in the study area. The physical properties of the crust here exhibit variation resulting from the effects of tectonic stress, especially before and after strong earthquakes. Several relevant physical parameters (e.g., velocity and attenuation) produce such variations, as mentioned in numerous studies. Therefore, in this study, the seismicity and focal mechanisms are analyzed to assess the seismic potential. Moreover, P-wave dispersive attenuation analysis is adopted to resolve the temporal changes in the media and assess the regional seismogenic process. The results for variations in physical parameters confirm the correlation between the observed data and earthquakes as well as assess the changes in the regional stress state. The results not only provide a better understanding of the seismogenic structure in southwestern Taiwan but also allow us to identify physical characteristics caused by cracks propagating in the stratum.

Keywords: seismicity, focal mechanism, dispersive attenuation.

1. Introduction

According to the report of the Central Geological Survey (2010 version), southwestern Taiwan contains a number of faults, including first-class active faults, such as the Chukou fault, Dajianshan fault, Meishan fault, and the Sinhua fault; and four other second-class active faults. Among the top ten disastrous earthquakes in Taiwan, which were recorded by instrumental observations from 1898 to 1997 (Zheng et al., 1999), five earthquakes occurred in southwestern Taiwan: the 1904 Douliu earthquake, the 1906 Meishan earthquake, the 1941 Zhongpu earthquake, the 1946 Sinhua earthquake, and the 1964 Baiho earthquake. Recently, some moderate earthquakes have also occurred in this area, including the 1998 Reuley earthquake, the 1999 Chiayi earthquake, the 2010 Jiasian earthquake, and the 2016

Meinong earthquake. These earthquakes had a magnitude of 6.0 or greater and caused considerable damage to houses and human lives.

Southwestern Taiwan can be divided into two main areas: the western foothills (WF) and the western coastal plain (WCP). The WFs are mainly composed of Neogene clastic sediments and partly Oligocene strata. The dominant rock types are an interlamination of sandstone and shale, with the thickness of the shale and mudstone layers increasing from north to south. The main tectonic structure of the WFs is a standard fold-thrust belt, an obvious imbricate system composed of dense, unbalanced folds and low-angle thrust faults dipping toward the southeast (Ho, 1988). The particular geographical environment and topography of the southwest area of Taiwan, which has produced a number of earthquakes, has a high seismic potential, especially with the majority of the

¹Assistant Researcher, National Center for Research on Earthquake Engineering, yzchang@narlabs.org.tw

²Associate Researcher, National Center for Research on Earthquake Engineering, scwen@narlabs.org.tw

³Assistant Professor, Dept. of Earth and Environment Sciences, National Chung Cheng University

⁴Associate Researcher, National Center for Research on Earthquake Engineering, cmlin@narlabs.org.tw

area being relatively soft plains, densely populated, and economically well developed.

Therefore, this study aims to monitor the crustal activities in southwestern Taiwan by analyzing the changes in regional stress using the focal mechanism of shear wave splitting and dispersive attenuation of P-wave. The results can serve as model parameters for simulation of 3D wave propagation.

2. Data and Methodology

Since earthquakes have occurred frequently in the Yun-Chia-Nan area and active faults exist near densely populated urban areas, in order to further understand the seismic activity in this area, this study cooperated with the National Chung Cheng University (CCU) to jointly monitor crustal activities through regular data collection and maintenance of seismic stations. In addition, waveforms were collected and used in the Antelope database system to obtain the first arrivals of P- and S-waves, and Hypo71 software (Lee and Lahr, 1972) was used to locate the earthquakes. For precise location, relocation errors were reduced using the double-difference location technique (or double-differences method; Waldhauser and Ellsworth, 2000), which is based on a comparison of P- and S-wave travel-time differences.

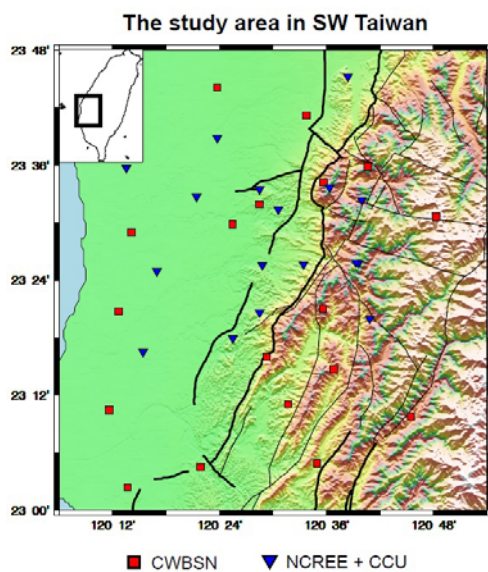


Figure 1. Station map showing the NCREE and CCU stations (blue triangles) and the CWBSN stations (red squares).

For seismography, this study adopted a 24-bit Guralp CMG-6TD broadband seismometer, which has a velocity-type sensor and provides 24-hour continuous recording at a frequency range of 0.03–50 Hz. The sampling rate was 100 points per second, which is different from that for free-field stations, allowing easy monitoring of small seismic activities.

In Figure 1, the red squares indicate the Central Weather Bureau earthquake observation network

(CWBSN) stations. Considering the CWBSN stations, fault locations, and seismicity distribution, this study cooperated with the CCU to deploy eighteen seismic stations, indicated by blue inverted triangles. This gave a good station coverage of the area improves earthquake location.

Figure 2 shows the combined seismic data from the NCREE, CCU, and CWBSN to relocate for the period October 2014 to June 2015. A total of 3817 earthquakes were recorded in this area and 1234 earthquakes were recorded from the local seismic networks (NCREE and CCU). In Figure 2, the dot size corresponds to the earthquake magnitude and the grey scale varies with the focal depth. Seismicity is densely distributed on the east side of the Dajianshan fault. From the topographic map shown in Figure 1, the Dajianshan fault exhibits arc patterns and is a reverse fault with a total length of approximately 25 km. To the south of the fault is the Chukou fault and to the west is the Chiuchungkeng fault and the Meishan fault; therefore, this region is a key area for monitoring. In addition, densely distributed seismic events in the Liuchia fault and the Lunhou fault in the southeast can be observed. The Lunhou fault belongs to the first-class active fault classification, as per the Central Geological Survey (2000 edition). Therefore, the southern part of the Chukou fault belongs to the Lunhou fault, giving a total length of 48 km and it is also a reverse fault.

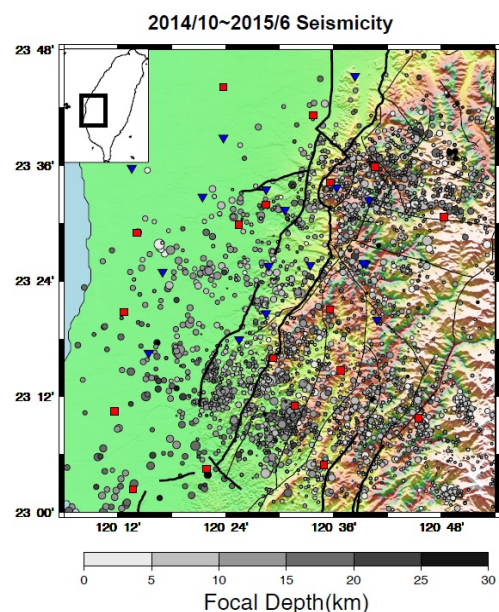


Figure 2. Seismicity map showing data from the NCREE, CCU, and CWBSN.

3. Focal mechanisms

In order to understand the regional tectonic faults, this study further calculated the focal mechanism. Because the energy of small earthquakes is less than

that of larger earthquakes, the station coverage is poor and the signal-to-noise ratio is relatively low; therefore, it is not easy to obtain the focal mechanism through the P-wave first-arrival technique. Hence, this study combined the data of the three networks to determine the fault plane solution and fill the gaps in station coverage.

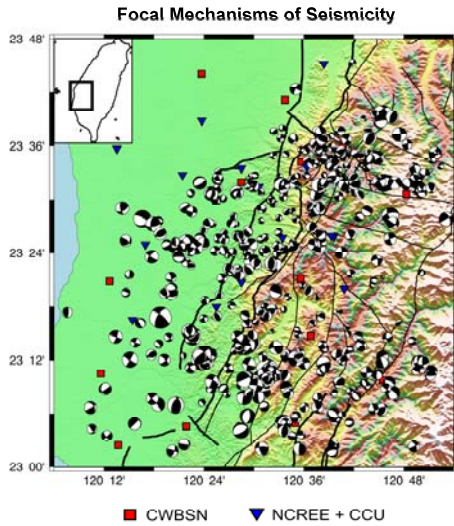


Figure 3. Distribution of focal mechanisms in the study area.

Figure 3 shows the focal mechanism of the earthquakes in the study area. A total of 524 fault plane solutions were obtained, with the normal and strike-slip faulting-type distribution in the WCP. Figure 4 shows triangular charts for the focal mechanisms at various depths (Forhlich, 1992, 2001). With a depth of 10 km in each plot, focal mechanism solutions were used to calculate the P, B, and T axis and their angles with respect to the horizontal plane were obtained. As a result, the P axis within 30° of the horizontal is defined as the normal fault; the B axis within 30° of the horizontal is the strike-slip fault; and the T axis within 40° of the horizontal is the reverse fault. These relationships are shown by the dotted lines in Figure 4. In the study area, the majority of earthquakes occurred at a depth of 5–15 km and less occurred at a depth of 20–30 km. Figure 4(b) shows the large number of reverse faults and strike-slip faults.

4. Dispersive attenuation

Figures 5 and 6 present the distributions of dQ for the year 2015 at the CHN5 and ALS stations, respectively. The red and green histograms indicate variations higher and lower than the average, which was calculated over two weeks; the blue histograms show dQ distributions for two weeks of the earthquake; the dotted line indicates a 15-day moving average; A–C are seismic events of $ML > 3.5$ that occurred within 40 km of the CHN5 station throughout the year 2015.

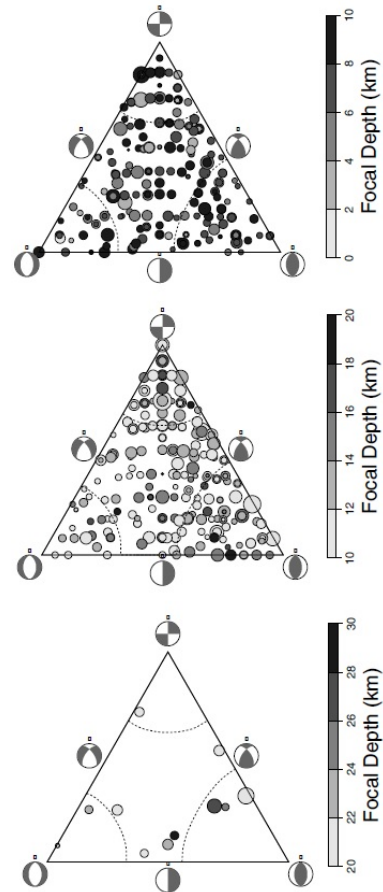


Figure 4. Triangular charts of the focal mechanisms for different depths.

The first cycle of the P-wave is sufficient to obtain information from the medium with little disturbance from other phase signals. The waveforms from small earthquakes were analyzed to obtain the temporal Q value, which is used to assess the changes in the regional stress and can serve as a short-term earthquake potential evaluation index (Wen et al., 2015). Dispersion, which is different frequencies propagating at different speeds. Ciz et al. (2006) indicated that the P-wave exhibits an obvious dispersion effect in the frequency band of 10^0 – 10^4 Hz; in this frequency region, velocity at different frequencies can be used to effectively sense medium changes, owing to the phenomenon of rock dilatancy.

Since the obtained Q values represent only a single path effect between a seismic event and the station, it exhibits directional characteristics. Based on this feature, the station was further used as a center point to divide the study area into east and west sides, as shown in Figures 5 and 6. Using the first cycle of the P-wave, interference by other waves can be effectively avoided, and compared with the calculation results from using the full waveform analysis, the focusing and defocusing effects would not influence the calculation. Therefore, the use of the P-wave first cycle provides more sensitive and efficient results. Compared with the topography map, the west side of CHN5 consists of relatively soft alluvium, which

could further attenuate the seismic energy and reduce the Q value. For the east side of CHN5, this part belongs to the central range area, and the Q value is relatively high. This difference reveals that dQ is more sensitive to the regional geological structure (see Figure 5).

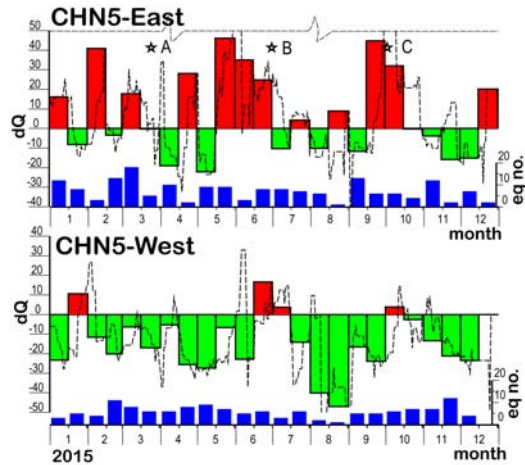


Figure 5. The dQ distributions for the CHN5 station, divided into two sides (east and west), to identify the anomalies.

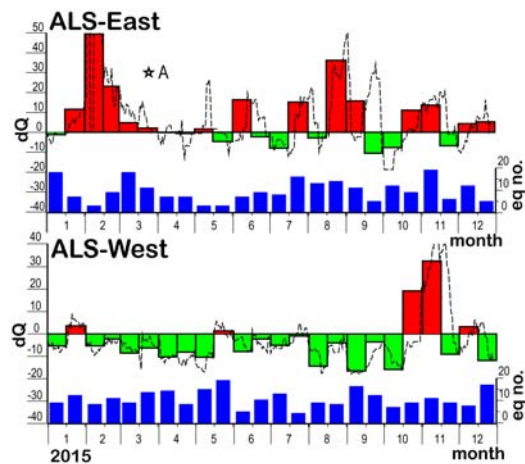


Figure 6. The dQ distributions for the ALS station, divided into two sides (east and west), to identify the anomalies.

5. Conclusions

This study used waveform data from 2014 to 2015, as recorded by the CWBSN, NCREC, and CCU seismic networks. Preliminary results for earthquake location and the focal mechanisms were obtained. These results indicated that the majority of earthquakes occurred in the area surrounding the Chukou fault, which also exhibited some small seismic clusters. From an analysis of the focal mechanism, it was determined that most earthquakes occurred at a depth less than 15 km and that the Chukou fault zone is of a thrust-faulting type. For the northern and southern segments, most seismic events exhibited strike-slip faulting, which may lead to the

complex fault structure beneath this area. For the coastal plain, more seismicity values exhibit normal and right-lateral strike-slip faulting, and this may be a result of the fault structures in the paleo-Tainan basin. Furthermore, the current evaluation method for the quality factor adopts P-wave dispersive attenuation to find relationship between the regional stress and seismicity. From the results of the CHN5 and ALS stations, the residual of the Qp value increases for some periods, indicating that the media in the crust were disturbed by the tectonic stress and a high seismic potential resulted.

References

- Ciz, R., Gurevich, B., and Markov, M. (2006), Seismic attenuation due to wave-induced flow in a porous rock with spherical heterogeneities. *Geophysical Journal International*, 165, 957–968.
- Frohlich, C., (1992) Triangle diagrams: ternary graphs to display similarity and diversity of earthquake focal mechanisms, *Physics of the Earth and Planetary Interiors*, 75, 193-198
- Frohlich, C., (2001) Display and quantitative assessment of distributions of earthquake focal mechanisms, *Geophysical Journal International*. 144, 300-308
- Ho, C. S., (1988) An introduction to the geology of Taiwan: explanatory text of the geological map of Taiwan, Central Geological Survey, MOEA, Taiwan Second edition pp. 192
- Waldhauser, F., and W. L. Ellsworth., (2000) A double-difference earthquake location Algorithm: method and application to the northern Hayward fault, California, *Bull. Seism. Soc. Am.*, 90, 1353-1368. doi:10.1785/0120000006
- Wen, S., Chieh-Hung Chen, Yu-Jhe Ji, Yi-Zen Chang, and Chau-Huei Chen (2015), The Seismogenic Deformation and Qp Temporal Variation before the M6.2 Mingjen Earthquake, Taiwan, *Journal of Asian Earth Sciences*, 114, 403-414,doi:10.1016/j.jseaes.2015.06.011.
- 鄭世楠、葉永田、徐明同、辛在勤，1999。台灣十大災害地震圖集，交通部中央氣象局地震測報中心，共 290 頁。

An Important Update for the Engineering Geological Database for TSMIP

Chun-Hsiang Kuo¹, Che-Min Lin¹, Kuo-Liang Wen², and Hung-Hao Hsieh³

郭俊翔¹、林哲民¹、溫國樑²、謝宏灝³

Abstract

The Engineering Geological Database for TSMIP was published several years ago. This database provides data regarding geological logging and velocities at 439 free-field strong motion stations throughout Taiwan. Precise Vs30 values were calculated using the measurements of the suspension PS-logging method at those stations, and therefore an essential site parameter is available for strong motion prediction equations, seismic hazard assessments, and the national seismic design code. However, there are more than 700 strong-motion stations in Taiwan. When site parameters become available for more strong motion stations, related studies will benefit from the site database. Therefore, although the investigation was closed in 2012, we continue the observation of velocity profiles. Velocity profiles at eighteen stations were added into the database, as well as the measured Vs30s. We assess the accuracy of the estimated Vs30s, which have been published in other studies using different proxy-based approaches; we also refer to the Vs30 selection criterion proposed by the NGA project. The estimated Vs30s from previous studies are then selected for stations without logging data in our database in order to complement the required site parameters for comprehensive usage of strong motion recordings in Taiwan. The updated site database currently contains Vs30 values at more than 800 stations for further studies. Moreover, another site parameter from recent studies, Z1.0, the depth of the velocity horizon with an S-wave velocity of more than 1.0 km/s, has been included in this database. The upgraded EGDT is used for national seismic hazard analyses.

Keywords: TSMIP; Vs30; Z1.0

Introduction

The National Center for Research on Earthquake Engineering (NCEE) of National Applied Research Laboratories (NARL) carried out an investigation on free-field stations in the Taiwan Strong Motion Instrumentation Program (TSMIP) with the Central Weather Bureau (CWB) from 2000 to 2012. A total of 483 stations were investigated, with 451 stations subjected to complete investigations including surface investigation, borehole drilling, and measurement of velocity. Only surface investigations were conducted at the other 32 stations for several reasons, such as the inability to transport the drilling equipment to the site or the denial of permission to drill from the land owner. Afterwards, the NCEE compiled the results into the Engineering Geological Database for TSMIP

(EGDT) and published a report (Kuo *et al.*, 2011a) and some papers (Kuo *et al.*, 2011b; 2012). Those publications provided important site parameters, empirical equations describing the S-wave velocity (Vs), and the characteristics of near-surface velocities. The site database has been the most important database for national seismic hazard assessments. Empirical Vs equations for Taiwan evaluated using the database have been prepared according to the national seismic design code.

Kuo *et al.* (2012) used the data from 469 stations from 2000 to 2010, of which 439 underwent complete investigation as mentioned above. Investigations in 2011 and 2012 (fourteen stations in total, with twelve complete investigations) were not included in the study. However, the empirical Vs equations are

¹ Associate Researcher, National Center for Research on Earthquake Engineering, chkuo@ncee.narl.org.tw; cmlin@ncee.narl.org.tw

² Professor, Dep. of Earth Science, National Central University and Division Manager, National Center for Research on Earthquake Engineering, wenkl@ncee.narl.org.tw

³ Assistant Researcher, National Center for Research on Earthquake Engineering, hhhsieh@ncee.narl.org.tw

unlikely to change significantly with the addition of data from these twelve stations. However, the V_s30 (the average V_s of the top 30 meters) at those stations can be further analyzed. Fifty-four stations have measured V_s profiles, but only at depths of less than 30 meters. Several of them have N (blow number of Standard Penetration Test) profiles longer than their V_s profiles. We converted these N values to V_s values to derive more V_s points at a site and adopted the Bottom Constant Velocity (BCV) extrapolation to calculate the V_s30 when the extended V_s profile is less than 30 meters. Site classification according to the criteria of the National Earthquake Hazards Reduction Program (NEHRP) is shown in Fig. 1.

V_s30 has been widely used in ground motion prediction equations (GMPE) and in seismic design codes. However, a site with a sedimentary depth larger than 30 meters cannot be recognized by this parameter, and therefore a parameter called Z1.0, the depth to which the velocity horizon of V_s is larger than 1.0 km/s, is adopted to account for the basin effect. Therefore, both the effects of soil stiffness and sedimentary depth are brought into the GMPEs via the V_s30 and Z1.0, respectively, and the GMPEs are able to account for site effects. We try to collect Z1.0 data from related studies to construct a more complete site database for strong motion stations. This may lead to further evaluation of GMPEs and other studies in Taiwan.

Review of Other Studies

This study aims to adopt V_s30 values estimated using surface geology, geotechnical data, geomorphology units, and ground slopes from existing publications. The site database of the Next Generation of Attenuation (NGA) project also used the estimated V_s30 s with appropriate consideration of uncertainties. Several studies analyzing seismic site conditions in Taiwan have been published since the 1990s. Earlier studies have only given site classifications but more recent studies also have V_s30 values. In recent years, the GMPEs have used a continuous site parameter, V_s30 , to represent the site effect rather than using only the site classification, such as rock and rock sites. Consequently, we conducted an examination by comparing the measured V_s30 values with estimated values from several studies (Wald and Allen, 2007; Chiou *et al.*, 2008; Lee and Tsai, 2008; Liu and Tsai, 2015) and decided the priority with which to include them in the EGDT database.

Wald and Allen (2007) calculated the topographic slope using digital data with a resolution of 30 arc seconds (around 900 meters) from the Shuttle Radar Topography Mission (SRTM30) and then developed two sets of correlations between topographic slopes and V_s30 values. A V_s30 map of the whole of Taiwan was also derived and can be downloaded from their website (Global V_s30 Map Server), in addition to the

digital data. In this study, this model is called W07 hereafter. Lee and Tsai (2008) used velocity profiles of 257 stations obtained from the EGDT and boring data of 4885 sites obtained from the Geo2005 database, which belongs to the Central Geological Survey (CGS) of Taiwan. They adopted a geological statistical approach as well as considering surface geological distributions to estimate V_s30 for free-field TSMIP stations, and evaluated a V_s30 map for the whole of Taiwan. The model is referred to as L08 hereafter. Chiou *et al.* (2008) used velocity profiles of 165 stations obtained from the EGDT, the elevation of the stations, and the third letter of Geomatrix's classification criteria, as well as considering previous site classification results (Lee *et al.*, 2001) to estimate V_s30 for stations that recorded the Chi-Chi earthquake sequence, and were therefore selected for the NGA database. The model is called C08 hereafter. The estimated V_s30 s from abovementioned studies are plotted in Fig. 2, together with subsequently measured V_s30 values reported by Kuo *et al.* (2012); this model is called K12 hereafter.

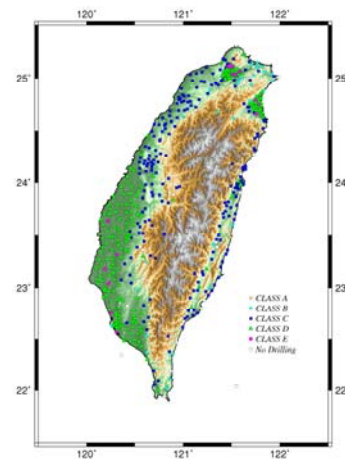


Fig. 1 Site classification according to the criterion of the NEHRP using the measured results.

Those stations that have both measured and estimated V_s30 values are plotted in Fig. 2 using symbols with different colors, as noted in the legend. The divergences between the observations and the three estimations of V_s30 are evident, but are proportional to the lower V_s30 values. Obvious horizontal linearities with an estimated V_s30 of 760 m/s, *i.e.*, the class B/C boundary, were found from models W07 and L08. This horizontal linearity is caused by a limitation in current methodologies using surface geology and topographic slope as proxies for V_s30 . These approaches cannot estimate V_s30 s larger than 760 m/s, which are found in hard rock and very hard rock sites. This reflects a global problem in estimating V_s30 for rock sites using common proxies, owing to the lack of measurements at hard rock sites. Hence, it remains difficult to evaluate reliable correlations between proxies and V_s30 . A similar restriction for the C08 model is more serious, where the upper-limit of V_s30 for the third letter of

Geomatrix's classification criterion of is around 660 m/s.

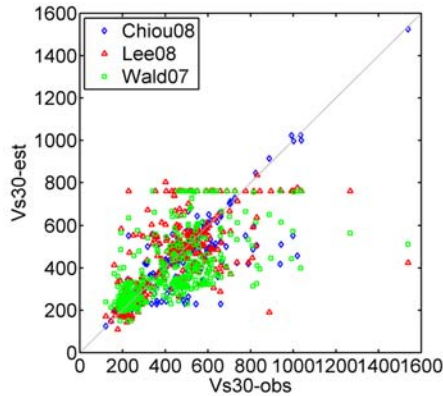


Fig. 2 Comparison between measured Vs30s using logging results (x axis) and Vs30s estimated by different methods (y axis).

Liu and Tsai (2015) recently evaluated the correlation between the inter-event residuals of their simple attenuation equation and the measured Vs30 values obtained from the EGDT, and then used the correlation to estimate Vs30 values for other stations without measured Vs30s. This model is referred to as L15 hereafter. The L15 model did not use EGDT data recorded in the last two years, however, so we are able to test the accuracy of this model using Vs30 values measured in 2011 and 2012. The comparison is shown together with the L08 and W07 models in Fig. 3. L15 shows a larger divergence compared to W07 and L08. L15 also overestimates the Vs30 values two or three times at two stations. Therefore, we did not include the results estimated by the L15 model in the site database to avoid large uncertainties.

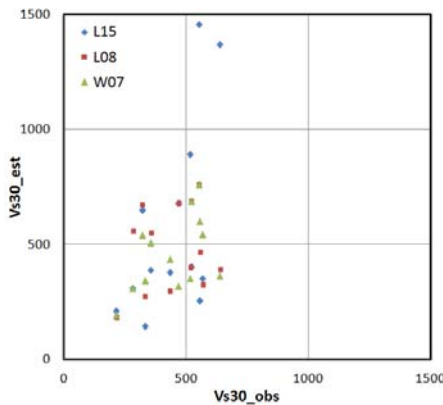


Fig. 3 Comparison of the estimated Vs30s of L15, L08, and W07 (y axis) and observations (x axis).

Extension of the EGDT

We further tested the accuracy of the W07, C08, and L08 models using a similar test as used for the L15 model. Here, we used later data that was not used

in the evaluation of the three models. W07 used EGDT data from up to 2005; C08 used data recorded until 2004; L08 used the data from up to 2005. Therefore, we could test each model using other data. The bias was defined as $\log(Vs30_{mea}/Vs30_{est})$ for each Vs30 value. Histograms of the bias distributions for the three models are shown in Fig. 4.

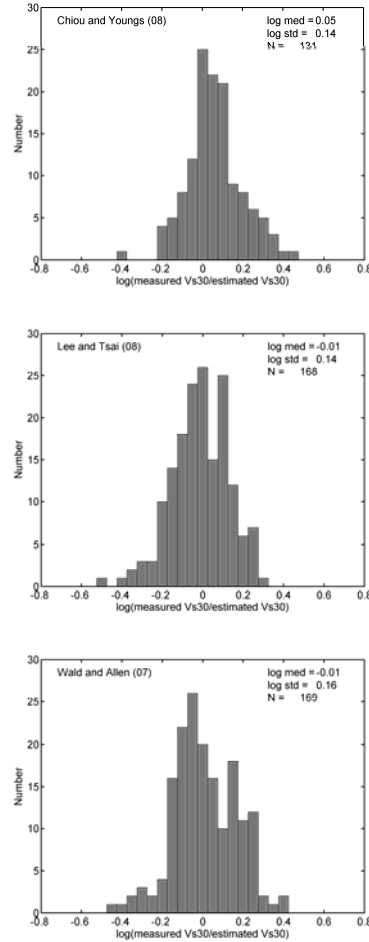


Fig. 4 Histograms of the bias distributions for the three major models.

The C08 and L08 models have similar standard deviations (0.14 in log scale), revealing the two models have similar accuracies. However, the C08 model seems to have a systematic underestimation based on the higher median value of the bias. In addition, this model only estimated Vs30 for those stations that recorded the Chi-Chi earthquake mainshock and aftershock sequences, because only these data were collected by the NGA database. The W07 model has a larger standard deviation of bias, indicating lower accuracy; however, this model has the largest density of Vs30 distribution because it was calculated using the 30-arc-second digital data. As a result of these considerations, these models are adopted in the following order of priority: K12 (measured Vs30), L08 (surface geology and geotechnical data as proxies), and W07 (topographic slope as a proxy).

The Z1.0 Parameter in Taiwan

A new site parameter, Z1.0, has recently been used to represent sedimentary depth, and thus the site terms used in the GMPE are able to account for both velocity (V_{s30}) and thickness (Z1.0), which are the main factors in site effect. However, this parameter is not easily obtained. It is currently only available in Japan, California, and some European countries. We are at present trying to derive and collect this parameter for Taiwan through borehole velocity profiles, and studies using non-invasive approaches. The Z1.0 is currently available for thirty stations where the V_s values were consistently larger than 1.0 km/s, and thus we can derive both the V_{s30} and the Z1.0 from those stations. Otherwise, a study of a shallow V_s analysis using the microtremor array method in the Western Plain of Taiwan provided Z1.0 values at around 40 strong motion stations (Kuo *et al.*, 2016). The Z1.0 values obtained from the EGDT, Kuo *et al.* (2016), and Lin *et al.* (2009) are respectively denoted with blue, black, and red symbols in Fig. 5. These results were plotted together, showing a regressive relationship (black curve). We believe that the pattern of data distribution in Taiwan is more like that of Japan than California.

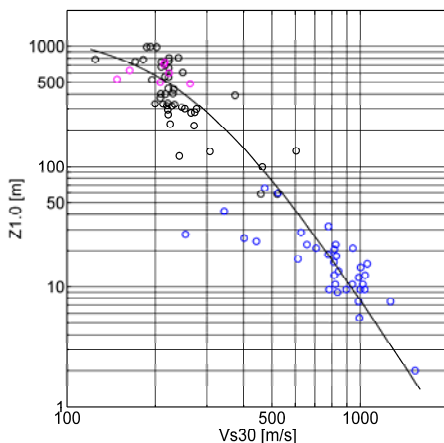


Fig. 5 The data distribution of V_{s30} and Z1.0 values at several stations in Taiwan as well as the relationship.

Conclusions

A completed site database will be very helpful for strong motion studies and seismic hazard analysis. In those stations that have V_s profiles of less than 30 meters, several stations have deeper N profiles that can be used to extend V_s profiles. The uncertainty of extrapolating the V_{s30} using the BCV method can be reduced with deeper V_s profiles. The V_{s30} s at a few stations changed slightly after adopting this modification. We collected estimated V_{s30} s from other studies (L08 and W07) for those stations without logging data. Although these two models have large uncertainties, we believe the estimated V_{s30} is still useful if the selection uses clear criteria. The EGDT

can provide V_{s30} values for all stations in Taiwan after the L08 and W07 models are incorporated. Otherwise, the Z1.0 parameter is available at seventy strong motion stations and ten other sites. The V_{s30} s are spread from 125 m/s to 1538 m/s, and the relationship between V_{s30} and Z1.0 for Taiwan was evaluated as shown in Fig. 5. The Z1.0 values at other stations can also be estimated using this relationship. The current objective of the EGDT is to provide V_{s30} and Z1.0 values for all stations in Taiwan. However, the current accuracy is not sufficient, especially for the Z1.0, because of the limited measured data available. We will continue introducing new data when it is available.

References

- Chiou, B. S.J., Darragh, R., Gregor, N., Silvad, W. (2008), "NGA project strong motion database", *Earthquake Spectra*, 24(1), 23-44.
- Global V_{s30} Map Server, U.S. Geological Survey, <http://earthquake.usgs.gov/hazards/apps/vs30/>.
- Kuo, C.H., Wen, K.L., Hsieh, H.H., Lin, C.M. and Chang, T.M. (2011a), "Study on the characteristics of near-surface velocities", NCRE-11-022, 82 pp. (In Chinese)
- Kuo, C.H., Wen, K.L., Hsieh, H.H., Chang, T.M., Lin, C.M., and Chen C.T. (2011b), "Evaluating empirical regression equations for V_s and estimating V_{s30} in northeastern Taiwan", *Soil Dynamics and Earthquake Engineering*, 31(3), 431-439.
- Kuo, C.H., Wen, K.L., Hsieh, H.H., Lin, C.M., Chang, T. M., and Kuo, K.W. (2012), "Site classification and V_{s30} estimation of free-field TSMIP stations using the logging data of EGDT", *Engineering Geology*, 129-130, 68-75.
- Kuo, C.H., Chen, C.T., Lin, C.M., Wen, K.L., Huang, J. Y., and Chang, S.C. (2016), "S-wave velocity structure in the western plain, Taiwan, derived by the microtremor array method". (Under review)
- Lee, C.T. and Tsai, B.R. (2008), "Mapping V_{s30} in Taiwan", *Terrestrial Atmospheric and Oceanic Sciences*, 19(6), 671-682.
- Lin, C.M., Chang, T.M., Huang, Y.C., Chiang, H.J., Kuo, C.H., and Wen, K.L. (2009). "Shallow S-wave Velocity Structures in the Western Coastal Plain of Taiwan", *Terrestrial, Atmospheric and Oceanic Sciences*, 20(2), 299-308.
- Liu, K.S. and Tsai, Y.B. (2015), "A refined V_{s30} map for Taiwan based on ground motion attenuation relationships", *Terrestrial Atmospheric and Oceanic Sciences*, 26(6), 631-653.
- Wald, D.J. and Allen T.I. (2007), "Topographic slope as a proxy for seismic site conditions and amplification", *Bulletin of the Seismological Society of America*, 97(5), 1379-1395.

Shallow Shear-Wave Velocity Structures of Strong-Motion Stations in the Kaohsiung-Pingtung Area Using Receiver Function Analysis

Che-Min Lin¹, Chun-Hsiang Kuo¹, Jyun-Yan Huang², Ching-Chang Si³ and Kuo-Liang Wen⁴

林哲民¹、郭俊翔¹、黃雋彥²、思靜章³、溫國樑⁴

Abstract

Kaohsiung City and Pingtung County are located in southern Taiwan and are bounded on the west side by several active faults. The shallow velocity structure of the thick alluvium basin in this area should be delineated to understand the seismic site effect of strong ground motion. The receiver function (RF) technique is a conventional method for studying the structure of the crust and the upper mantle beneath a seismometer. However, recently RF analysis of high-frequency acceleration seismograms has proven feasible for estimating shallow structures. This study applied the RF technique to the strong-motion records of almost one hundred TSMIP stations in the Kaohsiung-Pingtung area to estimate the shallow shear-wave velocity structures. The averaged RFs of all stations exhibit obvious variations because of different geologies and site conditions. After the forward modeling of RFs on the basis of a genetic algorithm (GA) search, the shallow shear-wave velocity structures beneath all the strong-motion stations in the Kaohsiung-Pingtung area were estimated to delineate the isovelocity contour maps of the main formation interfaces and produce a preliminary shallow 3D velocity model.

Keywords: Receiver Function, strong-motion station, shear-wave velocity, Kaohsiung, Pingtung

Introduction

Taiwan is the result of ongoing orogeny induced by complex arc-continent collisions between the Philippine Sea plate and the Eurasian plate. The active collisions frequently cause earthquakes and result in major tectonic features in and around Taiwan. There are several alluvium plains and basins, including the Western Coastal Plain, the Pingtung Plain, the Taipei Basin, and the Ilan Plain, that are filled with unconsolidated Quaternary sediment covering the bedrock. The obvious seismic site effect amplifies and extends incident seismic waves and can result in earthquake disasters. Therefore, a detailed three-dimensional (3D) velocity model, reflecting the real and complex seismic site effects in these areas, is necessary for ground motion simulation and prediction in Taiwan. Many 3D velocity models have been constructed using seismic tomography inversions in Taiwan. They are widely used to study seismic wave

propagations, source mechanisms, and site effects. However, the resolution of the shallow parts of these tomography models (within a depth of one or two kilometers) is not enough to reflect the alluvium plains and basins with low velocities because of insufficient and uneven seismic ray traces.

Over the next several years, the National Center for Research on Earthquake Engineering (NCREE) plans to combine several methods and data sets to construct a shallow 3D velocity model for Taiwan. The model will include detailed velocity distributions, depths of engineering and seismic bedrock, and other important site parameters to provide fundamental data for seismology and earthquake engineering. The aim of this study is to apply the receiver function (RF) technique to high-frequency acceleration seismograms recorded by Taiwan Strong Motion Instrumentation Program (TSMIP) stations, which are operated by the Central Weather Bureau (CWB), to estimate the

1 Associate Researcher, National Center for Research on Earthquake Engineering, cmlin@ncree.narl.org.tw

2 Assistant Researcher, National Center for Research on Earthquake Engineering, jyhuang@ncree.narl.org.tw

3 Assistant Technologist, National Center for Research on Earthquake Engineering, ccsi@ncree.narl.org.tw

4 Professor, Dep. of Earth Science, National Central University and Division Director, National Center for Research on Earthquake Engineering, wenkl@ncree.narl.org.tw

shallow shear-wave velocity structure in Taiwan's Kaohsiung-Pingtung area.

Local Geology and TSMIP Station

The Kaohsiung-Pingtung area includes Kaohsiung City and Pingtung County in southwestern Taiwan. It is located in the southern margin of the Western Foothills with exposed strata from the Pleistocene to the Holocene. The strata from the oldest to youngest are the Tashe Formation, the Gutingkeng Formation, the Lingkou Conglomerates, an accumulative formation, and recent alluviums. The main geological structures include the Tainan Anticline, the Chungchou Anticline, the Banpingshan Anticline, the Hsiaokangshan Fault, the Chishan Fault, and the Chaochou Fault. The activity of the Chishan Fault was classified as the first category by the Central Geological Survey (CGS). The Hsiaokangshan Fault and Chaochou Fault both belong to the second category of active faults. The Hengchun Peninsula, located at the southernmost part of the study area, is a southward extension of the Central Mountain Range. It is divided into the Hengchun Western Platform, the Hengchun Valley, and the Central Mountain Range, and it represents a part of the accretionary wedge of the Chinese continental margin above the eastward subducting South China Sea.

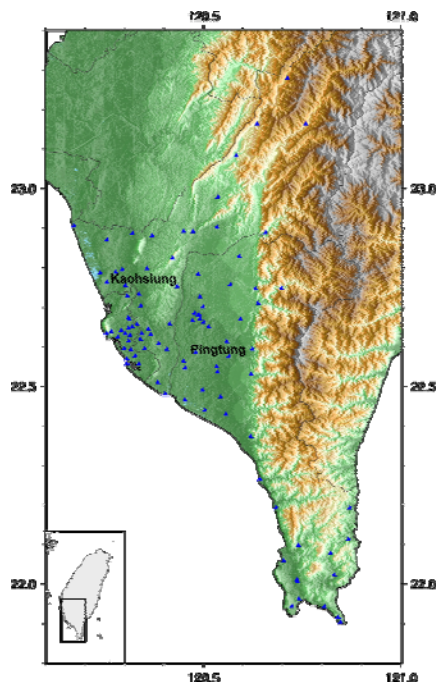


Fig. 1 Topographic map and the distribution of the TSMIP stations in Kaohsiung and Pingtung.

Figure 1 shows a topographic map and the distribution of the 100 TSMIP stations in Kaohsiung and Pingtung. Most of the stations are spread in the plain region, but there are also some stations located in the mountain region in the west. The dense network of TSMIP stations provides a large collection of

excellent seismic data for our study. The instruments installed at the stations are all tri-axial accelerometers. The data used are obtained from local earthquakes that occurred within or around the island of Taiwan between 1992 and 2012. Each waveform was visually inspected to eliminate recordings with low signal-to-noise ratios, anomalous glitches, and calibration issues. The selections of the P- and S-wave arrivals were also reviewed.

Receiver Function Analysis

The teleseismic RF method was developed to provide local information on S-wave velocity discontinuities beneath recording stations (Langston, 1979; Owen et al., 1984; Ammon et al., 1990). This method is excellent at showing clearly the converted phases used to estimate the depth of the discontinuities, even if the seismograms are contaminated by noise and scattering waves. The RFs of stations distributed over a region can efficiently estimate the 3D structures of that region. Because the largest S-wave velocity discontinuity generally coincides with the Moho, the RF method is a popular way to study the structures from the lower crust to the upper mantle. However, if sediments fill the site, the sediment-bedrock interface becomes a major velocity discontinuity. The waveforms from these receiver functions are predominantly controlled by the sedimentary structures within the first few seconds of the direct P arrival (Zelt and Ellis, 1998). As a result, the sensitivity of the RFs to variations in both the velocity and thickness of the surface layer increases dramatically. Julià et al. (2004) inverted the seismic velocities and densities for the sedimentary cover in the New Madrid Seismic Zone. The whole thickness of the Cenozoic and Cretaceous sediments within a depth of 1 km was estimated by performing an inversion of the RFs, computed at each individual broadband station. In Taiwan, RF analysis has been applied at the TSMIP stations in the Taipei basin and the Ilan plain to study shallow shear-wave velocity structures. The results proved that this method is an effective and convenient way to construct a sediment velocity model for a region that is densely populated with strong-motion stations and has numerous earthquake records.

In the RF analysis, all horizontal waveforms were converted to radial components and divided by the vertical component in the frequency domain of the Fourier spectra to derive the receiver functions. A Gaussian low-pass filter width of $a = 50$ and a water level of $c = 0.05$ were used in our analyses. Figure 2 shows all receiver functions of the station KAU051 in order of back-azimuth. Most receiver functions from KAU051 exhibit two apparent converted phases at 0.4 and 1.2 seconds. In the RFs, the systematic variation of converted phase waveforms versus ray back azimuth, and the appearance of seismic energy on both the radial and transverse components reflect the

existence of a dipping velocity discontinuity. After the selection of receiver functions with similar and reasonable waveforms, the average receiver functions for each station were calculated. The average of 17 RFs for KAU051 (Fig. 2) enhances the converted phases and reduces the inharmonic arrivals.

The average RFs of selected stations are shown in Fig. 3. The stations located in the plain region, where the sediment is deeper, show smaller converted phases with later arrival times. In contrast, the average RFs of the stations near or within the mountain region show earlier and more complex converted phases with high amplitudes. The variation of receiver functions with regard to location correlates closely with the surface geology of the study sites. This means that the RF analysis is also effective for the TSMIP stations in the Kaohsiung-Pingtung area.

In this study, a genetic algorithm (GA) was applied to search for the S-wave velocity model with the best fitness between the observed and synthetic receiver functions. GA search is a powerful global optimization method. The algorithm consists of selection, crossover, and mutation of individuals in a population and can search globally and locally for an optimal solution. Based on the geological, geophysical, and borehole data, we assumed a model with six layers covering a half space for the GA search. The shear-wave velocity and thickness of each layer are both variables in a range that was set. Figure 4 presents the results of the GA search for station KAU004 as an example. The results of the GA search show the effective convergence of the wide searching ranges (blue dash lines). The synthetic RF corresponding to the best model fits the observed one well.

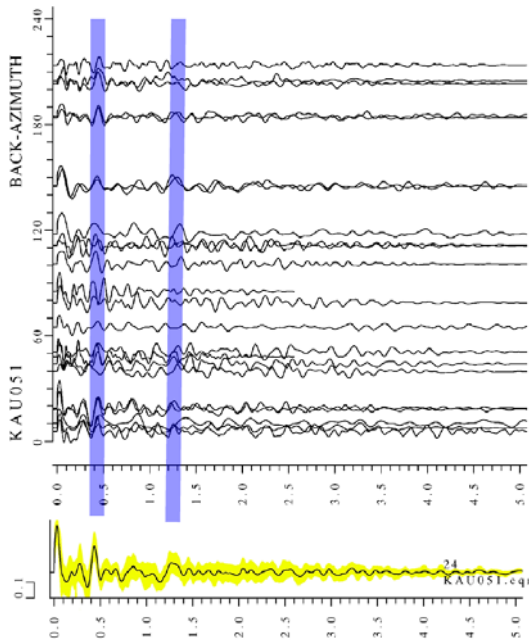


Fig. 2 RFs in order of back-azimuth (upper figure) and average RF (lower figure) of KAU051.

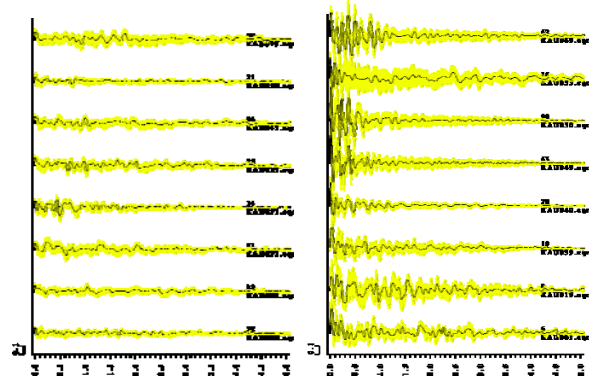


Fig. 3 Average RFs of the stations in the plain (left) and the mountain regions (right).

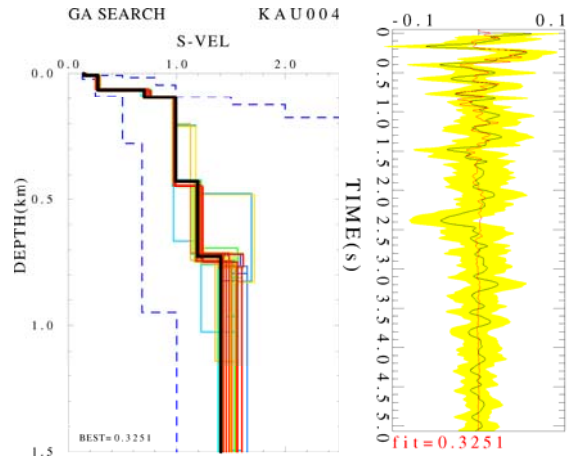


Fig. 4 An example of a GA forward search. The left figure shows 100 shear-wave velocity models with good RF fitness by the GA search. The black bold line is the best one. The right figure shows a comparison between the average observed RF (black line) and the best synthetic RF (red line).

Results and Discussion

In this study, the one-dimensional shallow shear-wave velocity structures of the TSMIP stations were estimated by RF analysis and forward modeling with a GA search. Based on these results, a velocity model can be estimated. Figure 5 shows an isovelocity contour map with shear-wave velocities reaching 0.5 km/s. This depth interface is comparable to the bottom of the first alluvium layer indicated by the previous study. Our result shows this velocity interface is deepest along the coast. In Kaohsiung City, it is mostly between 60 and 120 m and becomes shallower eastward. The depth is just a few meters between Chishan and Fongshan. However, the depth of the interface increases in the west part of the Pingtung plain, and then decreases slowly to the east. In the Hengchun Peninsula, the southernmost part of the study area, alluvium with a thickness about 30 m exists only in the Hengchun Western Platform. The entire mountain region has very thin surface alluvium. The variation of the bottom of the first alluvium layer

agrees well with the topography and the surface geology. Fig. 6 shows an isovelocity contour map with shear-wave velocities over 1.0 km/s. This interface represents the depth of the bedrock. The shear-wave velocities of stations located in the plain region reach 1.0 km/s at depths between 100 and 500 m, but this depth is just tens of meters for the stations located in the mountain region. The variation of this interface is similar to that shown in Fig. 5; however, the increase between Chishan and Fongshan vanishes. In addition, the depths with shear-wave velocities over 1.0 km/s in the Hengchun Western Platform increase to over 300 m from east to southwest because of the thick mudstone.

In conclusion, there is no obvious velocity contrast between the ground surface and bedrock to generate large converted phases of receiver functions in the plain region area because of the thick mudstone and conglomerate in Kaohsiung and Pingtung, respectively. However, we still can delineate the brief 3D shallow shear-wave velocity structure of this area well based on the RF analysis of the TSMIP stations. In the mountain region, near-surface velocity discontinuities, which generate early and large converted phases, were detected. The results show good correlation with the topography and geological structure and would be essential to conduct site-effect estimations, theoretical simulations of strong motion, and seismic hazard assessments.

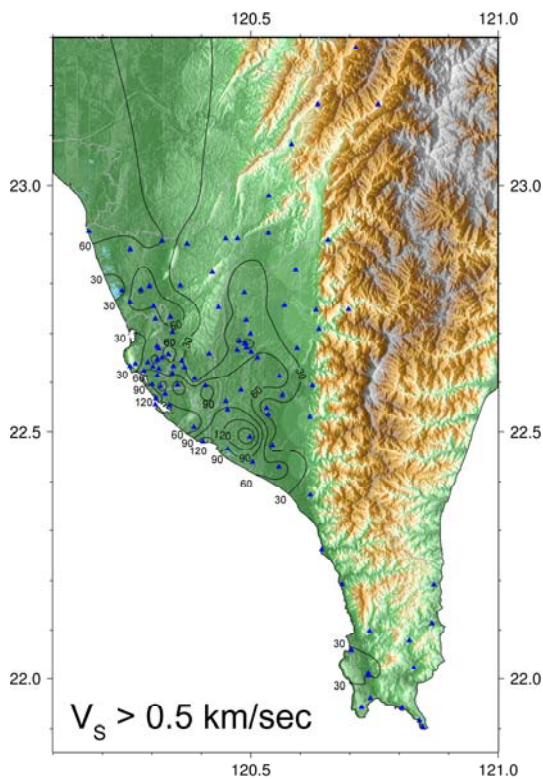


Fig. 5 Isovelocity contour (meter) map of the Kaohsiung-Pingtung area with shear-wave velocities over 0.5 km/s.

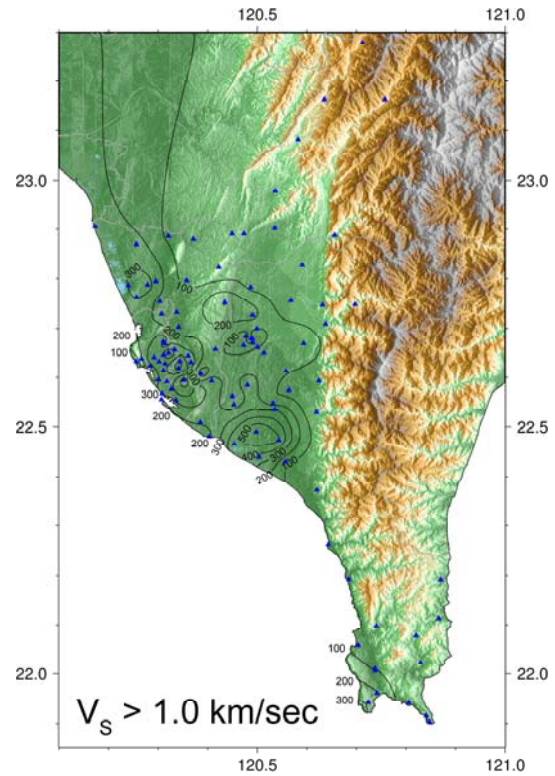


Fig. 6 Isovelocity contour (meter) map of the Kaohsiung-Pingtung area with shear-wave velocities over 1.0 km/sec.

References

- Ammon, C. J., Randall, G. E., and Zandt, G. (1990), "On the Non-uniqueness of Receiver Function Inversions," *J. Geophys. Res.*, 95, 15303–15318.
- Julià, J., R. Herrmann, B. C., Ammon, J. and Akinci, A. (2004), "Evaluation of Deep Sediment Velocity Structure in the New Madrid Seismic Zone", *Bull. Seism. Soc. Am.*, 94, 334–340.
- Langston, C. A. (1979), "Structure under Mount Rainier, Washington, Inferred from Teleseismic Body Waves," *J. Geophys. Res.*, 84, 4749–4762.
- Owens, T. J., Zandt, G., and Taylor, S. R. (1984), "Seismic Evidence for an Ancient Rift Beneath the Cumberland Plateau, Tennessee: A Detailed Analysis of Broadband Teleseismic P Waveforms," *J. Geophys. Res.*, 89, 7783–7795.
- Zelt, B. C., and Ellis, R. M. (1998), "Receiver Function Studies in the Trans- Hudson Orogen, Saskatchewan", *Can. J. Earth Sci.*, 36, 585–603.

Site Correction of a High-Frequency Strong-Ground-Motion Simulation Based on an Empirical Transfer Function

Jyun-Yan Huang¹ Kuo-Liang Wen² Che-Min Lin³ and Chun-Hsiang Kuo³

黃雋彥¹ 溫國樑² 林哲民³ 郭俊翔³

Abstract

This study constructs an empirical transfer function (ETF) for the difference in frequency spectra between the observed strong ground motion and the synthetic motion of a stochastic point-source approach (Boore, 1983; Boore, 2003) for the Taipei Basin, Taiwan. A database of shallow, small-magnitude earthquakes was selected to construct the ETF so that the point-source approach for synthetic motions might be made more widely applicable. Site corrections for high-frequency synthetic motion from the ETF procedure are made in the strong site-response area of the Taipei Basin. Finally, one of the most significant shallow large earthquakes (the 1999 Chi-Chi earthquake in Taiwan) is verified in this study. A finite fault stochastic simulation technique (Beresnev and Atkinson, 1998; Motezadian and Atkinson, 2005; Boore, 2009) is applied, owing to the complexity of the fault rupture process in the Taipei Basin, and the ETF-based site correction function is multiplied to obtain a precise simulation of high-frequency (up to 10 Hz) strong motions. The high-frequency prediction has good agreement in both the time and frequency domains in this study and it reached the same level as that predicted by the site-corrected ground motion prediction equation (GMPE, Jean et al., 2006; Chang et al., 2010; Lin, 2009).

Keywords: Stochastic ground motion simulation, empirical transfer function, site correction, Taipei basin

Introduction

Precise estimations of ground motion are valued in engineering seismology, and in practice the ground motion prediction equation (GMPE) is applied to each target site. The engineering approach is highly applicable to many different purposes, such as hazard analysis, structural seismic design, and disaster prevention. However, seismologists instead consider a wave propagation theory applied to one-dimensional, two-dimensional, and three-dimensional subterranean velocity structures in order to simulate the full waveforms at each target site. Strong site effects induced by sedimentary basins such as the Taipei Basin can already be considered in a three-dimensional simulation, but the reliable

frequency band is still less than 1 Hz, owing to shallow velocity structures not being sufficiently clear. The current technique cannot resolve the high-frequency (of at least 10 Hz) responses that are mainly induced by site effects.

To achieve a broad-band ground-motion simulation, the hybrid simulation technique was proposed and the stochastic ground motion simulation technique was proposed for high-frequency band. Most of the site responses used in the stochastic ground-motion simulation technique are simplified and only the rock-like response is considered. In this study, a site correction aspect in the stochastic simulation is considered to reduce the simulation errors. A small shallow earthquake database is used to

¹ Assistant Researcher, National Center for Research on Earthquake Engineering

² Division Head, National Center for Research on Earthquake Engineering; Professor, National Central University

³ Associate Researcher, National Center for Research on Earthquake Engineering

construct the empirical transfer function (ETF) and the 1999 Chi-Chi Taiwan earthquake was selected to verify the correction ability of the ETF.

The Taipei Basin, Taiwan, is greatly influenced by site effects during an earthquake. It has a triangular shape and the subsurface structure is deeper on the west side than on the east side. The deepest geological basement (the top of the Tertiary period) is located at around 680 m and the deepest engineering basement (the Sungshan formation) is around 100 m (Wang et al. 2004). The issue of seismic disaster prevention is quite important within the basin, as ground motions have been enlarged in historical earthquakes. For example, the Chi-Chi earthquake in 1999, even though the epicenter was 100 km away, still caused damage to over 450 houses. In a March 31, 2002, ML-6.8 earthquake, with an empirical distance also greater than 100 km, five people perished and over 250 people were injured in the basin, and it still caused more damage in the basin than in nearby regions. Therefore, in this study, a site correction for the Taipei Basin is applied to the stochastic simulation in order to reduce the uncertainties in high-frequency simulation.

In this study, a site correction technique from the ETF is applied to reduce the error in high-frequency simulations in the Taipei Basin from a stochastic point source and a finite-fault method. Regional parameters used here were well developed from previous studies for Taiwan. In order to highlight discussion of the error part from the ETF-based site correction method, this study use both time domain and frequency domain errors. The results showed that the correction method was useful and could reach the same level as the site-corrected GMPE. This method can also provide information on the site-corrected frequency spectrum. These results can help in the planning of disaster prevention measures for future earthquakes.

Construction of the Empirical Transfer Function

Strong motion data was selected from stations within the Taipei Basin (Fig. 1) from the database of the Taiwan Strong Motion Instrumentation Program (TSMIP) (Tsai & Lee 2005), with a time span from 1991 to 2012. As disastrous earthquakes are a priority for people, the ETF was first constructed from shallow earthquakes. Some 309 earthquakes (Fig. 1) with focal depths less than 30 km and magnitudes ranging from 1.8 to 6.0 were selected for the earthquake database in order to easily apply the point-source approach with a great quantity of records. Sokolov et al. (2009) discovered a significant difference between the site responses of shallow and deep earthquakes in the Taipei Basin, and said that this was due to different angles of incidence of seismic waves moving toward the basin edge. The target earthquake selected to verify our simulation was the 1999 Chi-Chi

earthquake in Taiwan. Only a shallow ETF was considered in this study.

The method of constructing the ETF has two stages. The first stage is including the simulated stochastic point sources of whole earthquakes in the database to a half space and adding the response of a layered structure for each individual station in order to extend the simulated spectrum into very hard rock (VHR). The second stage is dividing the spectrum into shear wave windows of observation and simulation to obtain the response between the site itself and VHR. Finally, averaging the spectral ratios of small earthquakes will complete construction of the ETF (diagram shown in Fig. 2, example waveform of constructed model bias shown in Fig. 3, example ETF shown in Fig. 4).

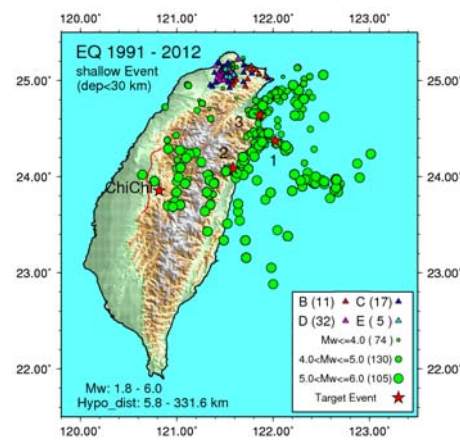


Fig. 1 Shallow earthquake data selected from the TSMIP database in this study. Triangles denote strong motion stations. Circles denote epicenters and magnitudes of earthquakes. Red stars denote target earthquakes used to verify the ETFs constructed in this study. The red line indicates the surface rupture during the 1999 Chi-Chi earthquake

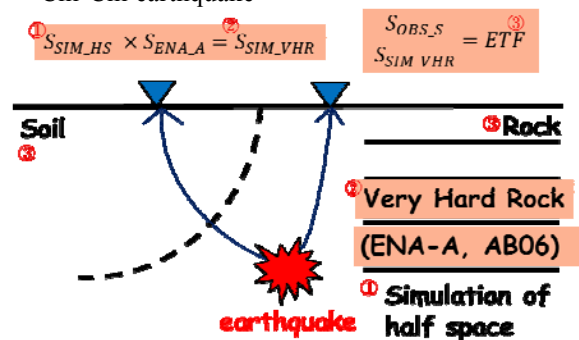


Fig. 2 Flow chart for construction of the ETF for a rock or soil site

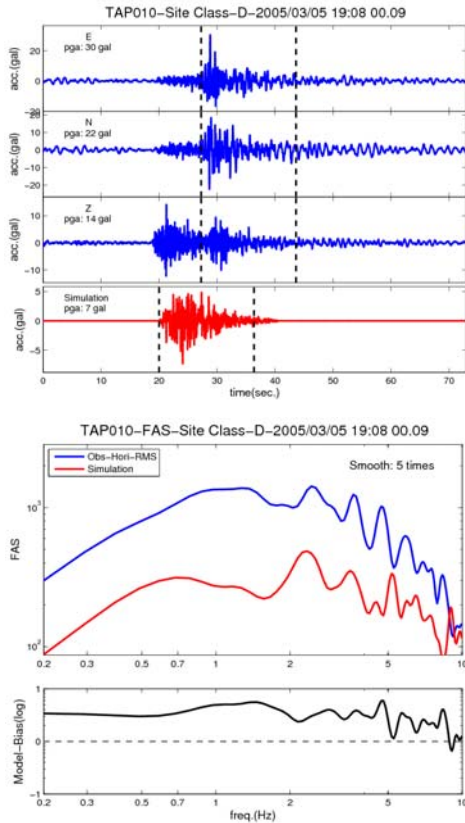


Fig. 3 Example waveforms for calculating model bias from a shear wave window

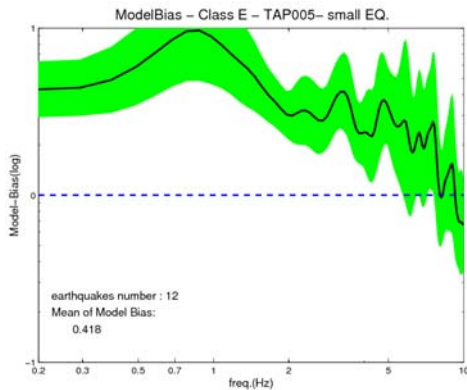


Fig. 4 Example ETF in the Taipei Basin, at TAP005, site class E, $V_{s30}=177\text{m/s}$

Results of ETF-based site correction method – example of the 1999 Chi-Chi earthquake

The finite-fault stochastic ground-motion simulation was applied to the 1999 Chi-Chi earthquake in Taiwan, owing to the complexity of its fault rupture system. A fault slip model with asperity distribution calculation was adopted from Ma et al. (2001) and is shown in Fig. 5. Results of site correction for the stochastic finite-fault simulation from the ETF based on shallow, small earthquakes (Fig. 6) show the spectra were slightly overestimated in the high-frequency band (5–10 Hz), regardless of the site classification. This means this phenomenon

was not due to site effects and might be because the energy contained in the high-frequency portion is lower in a large earthquake, as greater low-frequency waves are generated from a longer rupture process. The ETF based on shallow, small earthquake could not totally reflect the response of a huge earthquake, but prediction errors could be efficiently reduced using the DSPD and $\ln Err$ calculations (Fig. 7). The slightly higher PGA prediction results indicate that it is a conservative estimate of ground motion for disaster prevention purposes.

In general, results of PGA simulations from site correction using ETF can provide the same level of prediction as the site-corrected GMPE (J06&C10) and could produce acceptable spectrum fitting results (Figs. 7).

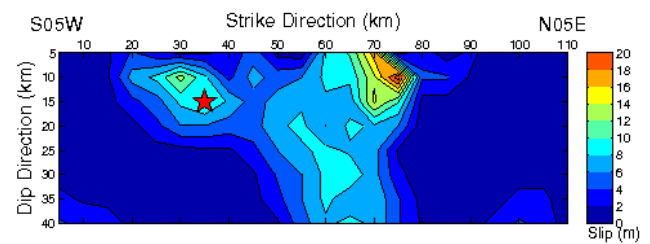


Fig. 5 Slip distribution of the Chelongpu fault during the 1999 Chi-Chi, Taiwan, earthquake. The star indicates the seismic source, and the fault strike is toward the N05E direction (redrawn from Ma et al. 2001)

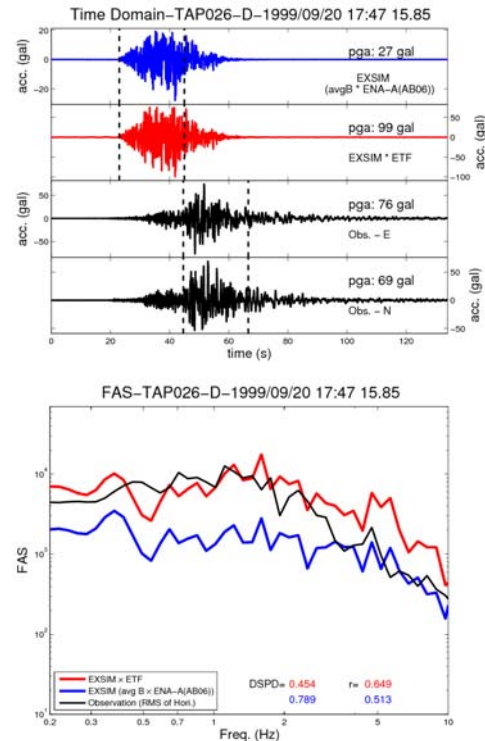


Fig. 6 Examples of ETF site correction for a stochastic finite-fault simulation of the 1999 Chi-Chi, Taiwan, earthquake.

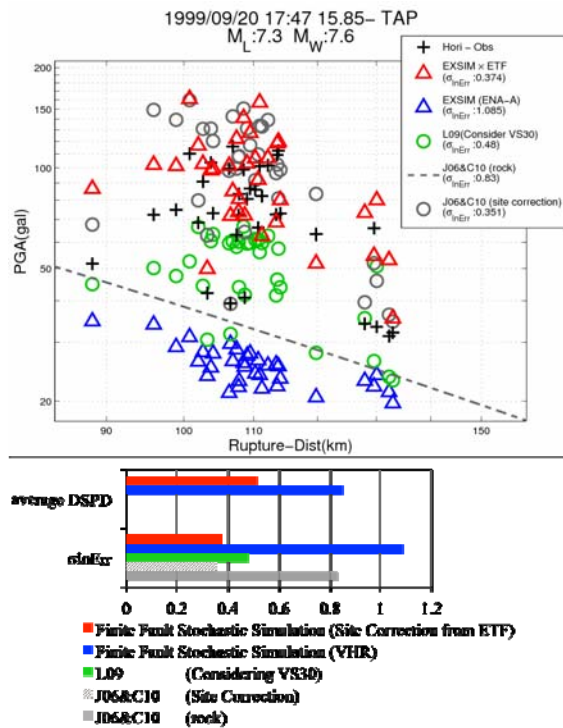


Fig. 7 PGA attenuation relation for the 1999 Chi-Chi, Taiwan, earthquake. and error comparisons in time and frequency domains

Conclusions

In this study, empirical transfer functions (ETF) were constructed based on a point-source stochastic simulation and observations from a database of shallow (<30 km), small ($M_w < 6.0$) earthquakes from Taiwan Strong Motion Instrumentation Program stations in the Taipei Basin.

The results of the ETF-based site correction of the stochastic strong-motion simulation showed good agreement in both the time and frequency domains when the depth and magnitude of a target earthquake suited the earthquake database. In addition, although the site correction function of a finite-fault simulation of the 1999 Chi-Chi, Taiwan, earthquake based on the ETF produced a slight overestimate in the high-frequency band, a conservative estimate can still be produced from the ETF-based site correction technique. It can also reach the same prediction level as the site-corrected ground-motion prediction equation. This means a theoretical calculation of strong ground motion, regardless of the peak ground acceleration or frequency domain, can aid in earlier planning of disaster prevention for individual fault systems in the future.

References

Beresnev, I. A., and Atkinson, G. M., "FINSIM -a FORTRAN program for simulating stochastic acceleration time histories from finite faults", *Seism. Res. Lett.*, 69(1), 1998, PP27-32.

Boore, D. M., "Stochastic simulation of high-frequency ground motions based on seismological models of the radiated spectra", *Bull. Seismol. Soc. Am.*, 73(6), 1983, PP1865-1894.

Boore, D. M., "Simulation of ground motion using the stochastic method", *Pure appl. geophys.*, 160, 2003, PP635-676.

Boore, D. M., "Comparing stochastic point-source and finite-source ground-motion simulations: SMSIM and EXSIM", *Bull. Seismol. Soc. Am.*, 99(6), 2009, PP3202-3216.

Chang, Y. W., Jean, W. Y., and Chiu, S. B., "Study on the design earthquakes for Kinmen, Matsu and Penhu areas", *Technical Report of National Center for Research Earthquake Engineering*, report number NCREE-10-016, 2010 (in Chinese with English abstract).

Jean, W. Y., Chang, Y. W., Wen, K. L., and Loh, C. H., "Early estimation of seismic hazard for strong earthquakes in Taiwan", *Natural Hazards*, 37, 2006, PP39-53.

Lin, P.S., "Ground-motion attenuation relationship and path-effect study using Taiwan data Set", PhD thesis, National Central University, Taiwan, 2009 (in Chinese with English Abstract).

Ma, K. F., Mori, J., Lee, S. J., and Yu, S. B., "Spatial and temporal distribution of slip for the 1999 Chi-Chi, Taiwan, earthquake", *Bull. Seismol. Soc. Am.*, 91(5), 2001, PP1069-1087.

Motezedian, D., and Atkinson, G. M., "Stochastic finite-fault modeling based on a dynamic corner frequency", *Bull. Seismol. Soc. Am.*, 95(3), 2005, PP995-1010.

Sokolov, V., Wen, K. L., Miksat, J., Wenzel, F., and Chen, C. T., "Analysis of Taipei basin response for earthquakes of various depths and locations using empirical data", *Terr. Atmos. Ocean.*, 20(5), 2009, PP687-702.

Wang, C. Y., Lee, Y. H., Ger, M. L., and Chen, Y. L., "Investigating subsurface structures and P- and S-wave velocities in the Taipei basin", *Terr. Atmos. Ocean.*, 15(4), 2004, PP609-627.

In-plane Load Tests for Confined and Infilled Masonry Panels in Reinforced Concrete Frames with Eccentric Openings

Yi-Hsuan Tu¹ Yu-Syuan Lin² Tsung-Chih Chiou³ Lap-Loi Chung⁴

杜怡萱¹、林育瑄²、邱聰智³、鍾立來⁴

Abstract

Four full-scale masonry panels in reinforced concrete (RC) frames were tested to investigate the influence of the opening and the type of masonry panel on in-plane seismic behavior. Test parameters of specimens were the construction method and the opening condition. Confined masonry panels failed in diagonal tension and infilled masonry panels failed in bed-joint sliding. Columns of specimens without opening failed in shear, and independent columns of specimens with openings showed flexural behavior. Behavior of both columns and panels and the interaction between columns and panels are affected by the opening condition and the construction method. The maximum strength and initial stiffness is higher for confined specimens and specimens without opening, and the maximum displacement has the opposite trend.

Keywords: Confined Masonry, Infilled, Opening, In-plane

Introduction

Seismic resistance of low-rise RC structures in Taiwan is usually governed by structurally weak directions. Masonry panels with eccentric openings are often found in these directions. These panels affect the failure mode of column and contribute to the stiffness and strength of the frame. Masonry panels could also be confined or infilled. Confined masonry panels are often found in old buildings, while infilled panels are more commonly used in modern buildings. The structural behavior and interactions between the column and these panels are different. Therefore, it is important to study the influence of the opening and the type of masonry panel.

Materials and Methods

Four full-scale specimens of masonry panels in RC frames were tested under a cyclic lateral load and a fixed vertical compressive load. The parameters of the specimens being tested are the construction method and the opening condition. Specimens CS and IS are

without openings on the panel and specimens CD-e and ID-e are with eccentric door openings. Two specimens with the same opening condition are confined and infilled, respectively. The size of the RC frame is 4500 mm × 3500 mm. The column section is 300 mm × 500 mm. Panels are 4200 mm × 3000 mm × 200 (thickness) mm and the opening width is 1000 mm. A three-cycle displacement-controlled lateral load with increasing drift was applied on the top beam. To simulate the shear building behavior, the RC beam of the specimen was controlled to remain horizontal during lateral loading. The axial load was fixed at 390.68 kN.

Test Results

The crack pattern of each specimen is shown in Fig. 1 and Fig. 2. The behavior of each specimen is concluded as follows:

Specimen CS behaved symmetrically in both directions. The diagonal crack of the confined masonry panel at the first stage controlled the maximum strength of the specimen. The diagonal crack also extended into

¹ Associate Professor, Department of Architecture, National Cheng Kung University

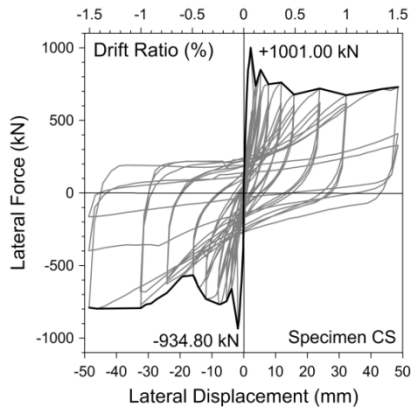
² Graduate Student, Department of Architecture, National Cheng Kung University

³ Associate Researcher, NCREC

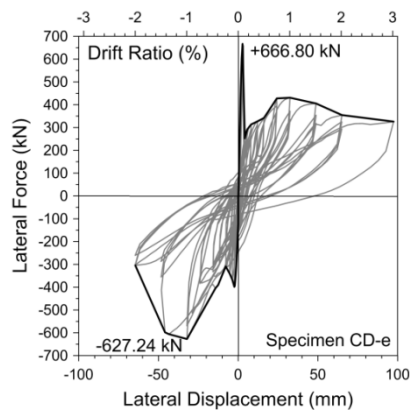
⁴ Division Head, NCREC

the top of the columns, and at a later stage, both columns failed in shear.

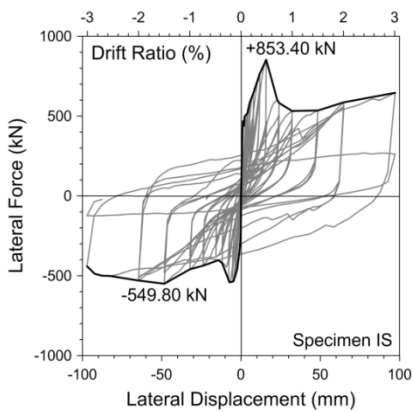
Specimen CD-e showed unsymmetrical behavior in both directions. When loaded in the opening direction, an initial crack appeared at the first stage and maximum strength was reached. The maximum strength in the other direction was reached later, as the diagonal toes of



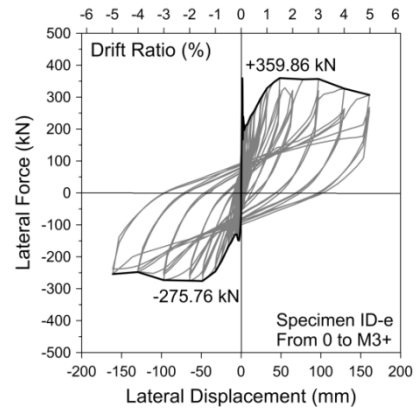
(a) Specimen CS



(b) Specimen CD-e

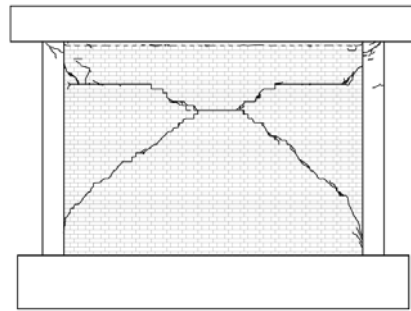


(c) Specimen IS

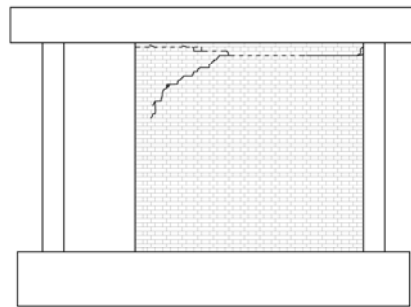


(d) Specimen ID-e

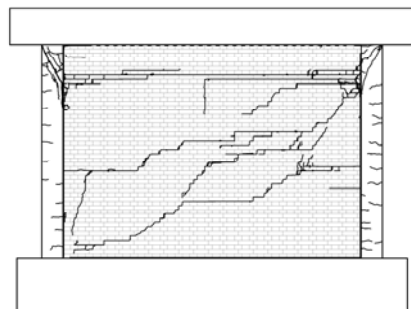
Fig. 1. Lateral force–displacement relationship.



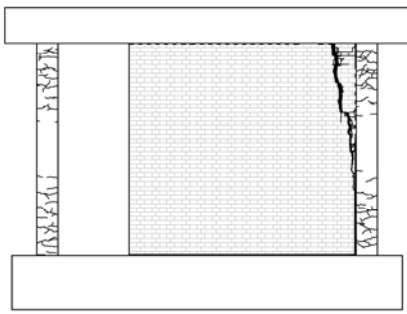
(a) Specimen CS



(b) Specimen CD-e



(c) Specimen IS



(d) Specimen ID-e

Fig. 2. Crack pattern at maximum strength.

the panel were crushed. The independent column of the specimen showed flexural behavior and only cracked, but the column near the masonry panel failed in shear at the end of the test.

Specimen IS first horizontally cracked near the top of the panel. A sliding zone appeared in the upper segment of the panel, and a short column effect developed. Then, a diagonal crack appeared in the lower segment of the panel. The panel contained a bed-joint sliding failure and the columns failed in shear.

Specimen ID-e also showed an unsymmetrical behavior. Since there was no boundary confinement on the opening side, the panel slid when loaded in the opening direction. Columns showed flexural behavior. Maximum strength was attained when columns reached flexural strength, and the panel had a bed-joint sliding failure. At the final stage of loading, the shear failure of the columns caused increasing axial compressive force on the panel. The rocking of the panel contributed to a distinctive increase in strength, as shown in Fig. 3.

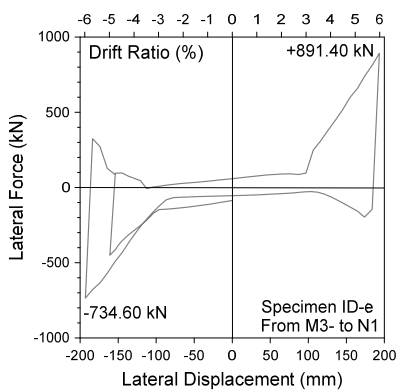


Fig. 3. Lateral load–displacement relationship of specimen ID-e at the final stage.

By comparing the lateral load–displacement relationship in Fig. 4 and the pictures of each specimen at the end of the test in Fig. 5, the behavior of all the specimens and the influence of test parameters can be concluded as follows.

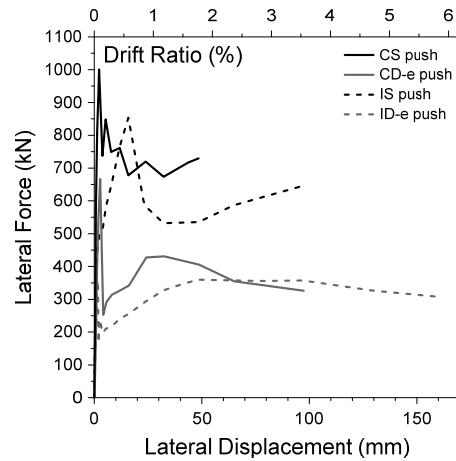
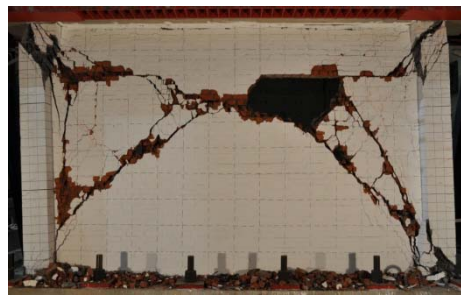


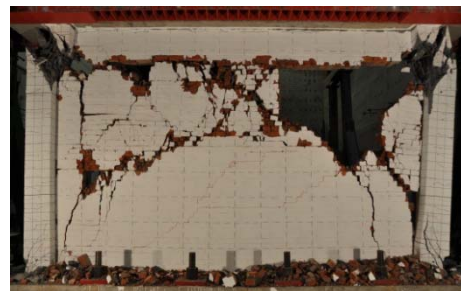
Fig. 4. Comparison of lateral load–displacement relationship of all specimens



(a) Specimen CS



(b) Specimen CD-e



(c) Specimen IS



(d) Specimen ID-e

Fig. 5. Pictures at the end of the test

1. Influence of the opening condition of the panel

When comparing specimens with the same construction method, the ultimate strength and initial stiffness of the specimen without an opening is much higher than that of the specimen with an eccentric door opening. However, the ultimate displacement and maximum displacement of the specimen with an opening are larger than that of the specimen without an opening.

The boundary condition of the masonry panel affects crack development remarkably. Both specimens without openings formed symmetric diagonal cracks. Both specimens with eccentric door openings cracked at the interface of the frame and the panel, and the panels slid toward the opening side instead of cracking diagonally.

2. Difference between confined and infilled masonry

When comparing specimens with the same opening condition, the ultimate strength and the initial stiffness of a confined specimen is higher than that of an infilled specimen. The ultimate displacement and maximum displacement of an infilled specimen are remarkably larger than that of a confined specimen.

In specimens without an opening, confined specimens diagonally cracked along the diagonal of the frame, but infilled specimens cracked along the diagonal below the sliding zone on top of the panel. This reveals that the column and the panel of confined masonry resist lateral force by forming a composite section, but an infilled panel and column tend to provide lateral resistance instead.

When comparing the two specimens with eccentric door openings, the sliding situations of panels were similar when the specimens were pushed. When pulling the specimens, the confined panel slid back to its original position and had a trend of forming a compressive strut, but the infilled panel did not slide back. The reason is that the friction between the top beam and the panel is lower, which is caused by the lower axial stress of the infilled panel.

Conclusions

1. The cracking path of panels is affected by the opening condition significantly.

2. The construction method affects the tendency to form a composite section within the column and panel.
3. Confined masonry panels failed in diagonal tension and infilled masonry panels failed in bed-joint sliding.
4. Failure modes of columns are affected by the opening condition and the construction method.
5. The maximum strength and initial stiffness of specimens without opening are higher, but the maximum displacement is smaller. Specimens with confined masonry panels have the same trend.

References

- Hsu, Y.-H., "Lateral Loading Experiments for Confined Masonry Panels with Different Opening Types", master's dissertation, Department of Architecture, National Cheng Kung University, 2015.
- Chao, Y.-F., "Experiment of In-filled Masonry Panels with Openings in RC Frames under In-plane Loading", master's dissertation, Department of Architecture, National Cheng Kung University, 2015.
- Chuang, T.-H., "Seismic Behavior of Slender Partially-Confined Masonry Panels Subjected to In-plane Force", doctoral dissertation, National Cheng Kung University Department of Architecture, 2013.
- G. Magenes and G. M. Calvi, "In-Plane Seismic Response of Brick Masonry Walls", *Earthquake Engineering and Structural Dynamics*, vol. 26, pp. 1091-1112, 1997.

Seismic Evaluation and Fragility Curves of a Typical School Building

Yeong-Kae Yeh¹ and Te-Kuang Chow²

葉勇凱¹、周德光²

Abstract

At present, pushover analysis based on the capacity spectrum method is often used for the detailed seismic evaluation of existing typical school buildings in Taiwan. The performance-target ground acceleration is compared with the site's peak ground acceleration (PGA) for a design earthquake with a 475-year return period in order to evaluate whether the seismic capacity is sufficient. However, as stated in FEMA 440, the results of the evaluation are too conservative for relatively short-period structures. In this report, incremental dynamic analysis (IDA) of a typical school building is used to study its seismic capacity and how conservative is the capacity spectrum method. Additionally, from the results of IDA, a seismic fragility curve of a sample school building can be built in order to evaluate the probability of collapse of this building under an earthquake with the evaluated performance-target PGA. From the analysis results, the roof displacement estimated by the capacity spectrum method is on average 2.25 times the value from nonlinear dynamic analysis for a typical three-story school building; under the performance-target earthquake for seismic evaluation, this structure has a 5.3% probability of collapse, which is acceptable, and the specified performance target is a reasonable and conservative choice.

Keywords: detailed seismic evaluation, nonlinear pushover analysis, capacity spectrum method, nonlinear dynamic analysis

Introduction

From the point of view of recent findings in earthquake engineering, the structural system and member details of old, existing buildings may lack sufficient ductility. In addition, due to aging of the materials, the seismic capacity may not meet the requirements of today's seismic design specifications. The seismic capacities of old buildings need to be examined to determine whether they need to be retrofitted or demolished. Currently, the most widely used detailed evaluation method is nonlinear pushover analysis, which aims to obtain the capacity curves of structures, that is, establishing the relationship between the base shear and roof displacement. Based on a building's performance needs, a performance point is set on the capacity curve and a design earthquake is sought that can cause this performance-point roof displacement, through the use

of the capacity spectrum method (ATC, 1996). This performance-target earthquake is represented by an associated design response spectrum and maximum ground acceleration.

The pushover analysis based on the capacity spectrum method is an approximation method to simulate the roof displacement of a structure, as calculated by nonlinear dynamic analysis. In the FEMA 440 report (FEMA, 2005), the capacity spectrum method of ATC 40 is noted to be too conservative for single-degree-of-freedom systems with periods less than 0.5 s. For a single-degree-of-freedom frame (Yeh and Chow, 2013) and for five-story and ten-story models (Yeh and Chow, 2014), we showed that the capacity spectrum method is very conservative for relatively short-period structures and is still conservative for the ten-story model.

¹ Research Fellow, National Center for Research on Earthquake Engineering, ykyeh@ncrec.narl.org.tw

² Assistant Technician, National Center for Research on Earthquake Engineering, tkchow@ncrec.narl.org.tw

In this paper, a real typical three-story school building is used as a sample structure to study how conservative is the detailed seismic evaluation. In addition, incremental dynamic analysis (IDA) (Vamvatsikos and Cornell, 2002) is used to study the seismic vulnerability of the sample structure, in order to evaluate the probability of each performance level as Immediate Occupancy (IO), Collapse Prevention (CP), and Global Instability (GI) under the intensity of a performance-target earthquake.

The third edition of the NCREE Technology Handbook (TEASPA) (NCREE, 2013) is used to define the nonlinear hinges of the structure, and the software package PERFORM3D is adopted to perform the nonlinear pushover analysis and the nonlinear dynamic analysis.

IDA procedures and fragility curves

To evaluate the seismic capacity of the structure, in addition to a detailed evaluation using nonlinear static analysis, one can also use a more accurate nonlinear dynamic analysis to perform IDA procedures. Through multiple sets of seismic records, the IDA curve can be defined and fragility curves can be established for each performance level, in order to study the probability of each performance level under specific seismic intensities.

IDA uses a series of nonlinear dynamic analyses with a gradually enlarged seismic intensity measure (IM) to calculate the damage measure (DM) of a structure until the occurrence of structural collapse. The relationship between DM and IM is the IDA curve. In this paper, $S_d(T_1)$ of the response spectrum with a 5% damping ratio is chosen as IM and the maximum inter-story drift θ_{max} is chosen as DM .

On the IDA curve, the performance points for IO, CP, and GI need to be specified as damage states in order to establish their fragility curves. If DM is less than IO, then there is no structural damage or minor damage, and residents can live there as normal. For old, non-ductile reinforced-concrete (RC) school buildings, θ_{max} is set as 0.5% for IO and all structural members have not yielded. If DM is less than CP, then the structure still has some safety and the collapse state has not yet been reached. For an old, typical RC school building such as the sample structure, θ_{max} equals 1.75% for CP or, if the point's slope on the IDA curve is 20% of the initial slope, then the smaller value is chosen for CP. If DM reaches the GI level, the structure is unstable and on the verge of collapse. In this research, GI is defined as structural strength being decayed and stiffness being reduced to less than 50% of the elastic stiffness.

Ideally, if we can find an IM parameter to specify the seismic intensity, then various earthquakes with the same IM value will cause the structure to have the same DM response. In reality, however, there is no

such IM parameter. Instead, corresponding to each input seismic intensity IM_i , the structure has a response of DM_i , with values lying in a probability distribution. Vulnerability analysis is required to evaluate the structure's performance.

The function of the fragility curve is represented by a cumulative distribution function (CDF):

$$P[DM \geq C / IM = IM_i] = \Phi\left(\frac{\ln(IM_i) - \mu}{\beta}\right) = \int_0^{IM_i} \frac{1}{z\beta\sqrt{2\pi}} e^{-\frac{(\ln z - \mu)^2}{2\beta^2}} dz \quad (1)$$

where μ is the log mean of IM_i and β is the log standard deviation of IM_i .

Twenty observation points of IM_i for each performance level IO, CP, and GI can be gained from the derivation of the IDA curves. Then, according to the maximum likelihood estimation (MLE) method (Lallemant, Kiremidjian, and Burton, 2015), the fragility curves of every performance level can be defined.

Seismic evaluation of a typical three-story school building

A typical three-story school building was chosen from the NCREE report, Technology Handbook for Seismic Evaluation and Retrofit of School Buildings (NCREE, 2013), and it is an old non-ductile RC structure. The period of the dominant mode in the x -direction of this system is 0.6565 second, and the modal mass coefficient is 89.21%. Under a controlled force, a vertical loading is applied, and then, under displacement control, lateral loadings are applied to the centers of every floor. The vertical distribution of the lateral loadings is according to the dominant mode. The relationship between base shear and roof displacement is recorded to form a capacity curve. We assume the structure is located in the eastern region of Tainan City and that the ground is class-2. Its short-period and one-second-period design spectral acceleration coefficients S_{DS} and S_{D1} are 0.7 and 0.52, respectively. With a roof displacement of 8.03 cm as the performance target, the performance-target acceleration A_p is calculated to be 0.216 g from the capacity spectrum method.

Seismic vulnerability analysis of the typical three-story school building

Prior to dynamic analysis, we need to choose the input seismic records. From the geophysical database management system of the Central Weather Bureau (<http://gdms.cwb.gov.tw>) and the engineering geological database for TSMIP of the NCREE (<http://egdt.ncree.org.tw>), we chose twenty seismic

records. Their seismic intensities are larger than 6 and their seismic stations are all located on class-2 ground. These twenty seismic records are the input earthquake samples for the IDA. Figure 1 shows the 5% damping response spectrum of these sample records, the median, and 84% fractile. For each sample record, its IDA curve is established from IDA analysis.

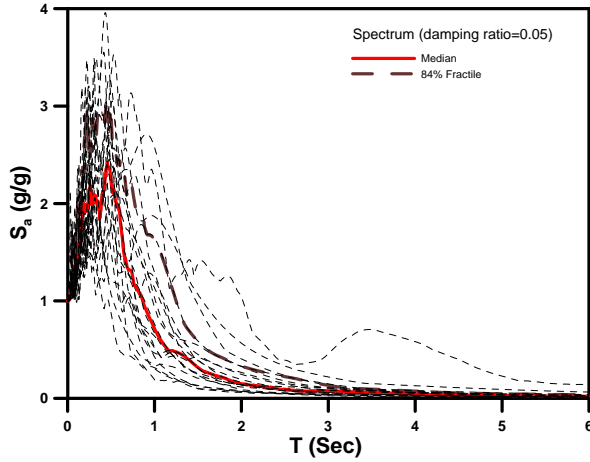


Fig. 1 Response spectra of twenty sample records.

The IDA curves of the twenty sample records are shown in Fig. 2. We set the (DM, IM) coordinates of IO, CP, and GI on each IDA curve according to the definitions of each performance level. From these twenty pairs of IM and DM values, we can establish fragility curves for each performance level, as shown in Fig. 3. From these fragility curves, we can calculate the probabilities of each damage state for a specified seismic intensity IM .

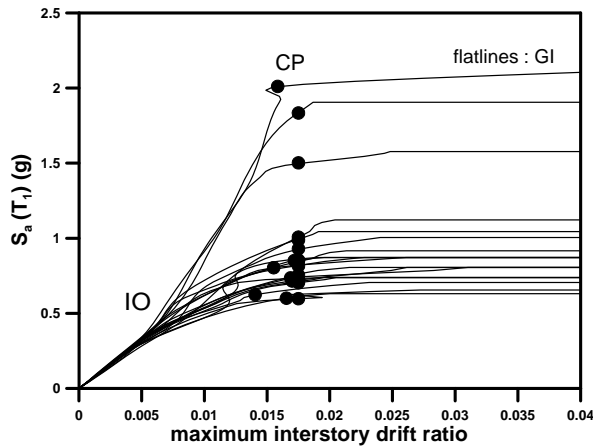


Fig. 2. IDA curves and performance points

The allowable probabilities for each performance level for each building make it difficult to have an objective standard. The United States PEER Center design criteria for tall buildings recommended that, at the maximum considered earthquake (MCE) level, a collapse or unstable state of a new designed building should have a low probability of occurrence, which can be set at around 10%.

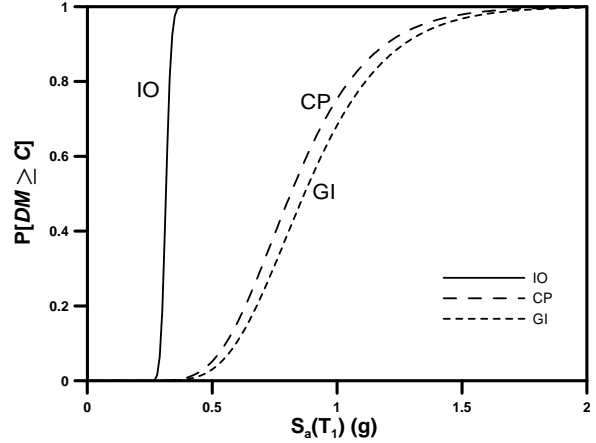


Fig. 3. Performance levels and fragility curves

Table 1. The probabilities of damage states of the typical three-story school building

	475-year design earthquake	Performance target earthquake
$P[DM \geq IO]$	100.0%	100.0%
$P[DM \geq CP]$	30.7%	8.5%
$P[DM \geq GI]$	23.2%	5.3%
$P[DM < IO]$	0.0%	0.0%
$P[IO \leq DM < CP]$	69.3%	91.5%
$P[CP \leq DM < GI]$	7.6%	3.2%

According to previous seismic evaluation procedures, a typical three-story school building located in the east region of Tainan City on class-2 ground has a performance-target acceleration of 0.216 g, which is less than PGA value of a design earthquake with a 475-year return period. Therefore, the seismic capacity of this sample structure is insufficient and it needs to be retrofitted or demolished. The IM value of a design earthquake with a 475-year return period in the east region of Tainan City on class-2 ground is specified as $S_a(T_1) = 0.7g$, and the corresponding occurring probabilities for each damage state are shown in Table 1. The probability of the GI unstable state is 23.2%, which is a slightly higher value; the probability between the CP and GI states is 7.6%; and the probability of no damage, which is less than IO, is 0%, so the structure being evaluated for retrofitting is considered reasonable. The IM of the evaluated performance-target earthquake is $S_a(T_1) = 0.216 \times 2.5 = 0.54g$, and the calculated probabilities of each damage state are shown in Table 1. The probability of the GI unstable state is 5.3%, which is less than 10% and thus lies in the acceptable range, so the performance target is a reasonable choice. The probability between the CP and GI states is 3.2%. The probability of no damage, which is less than IO, is 0%. The probability between the IO and CP states is 91.5%, which matches the assessment criteria for

moderate damage from a performance-target earthquake.

the Safety Factor of the Capacity Spectrum Method on Multi-Storey Structures”, NCREE report NCREE-14-023, Taipei.

Conclusions

From these analysis results, we can make the following conclusions:

1. For a sample structure of a typical three-story school building, the capacity spectrum has an implicit safety factor of 2.25 on average.
2. Under a design earthquake with a 475-year return period, the probability of the GI unstable state is 23.2%, which is a slightly higher value, so the structure being evaluated for retrofitting is considered reasonable.
3. Under evaluation with the performance-target earthquake, the probability of the GI unstable state is 5.3%, so the performance target is a reasonable choice. The probability between the IO and CP states is 91.5%, which matches the assessment criteria for moderate damage from a performance-target earthquake.

References

- Applied Technology Council (ATC) (1996), “ATC-40 Seismic Evaluation and Retrofit of Concrete Buildings”, prepared by the Applied Technology Council, Redwood City, Calif.
- Federal Emergency Management Agency (FEMA) (2005), “FEMA 440 Improvement of Nonlinear Static Seismic Analysis Procedures”, prepared by the Applied Technology Council for the Federal Emergency Management Agency, Washington, D.C.
- Lallemant, D., Kiremidjian, A. and Burton, H. (2015), Statistical Procedures for Developing Earthquake Damage Fragility Curves, *Earthquake Engineering and Structural Dynamics*, 44(9), pp. 1373-1389.
- NCREE (2013), “Technology Handbook for Seismic Evaluation and Retrofit of School Buildings”, NCREE report NCREE-13-023, Taipei.
- PEER (2010), “Guidelines for Performance-Based Seismic Design of Tall Buildings”, Report No. 2010/05, Pacific Earthquake Engineering Research Center, College of Engineering University of California, Berkeley, Page 7.
- Vamvatsikos, D., and Cornell, C. A. (2002), Incremental Dynamic Analysis, *Earthquake Engineering and Structural Dynamics*, 31, pp. 491-514.
- Yeh, Y.-K. and Chow, T.-K. (2013), “The Study for the Safety Factor of the Pushover Analysis Procedure based on Capacity Spectrum Method”, NCREE report NCREE-13-007, Taipei.
- Yeh, Y.-K. and Chow, T.-K. (2014), “The Study for

Soil Gas Continuous Monitoring For Earthquake Precursory Studies

Vivek Walia¹, Shih-Jung Lin², Arvind Kumar³, Tsung-Han Jimmy Yang⁴,
Ching-Chou Fu⁵ and Kuo-Liang Wen⁶

Abstract

The present investigations aim at developing an effective earthquake precursory system from the long term soil-gas data obtained from a network of soil-gas monitoring stations covering NW, SW and eastern Taiwan. As per the present practice, the data from various stations are examined synoptically to evaluate earthquake precursory studies. The present study is also aimed at the appraisal and filtrations of these environmental/meteorological parameters and to create an automated real-time database for earthquake precursory study. During the observation period of 2015, about 34 earthquakes of magnitude ≥ 5 were recorded and out of these, 16 earthquakes fell under the defined selection criteria and were tested in the proposed model. From all the monitoring station data it has been found that Jaosi monitoring station has recorded the maximum number of earthquakes whereas Hsincheng monitoring station has highest efficiency. It has also been found that 3 earthquakes lie in the common influence area of all the monitoring stations. Out of these, 2 earthquakes happened to have precursory signals which can be correlated with the occurred earthquake whereas one earthquake has shown precursory signals at HC and HH monitoring stations.

Keywords: Soil-gas, Earthquake, Radon, SSNTDs, Real-time, Data base

Introduction

Temporal variations in soil-gas composition at the established monitoring stations along some active faults are demonstrated as effective investigating tool to monitor the tectonic activities in the region (Fu et al., 2005; Kumar et al., 2009, 2013; Walia et al., 2013; Yang et al., 2006). There are a number of variables other than seismic events that influence soil-gas composition from earth's surface at a given location. The most important factor is influence of meteorological parameters. Influence of meteorological parameters on gas emanation was reported from time to time by various authors (Walia et al., 2005; Etiopie et al., 1997, Armienta et al., 2002; Chyi et al., 2011; Fu et al., 2008, 2009; Walia et al., 2009a; Yang et al. 2005, 2011). Several models have been proposed to explain soil-gas migration from subsurface especially of radon over large distances. It has been established that radon is transported by underground water or carrier gases along preferential

pathways such as fractures and faults (Yang et al., 2003).

The island of Taiwan is a product of the collision between Philippine Sea plate and Eurasian plate which makes it a region of high seismicity. Active subduction zones occur south and east of Taiwan. To the south an oceanic part of the Eurasian plate is subducting beneath the Philippine Sea plate along the Manila Trench, whereas in east the oceanic lithosphere of the Philippine Sea plate is subducting northwestward underneath the Eurasian plate along the Ryukyu Trench. These collisions are generally considered to be the main source of tectonic stress in the region. Among them, some have been identified as active faults (Hsu 1989). A detailed study of these active faults will provide information about the activity of these faults and give basis, which may greatly help to reduce the damage when the unavoidable large earthquakes come. This study

¹ Research Fellow, National Center for Research on Earthquake Engineering, walia@ncree.narl.org.tw

² Assistant Research Fellow, National Center for Research on Earthquake Engineering, sjlin@ncree.narl.org.tw

³ Associate Research Fellow, National Center for Research on Earthquake Engineering, kumar@ncree.narl.org.tw

⁴ Assistant Research Fellow, National Center for Research on Earthquake Engineering, 15066029@ncree.narl.org.tw

⁵ Postdoctoral Fellow, Institute of Earth Sciences, Academia Sinica, ccfu@earth.sinica.edu.tw

⁶ Professor, National Center for Research on Earthquake Engineering, wenkl@ncree.narl.org.tw

further helps the earthquake engineers to define the building codes for each fault zone.

Presently we have focused on temporal geochemical variations of soil-gas composition at established geochemical observatories along different faults in Hsinchu (HC) (i.e. along Hsincheng fault), Tainan (HH) (along Hsinhua fault) and Ilan (at Jaosi (JS) areas of Taiwan (Fig.1) and to find the corelation of enhanced concentrations of radon with the seismic activity in the region from data generated during the observation period (Fig. 1) and test the efficiency of the proposed tectonic setting based model (Walia et al., 2009b, 2010). This is being done along with some preliminary field surveys in Taipei area to find appropriate site for establishing geochemical monitoring station along Shan-Chiao fault, Northern Taiwan.

Radon (^{222}Rn) is the major radioactive gas in volcanic areas. The study of radon-thoron concentration variations in volcanic areas has been considered as a useful tool to investigate the volcanic activity. In addition to already established three monitoring stations for earthquake forecasting studies, we also tried to investigate variations of soil-gas radon-thoron concentrations using Solid State Nuclear Track Detectors (SSNTDs) technique (i.e. cellulose nitrate LR-115 films) to observe the tectonic activity in the Tatun volcanic area of northern Taiwan under the ongoing Ministry of Science and Technology (MOST) project.

The present study is also aimed at the appraisal and filtrations of environmental/meteorological parameters and to create an automated real-time database for earthquake precursory study. However, here we will discuss only about the data from established geochemical observatories HC, JS and HH and its correlation with seismic events during observation period of the year 2015.

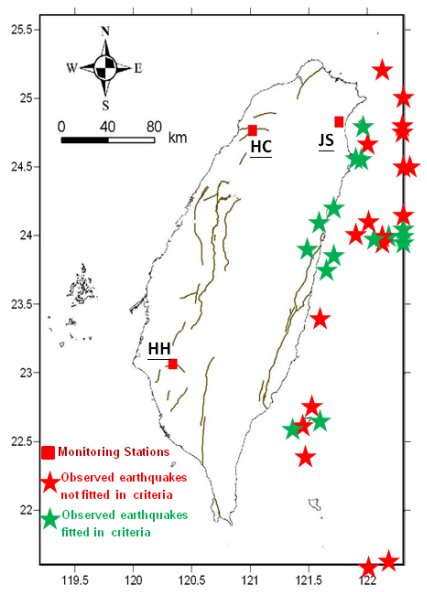


Fig.1: Map showing distribution of monitoring station and earthquakes recorded in the year 2015.

Methodology

To carry out the present investigation, temporal soil-gas composition variations were measured regularly at above mentioned continuous earthquake monitoring stations established using RTM2100 (SARAD) for radon and thoron measurement (for details see previous reports)

Results and Discussions

As per the present practice, the data from various stations are examined synoptically to evaluate earthquake precursory signals against the backdrop of rainfall and other environmental factors (see the previous reports). Various guidelines are developed to identify the nature of precursory signals almost in real-time. Data from various monitoring stations (run by NCREE and NTU in collaboration) are automatically uploaded to the web service which provides the data management/exhibition with less response time database. In addition to monitoring station data, seismic parameters (i.e. Magnitude/location/depth of the event, the intensity/epicentral distance at a monitoring station, etc.) and meteorological parameter data are also uploaded from Central Weather Bureau of Taiwan (www.cwb.gov.tw) simultaneously. It would be helpful in increasing efficiency of earthquake prediction studies.

During the observation period of 2015, about 34 earthquakes of magnitude ≥ 5 were recorded in and around Taiwan (Fig.1). However, out of these, 16 (i.e. about 47%) earthquakes fell under the defined selection criteria and were tested for the proposed model. Out of these 16 earthquakes 12 (i.e. about 75% of fitted earthquakes) have shown precursory signals at the established monitoring either individually or commonly.

Hsincheng Monitoring Station (HC)

During the observation period (i.e. Jan., 2015 until Dec., 2015) potential precursory signals have been recorded for some earthquakes having magnitude ≥ 5 that occurred in the region (Fig. 2). About 34 seismic events were observed during the observation period and 9 (i.e. about 26%) of these earthquakes fell under the defined selection criteria for this monitoring station (Fig. 2). Out of these 9 earthquakes 8 (i.e. about 88% of fitted earthquakes) have shown precursory signals at the established monitoring station. One earthquake which has shown no precursory signals, although fitted in the selection criteria, but still seems at large distance from the monitoring station. We have redefined the influence area for the HC monitoring station which is shown by circle in Fig. 2.

Jaosi Monitoring Station (JS)

At the JS monitoring station about 13 (i.e. 38%) fitted well under the defined selection criteria for this monitoring station from 34 seismic events of magnitude ≥ 5 that occurred during the observation period (i.e. Jan., 2015 until Dec., 2015) (Fig. 3). Some of the earthquakes overlap and can't be seen clearly in the Fig. 3. Out of these 13 fitted earthquakes 10 (i.e. about 77%) have shown precursory signals at this monitoring. We have defined the influence area for the JS monitoring station which is shown by circle in Fig. 3.

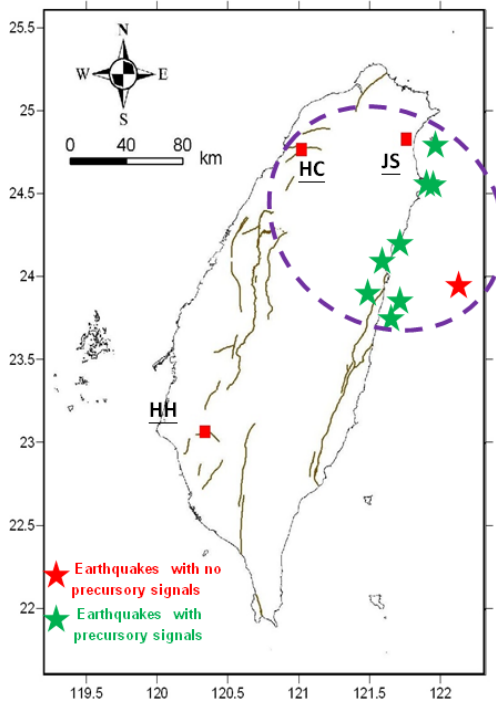


Fig. 2: Map showing distribution of recorded and correlated earthquakes at the HC monitoring station in Hsinchu area during year 2015.

Hsinhua Monitoring Station (HH)

Totally, 6 (i.e. 18% of all recorded earthquakes and about 38% all fitted earthquakes) seismic events fitted defined selection criteria for HH monitoring from all 34 recorded earthquake of magnitude ≥ 5 during the observation period (Fig. 4). From these 6 fitted earthquakes 4 (i.e. about 67%) have shown correlation with observed precursory signals at this monitoring station. Based on the observed data and its correlation with the seismic event we have redefined the influence area for a HH monitoring station which is shown by circle in Fig. 4.

From all the monitoring station data it has been found that JS monitoring station has recorded the maximum number of earthquakes whereas HC monitoring station has the highest efficiency. It has also been found that 3 earthquakes lie in a drawn common influence area of all the monitoring stations (Fig. 5). Out of these 2 earthquakes happened to have

precursory signals which can be correlated with the occurred earthquake whereas one earthquake has shown precursory signs at HC and HH monitoring stations (Fig.2 to Fig.5).

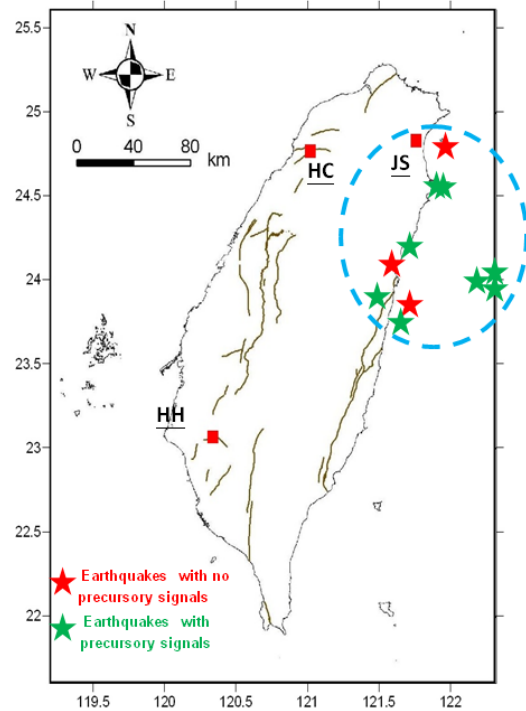


Fig. 3: Map showing distribution of recorded and correlated earthquakes at the JS monitoring station in Ilan area during year 2015.

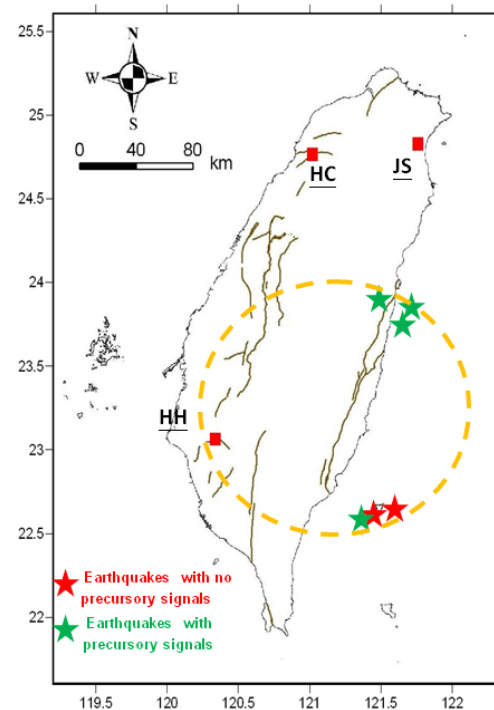


Fig. 4: Map showing distribution of recorded and correlated earthquakes at the HH monitoring station in Tainan area during year 2015.

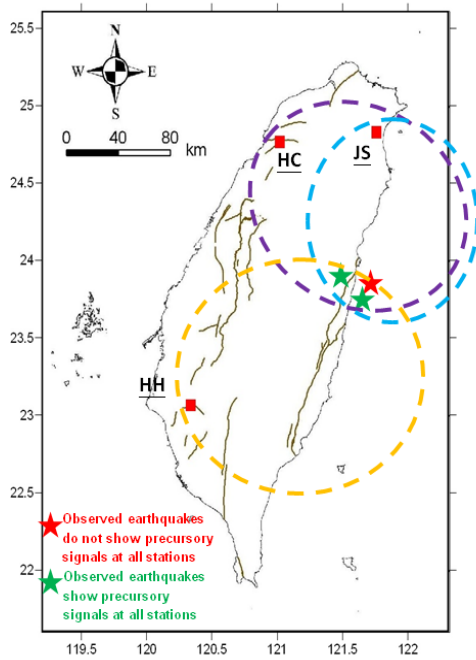


Fig. 5: Map showing distribution of recorded and correlated earthquakes in the common zone.

References

- Armienta, M.A., Varley, N., Ramos E. (2002). Radon and hydrogeochemical monitoring at Popocatepetl volcano, Mexico. *Geof. Intern.* 41, 271-276.
- Chyi, L.L., Quick, T.J., Yang, T.F., Chen, C-H. (2011). The origin and detection of spike-like anomalies in soil gas radon time series. *Geochem. J.*, 45, 431-438.
- Etiopie G., Calcara, M., Quattrocchi, F. (1997). "Seismogeochemical algorithms for earthquake prediction: an overview". *Annali Di Geofisica*, 40(6), 1483-1492.
- Fu, C.-C., Yang, T.F., Du, J., Walia, V., Chen, Y.-G., Liu, T.-K., Chen, C.-H. (2008). Variations of helium and radon concentrations in soil gases from an active fault zone in southern Taiwan. *Radiat. Meas.* 43, S348-S352.
- Fu, C.C., Yang, T.F., Walia, V., Chen, C.H. (2005). "Reconnaissance of soil gas composition over the buried fault and fracture zone in southern Taiwan". *Geochemical Journal*, 39, 427-439.
- Fu, C.-C., Yang, T.F., Walia, V., Liu, T.-K., Lin, S.-J., Chen, C-H., Hou, C.-S. (2009). Variations of soil-gas composition around the active Chihshang Fault in a plate suture zone, eastern Taiwan. *Radiat. Meas.* 44, 940-944.
- Hsu, T. L. (1989). *Geology and Engineering*. 8th Ed., Ker-Chi -Book Company, Taipei (in Chinese)
- Kumar, A., Singh, S., Mahajan, S., Bajwa, B.S., Kalia, R., Dhar, S. (2009). "Earthquake precursory studies in Kangra valley of North West Himalayas, India, with special emphasis on radon emission". *Appl. Radiat. Isot.* 67, 1904-1911.
- Kumar, A., Walia, V., Yang, T.F., Hsien, C-H., Lin, S.J., Eappen, K.P., Arora, B.R. (2013). Radon-thoron monitoring in Tatun volcanic areas of northern Taiwan using LR-115 alpha track detector technique: Pre Calibration and Installation. *Acta Geophysica*, 61 (4), 958-976.
- Walia V, Yang TF, Lin S-J, Kumar A, Fu CC, Chiu J-M, Chang H-H, Wen K-L, Chen C-H (2013) Temporal variation of soil gas compositions for earthquake surveillance in Taiwan. *Radiat Meas* 50:154-159.
- Walia, V., Lin, S-J., Yang, T.F., Fu, C-C., Hong, W-L., Wen, K-L., Chen, C-H. (2010). "Soil-gas monitoring: A tool for fault delineation studies along Hsinhua Fault (Tainan) Southern Taiwan." *Applied Geochemistry*, 25, 602-607.
- Walia, V., Virk, H.S., Yang, T. F., Mahajan, S., Walia, M. and Bajwa, B.S. (2005). "Earthquake prediction studies using radon as a precursor in N.W Himalayas, India: a case study". *TAO*, 16(4), 775.804.
- Walia, V., Yang, T.F., Lin, S.J., Hong, W.L., Fu, C.C., Wen, K.L., Chen, C.H. (2009b). "Continuous temporal soil gas composition variations for earthquake precursory studies along Hsincheng and Hsinhua faults in Taiwan". *Radiat. Meas.*, 44, 934.939.
- Walia, V., Yang, T.F., Lin, S.J., Hong, W.L., Fu, C.C., Wen, K-L., Chen, C-H. (2009a). "Geochemical variation of soil-gas composition for fault and earthquake precursory studies along Hsincheng fault in NW Taiwan". *Appl. Radiat. Isotopes*, 67, 1855- 1863.
- Walia, V., Yang, T.F., Lin, S-J., Kumar, A., Fu, C-C., Chiu, J-M., Chang, H-H., Wen, K-L., Chen, C-H. (2013). "Temporal variation of soil gas compositions for earthquake surveillance in Taiwan." *Radiat. Meas.*, 50, 154-159.
- Yang, T.F., Chou, C.Y., Chen, C.H, Chyi, L.L., Jiang, J.H. (2003). "Exhalation of radon and its carrier gases in SW Taiwan". *Radiat. Meas.* 36, 425.429.
- Yang, T.F., Fu, C.C., Walia, V., Chen, C.H., Chyi, L.L., Liu, T.K., Song, S.R., Lee, M., Lin, C.W., Lin, C.C., (2006). Seismo-geochemical variations in SW Taiwan: multi-parameter automatic gas monitoring results, *Pure Appl. Geophys.*, 163, 693.709.
- Yang, T.F., Walia, V., Chyi, L.L., Fu, C.-C., Chen, C.-H., Liu, T.-K., Song, S.-R., Lee, C.-Y., Lee, M. (2005). Variations of soil radon and thoron concentrations in a fault zone and prospective earthquakes in SW Taiwan. *Radiat. Meas.* 40, 496-502.
- Yang, T.F., Wen, H.-Y., Fu, C.-C., Lee, H.-F., Lan, T.F., Chen, A.-T., Hong, W.-L., Lin, S.-J., Walia, V., (2011). "Soil radon flux and concentrations in hydrothermal area of the Tatun Volcano Group, Northern Taiwan". *Geochem. J.*, 45, 483-490.

Reliability Assessment of Using the Equivalent Lateral Force Method to Estimate Elastic Seismic Responses with Accidental Torsion Effects

Jui-Liang Lin¹, Wei-Chun Wang² and Keh-Chyuan Tsai³

林瑞良¹、王韋竣²、蔡克銓³

Abstract

Model building codes require consideration of accidental eccentricity in addition to the existing eccentricity in order to reflect accidental torsion effects on the seismic responses of buildings. In some model building codes, accidental eccentricity is multiplied even further by the torsional amplification factor A_x in order to minimize the discrepancy between the statically and dynamically estimated responses. This study investigates the reliability of using the equivalent lateral force method to estimate elastic seismic responses with code-specified accidental torsion effects. To achieve this aim, the discrepancy curves that represent the exceedance probabilities of the difference between the statically and dynamically estimated elastic seismic responses are first developed. The discrepancy curves for 3-story, 9-story, and 20-story example buildings are then constructed and investigated accordingly. Besides the building height, the investigated buildings vary based on four frequency ratios: 0.7, 1.0, 1.3, and 1.6. The existing eccentricity ratios of the investigated buildings range from 0% to 30%. The assessment results of this study clearly indicate that the torsional amplification factor A_x specified in some building codes generally provides conservative estimates of displacement for medium-rise and high-rise buildings.

Keywords: reliability assessment; seismic responses; accidental torsion effect; torsional amplification factor; equivalent lateral force method

Introduction

In comparison with the static analysis approach, the dynamic analysis approach is typically more reliable when assessing the seismic responses of buildings. Nevertheless, due to the restraints of design costs and/or technical requirements, the static analysis approach stipulated in seismic design codes (ASCE 7-10 2010, Eurocode 8 2003) is still widely employed in engineering practice. ASCE 7-10 (2010) stipulates that the deflection at level x (δ_x) used to compute the design story drift could be the deflection obtained from an elastic analysis multiplied by the deflection amplification factor C_d . This clearly indicates that the deflection of buildings deforming far into the inelastic range can instead be efficiently computed by employing elastic dynamic analysis

together with the deflection amplification factor. Consequently, assessing the discrepancies between the statically and dynamically estimated responses of linearly elastic structures is essential in engineering practice.

In order to consider the accidental torsion effect, seismic design codes (ASCE 7-10 2010, Eurocode 8 2003) require both the static and dynamic analysis approaches to shift the center of mass (CM) of each floor to a distance of $\pm 5\%$ of the floor plane dimension, perpendicular to the direction of ground motion. The plus and minus signs of the abovementioned 5% indicate that the CM is shifted by 5% in either direction. It is well known that accidental torsion mainly accounts for the uncertainties in the locations of the CM and the

¹ Research Fellow, National Center for Research on Earthquake Engineering, jllin@ncree.narl.org.tw.

² Graduate Student, Department of Civil Engineering, National Taiwan University, r00521203@ntu.edu.tw

³ Professor, Department of Civil Engineering, National Taiwan University, kctsai@ntu.edu.tw.

center of rigidity (CR). It is also known to account for uncertainties in strength distributions and the rotational components of ground motions. Therefore, the accidental eccentricity, *i.e.*, $\pm 5\%$ of the floor plane perpendicular to the ground motion, is a lumped reflection of the four abovementioned uncertainties. Dimova and Alashki (2003) pointed out that, even for symmetric buildings with a 5% accidental eccentricity ratio, the static analysis procedures stipulated by Eurocode 8 may underestimate accidental torsional effects by up to 21%.

For torsionally irregular buildings, some building codes, *e.g.*, ASCE 7-10 (2010), stipulate that the accidental eccentricity used in the static analysis approach should be further amplified by multiplying by the torsional amplification factor. The definition and limits of the torsional amplification factor, denoted by A_x , are:

$$1 \leq A_x = \left(\frac{\eta}{1.2} \right)^2 = \left(\frac{\delta_{\max}}{1.2\delta_{\text{avg}}} \right)^2 \leq 3 \quad (1)$$

where δ_{\max} is the maximum displacement at the x -th story and δ_{avg} is the average of the displacements on both sides of the floor plane at the x -th story. The so-called torsionally irregular buildings, judged by using the parameter $\eta = \delta_{\max}/\delta_{\text{avg}}$ (Eq. 1), are those prone to rotation and those with very slender floor planes, in which the longest side is perpendicular to the ground motion. Therefore, in the code-specified static analyses (ASCE 7-10 2010), two stages of analysis work are required in order to consider the accidental torsion. The first stage is to shift the CM from the original location to a distance of $\pm 5\%$ of the floor plane and then perform the static analysis based on this modified building structure, from which the A_x value for each floor is computed. The second stage of analysis involves analyzing the twice-modified building, whereby the CM for each floor is moved from the original place to a distance of $\pm 5\% \times A_x$ of the floor plane. The static analysis results based on this twice-modified building are the final seismic response estimates of the building.

Due to the lack of probability-based evaluations of statically estimated seismic responses with accidental torsion, the aim of this study is to explore the reliability of the aforementioned responses, which may act as a bridge between current and future seismic design codes in terms of accidental torsion. By mimicking the construction of fragility curves, this study first develops a means of constructing discrepancy curves that show the probabilities of exceedance for the discrepancy states of statically estimated seismic responses. Second, by constructing discrepancy curves for the estimated displacements of 3-story, 9-story, and 20-story buildings, this study evaluates the reliability of the statically estimated displacements with accidental torsion effects.

Discrepancy Curves

The discrepancy represents the normalized difference between the statically and dynamically estimated engineering demand parameters (*EDP*) with the accidental torsion effect. The discrepancy, denoted as DC' , is expressed as:

$$DC' = \frac{(EDP_{\pm 0.05 A_x})_{\text{static}} - (EDP_{\pm 0.05})_{\text{dynamic}}}{(EDP_{\pm 0.05})_{\text{dynamic}}} \times 100\% \quad (2)$$

The *EDPs* considered in this study include the peak displacement at the CM, and the peak displacements on the flexible side (FS) and the stiff side (SS). The FS and SS are the two sides of a floor plane close to the CM and the CR, respectively. The subscripts '*static*' and '*dynamic*' indicate that the quantities in the associated parentheses result from the static and dynamic analysis approaches, respectively. The subscripts ' $\pm 0.05 A_x$ ' and ' ± 0.05 ' represent the distances from the original location of the CM to the location of the CM used in the analysis work. It should be noted that, in the dynamic analysis, the CM is shifted by $\pm 5\%$, rather than $\pm 5\% \times A_x$, of the floor plane perpendicular to the ground motion. In the static analysis, the peak base shear force obtained from the dynamic analysis is distributed vertically over the building in a triangular formation, according to the seismic design codes for buildings.

Following the definition of the fragility function, the discrepancy function, $F_{dc'}(e)$, for the discrepancy state dc' (a value of $|DC'|$) is defined as the probability of reaching or exceeding the discrepancy state as a function of the eccentricity ratio e , and is idealized by a lognormal distribution:

$$F_{dc'}(e) \equiv P[|DC'| \geq dc' | e] = \Phi \left(\ln \left(\frac{e}{\lambda'} \right) / \beta' \right) \quad (3)$$

whereby Φ denotes the standard normal (Gaussian) cumulative distribution function, λ' denotes the medium value of the distribution, and β' denotes the logarithmic standard deviation. Since the random variable DC' (Eq. 2) may be positive or negative, the absolute value of the random variable DC' , denoted as $|DC'|$, is used in Eq. 3. The eccentricity ratio e is the existing eccentricity of the building divided by the floor plane dimension in the same direction. The existing eccentricity is the original distance between the CM and CR, excluding the accidental eccentricity. The discrepancy state dc' represents the extent of the discrepancy value. The defined four discrepancy states representing minor (denoted as $dc'1$), moderate (denoted as $dc'2$), severe (denoted as $dc'3$), and unacceptable (denoted as $dc'4$) levels are 10%, 20%, 40%, and 60%, respectively.

The procedures for constructing the discrepancy curves are similar to the procedures used for constructing fragility curves. In this study, the

displacement estimates obtained from the static analyses are the quantities of concern. In addition to obtaining the exceedance probabilities of the discrepancy states, it is also useful to determine the degree to which the statically estimated seismic responses with the accidental torsion effects have been underestimated or overestimated. Therefore, rather than $|DC'|$, the average DC' values for all floors under the excitations of all applied ground motions are also computed.

Assessment Results

In order to investigate the reliabilities of the displacement estimates obtained from the static analyses, the discrepancy curves of numerous 3-story, 9-story, and 20-story buildings were constructed. The prototypes of these buildings are those used in the SAC steel research project (FEMA-355C 2000) for buildings located in Los Angeles. These three prototype buildings are symmetrical and their CMs coincide with the CRs located at the geometric centers of the floor plane. These three prototype buildings can represent low-rise, medium-rise, and high-rise buildings. In addition to the existing eccentricity ratio, the frequency ratio Ω is a common parameter for categorizing asymmetric-plan buildings. The frequency ratio Ω is the ratio of the frequency of the first rotational mode, ω_θ , to the frequency of the first translational mode, ω_x , of the corresponding symmetrical building. When the frequency ratio is lower or higher than unity, the building is torsionally flexible or torsionally stiff, respectively. When the frequency ratio is approaching 1 or equal to 1, the building is torsionally similarly stiff. In this study, the floor mass moment of inertia of each prototype building is scaled to yield four different frequency ratios: $\Omega = 0.7, 1.0, 1.3,$ and 1.6 . In addition, the CMs of these buildings are shifted in the positive z -direction to result in 31 existing eccentricity ratios varying from 0% to 30% in 1% increments. Therefore, a total of 372 (*i.e.*, $3 \times 4 \times 31$) buildings were eventually analyzed in this study. For the purposes of discussion, the buildings are categorically labeled SAC3, SAC9, and SAC20 according to the number of floors in the building. Rayleigh damping is used to simulate the inherent damping of the buildings. The damping ratios of the first two x -translational dominant modes are set equal to 2%. The selected ground motions are the twenty historical earthquake records of the SAC project scaled to a return period of 475 years for buildings located in Los Angeles (FEMA-355C). These twenty ground motions are applied to all of the buildings in the x -direction.

In this study, an accidental eccentricity ratio of 5%, designated as case I, represents a CM moved farther away from the CR. For an accidental eccentricity ratio of -5%, designated as case II, the

CM is located closer toward the CR. Figures 1(a), (b), and (c) show the average DC' values obtained at all stories of SAC3, SAC9, and SAC20, respectively. Figure 1 shows that the average displacements obtained from the static analyses are all overestimated except for the averaged SS displacements of SAC3 and SAC9, while their frequency ratios are 0.7 and 1.0. The peak values of the overestimation of the average displacements at the CM and FS of SAC3, SAC9, and SAC20 are approximately 40%, 60%, and 130%, respectively. This implies a higher overestimation percentage for the average displacements at the CM and FS with increased building height. In comparison with the torsionally stiff ($\Omega = 1.3$ and 1.6) and torsionally similarly stiff ($\Omega = 1.0$) buildings, the average displacements at the CM and FS for torsionally flexible buildings ($\Omega = 0.7$) are the most overestimated. On the other hand, the underestimation of the averaged SS displacements of SAC3 and SAC9, while their frequency ratios are 0.7 and 1.0, increases as their existing eccentricity ratios increase. This underestimation is more apparent for lower torsionally flexible buildings, *i.e.*, SAC3 with $\Omega = 0.7$, than for higher torsionally similarly stiff buildings, *i.e.*, SAC9 with $\Omega = 1.0$. Furthermore, this underestimation is slightly more apparent in case I than in case II. That is to say, a further underestimation of the SS displacement occurs when using the +5% accidental eccentricity ratio (case I). When the frequency ratios are 1.3 and 1.6, the averaged SS displacements of SAC3, SAC9, and SAC20 are mostly overestimated, in which the maxima are approximately 20%, 30%, and 75% overestimated, respectively. This overestimation generally increases as the existing eccentricity ratio decreases.

Figure 2 shows the discrepancy curves of the statically estimated displacements at the CM, and those for the FS and SS are not shown, owing to the limited pages. These figures indicate that the statically estimated displacements for torsionally stiff buildings are generally more reliable than those for torsionally similarly stiff and torsionally flexible buildings. For example, the far left plot of Fig. 2(a) shows that the exceedance probabilities of the discrepancy states $dc'1$, $dc'2$, $dc'3$, and $dc'4$ for the displacements at the CM of SAC3 with $\Omega = 0.7$ and $e = 30\%$ in case I are approximately 0.95, 0.8, 0.4, and 0.15, respectively. Nevertheless, for SAC3 with $\Omega = 1.0$ (the second plot of Fig. 2(a)), the four abovementioned exceedance probabilities are approximately 0.65, 0.4, 0.2, and 0.1, respectively. As for SAC3 with $\Omega = 1.3$ (the third plot of Fig. 2(a)), the four abovementioned exceedance probabilities are approximately 0.5, 0.22, 0.1, and 0.05, respectively. It is also noted that there is no obvious difference between those for $\Omega = 1.3$ and $\Omega = 1.6$, which are both torsionally stiff.

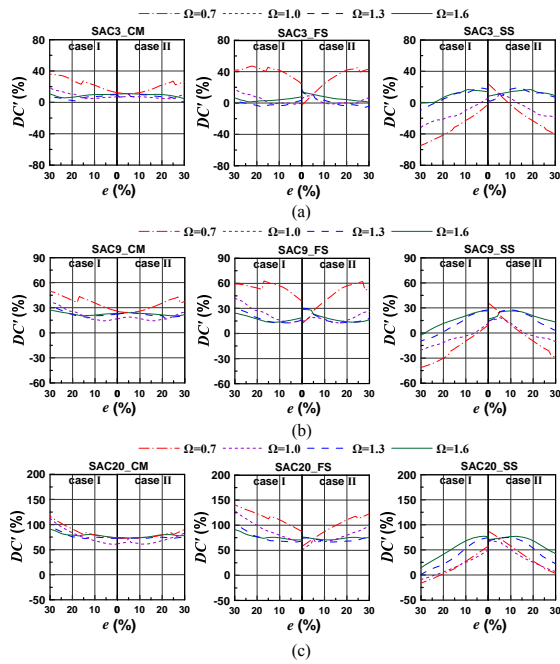


Figure 1. The average DC' values of (a) SAC3, (b) SAC9, and (c) SAC20 under the excitation of the selected earthquakes.

Comparing the investigation results for SAC3, SAC9, and SAC20 indicates that the exceedance probabilities of the discrepancy states $dc'1$, $dc'2$, $dc'3$, and $dc'4$ increase when the building height increases. This observation is consistent with the observations made by comparing Figs. 1(a), (b), and (c). In most conditions, the exceedance probabilities for torsionally stiff buildings ($\Omega = 1.3$ and 1.6) generally remain constant despite the variation of the existing eccentricity ratio. This implies that the reliability of the statically estimated displacements for torsionally stiff buildings is generally unrelated to the existing eccentricity ratio. By comparing the investigation results for CM, FS, and SS, it is reasonable to conclude that the exceedance probabilities of the discrepancy states for the statically estimated displacements at the CM are generally less than those on the FS and SS. This clearly indicates that the torsional effect, which is more significant on the two sides of the floor plane than at the CM, generally reduces the reliability of statically estimated displacements.

Conclusions

Discrepancy curves, which present the exceedance probabilities of the differences between statically and dynamically estimated responses, were developed. The discrepancy curves were used to assess the reliability of seismic responses obtained from the static analysis approach. This study systematically investigated the reliabilities of the statically estimated displacements with accidental torsion effects. The discrepancy curves for the

various 3-story, 9-story, and 20-story buildings investigated in this study highlighted several trends associated with the reliability values of concern. For torsionally stiff buildings, which are commonly encountered in engineering practice, there is a 65% chance for the statically estimated displacement at the CM of a 20-story building to be overestimated with a discrepancy higher than 15%. This probability becomes even higher for torsionally flexible and torsionally similarly stiff buildings. The assessment results of this study clearly indicated that the torsional amplification factor A_x specified in some building codes generally provides conservative estimates of displacement for medium-rise and high-rise buildings.

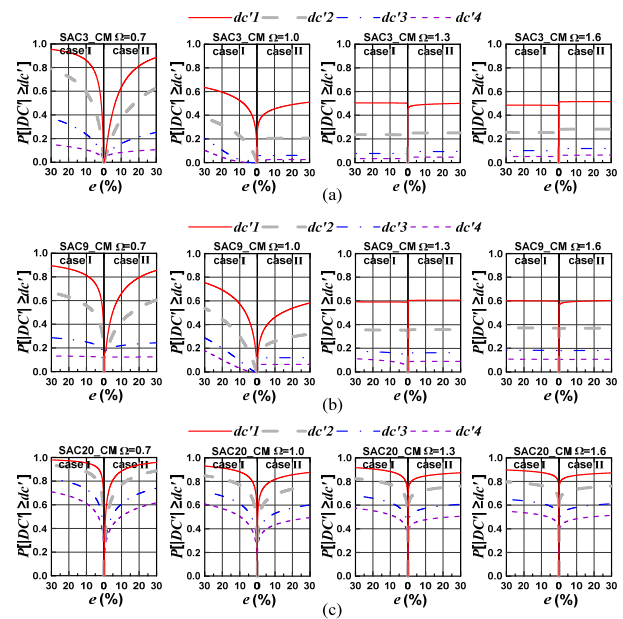


Figure 2. The discrepancy curves of the statically estimated displacements at the CMs of (a) SAC3, (b) SAC9, and (c) SAC20.

References

- ASCE (2010), "Minimum Design Loads for Buildings and other Structures. *ASCE/SEI 7-10*", American Society of Civil Engineers (ASCE), Reston, VA.
- Dimova, S.L. and Alashki, I. (2003), "Seismic design of symmetric structures for accidental torsion", *Bulletin of Earthquake Engineering*, 1, 303-320.
- Eurocode 8, (2003), "Design of Structures for Earthquake Resistance. Part1: General Rules, Seismic Actions and Rules for Buildings. *prEN 1998-1:2003(E)*", Commission of the European Communities, European Committee for Standardization, Brussels.
- FEMA-355C (2000), "State of the art report on systems performance of steel moment frames subject to earthquake ground shaking", prepared by the SAC Joint Venture for the Federal Emergency.

An Experimental Study of the In-Plane Cyclic Behavior of Low Aspect Ratio SC Wall Piers

Chang-Ching Chang¹ and Yin-Nan Huang²

張長菁¹、黃尹男²

Abstract

A steel-plate composite (SC) wall is composed of steel faceplates, infill concrete, and connectors. The faceplates are joined with steel tie rods that ensure structural integrity. Steel studs are welded to the faceplates to ensure composite behavior. This paper summarizes the results of in-plane cyclic tests of four SC walls. The flexure-critical wall piers are 2m long and 1m high. The faceplates are embedded in the foundation and connected to the foundation concrete using shear studs and transverse reinforcement. The influence of infill reinforcement ratio and the wall-foundation connection is studied. The test results confirm the effectiveness of the analytical method of Epackachi *et al.* in predicting the in-plane monotonic behavior of low aspect-ratio SC wall piers.

Keywords: steel-plate composite (SC) walls, cyclic tests

Introduction

Steel-plate-concrete (SC) composite walls are being constructed in nuclear power plants (NPP) in the United States and China. These walls are composed of steel faceplates, infill concrete, welded connectors that tie the plates together and provide out-of-plane shear reinforcement, and shear studs that enable composite behavior of the faceplates and the infill concrete and delay buckling of the faceplate. SC walls have been used in safety-related nuclear facilities in Korea, Japan, and the United States, and they have been studied for the past 20 years (Ozaki *et al.*, 2004, Epackachi *et al.* 2014, Varma *et al.* 2014). Most numerical studies of SC walls and the test data from those studies have focused on the elastic response range because NPPs are designed to remain elastic under design basis shaking. More importantly, most of these studies addressed shear-critical walls because SC walls have been used in the labyrinthine construction of internal containment structures. The behavior of flexure- and flexure-shear-critical walls is not as well understood, in part, because only a small number of experiments have been performed on them.

Epachachi *et al.* (2014) tested four SC wall piers, each with an aspect ratio (height divided by length) of

1.0. The piers were anchored to a reusable foundation block with a post-tensioned connection. A numerical model for the SC wall piers was validated using the test data. Epachachi *et al.* (2015) also developed an analytical procedure to predict the flexure and flexure-shear response of SC wall piers using the calibrated numerical model.

This paper addresses the inelastic response of SC wall piers subjected to reversed in-plane cyclic loading. The wall-to-foundation connection for these tests is different from that of Epachachi *et al.* (2014) because the faceplates are embedded in the foundation using shear studs and the transverse reinforcement passes through holes in the faceplates. The following sections of the paper describe the testing program, present key experimental results, and validate the analytical method of Epachachi *et al.*

Experimental Program

Four wall piers (SC1 through SC4) were constructed and tested under displacement-controlled reversed cyclic loading. The tests were performed at the National Center for Research on Earthquake Engineering (NCREE) in Taiwan. The design

¹ Assistant Researcher, National Center for Research on Earthquake Engineering

² Associate Professor, Dept. of Civil Engineering, National Taiwan University, Taiwan

variables considered in the testing program were the reinforcement ratio and the faceplate slenderness ratio. The aspect ratio (height-to-length) of each wall was 0.5, which was one-half of the aspect ratio of the specimens used by Epackachi *et al.* (2014). Information on the four walls is provided in Table 1. In this table, the studs and tie rods that serve as connectors, spaced at distance, S ; the overall thickness of the wall is T ; the thickness of each faceplate is t_p ; the reinforcement ratio is $2t_p/T$; and the slenderness ratio of the faceplate is S/t_p . No axial load was imposed on the piers. The faceplate slenderness ratios were 17 and 33, where the lower value complies with the provisions of AISC N690s1 (2015) and the higher value does not comply.

Table 1. Test specimen details.

Specimen	Wall dimension ($H \times L \times T$) (cm \times cm \times cm)	Stud spacing (cm)	Tie rod spacing (cm)	Reinforcement Ratio (%)	Faceplate slenderness ratio
SC1	100 \times 200 \times 29.9	7.5	15	3.1	17
SC2	100 \times 200 \times 29.9	-	15	3.1	33
SC3	100 \times 200 \times 20.9	7.5	15	4.3	17
SC4	100 \times 200 \times 20.9	-	15	4.3	33

Studs and tie rods were used in SC1 and SC3. Only tie rods were used in SC2 and SC4. The studs and tie rods were 13 mm in diameter for all walls. They were fabricated from carbon steel with a minimum tensile strength of 1034 MPa (150 ksi). The yield and ultimate strengths of the steel faceplates were 320 MPa and 460 MPa, respectively. The compressive strengths of the infill concrete and the foundation concrete were 30.5 MPa and 42.2 MPa, respectively.

Figure 1 presents elevation and cross-sectional views of SC1. The base of each wall included a 20-mm-thick A572 Gr.50 steel baseplate and nine 10-mm-thick stiffeners. They were welded to connect the faceplate and the base plate. Two rows of twenty 19-mm-diameter headed studs were welded to the baseplate to anchor the faceplate in the foundation and to improve the transfer of shear and tensile forces. Transverse reinforcement (stirrups) was passed through holes in the embedded sections of the faceplates to further anchor the faceplates. The wall-to-foundation connection was designed to be stiff and strong, and to be different from the flexible connection used in the Epackachi *et al.* tests.

Figure 2 presents the test setup. Five horizontally inclined high-force-capacity actuators were used to apply quasi-static cyclic lateral loads to each specimen via loading brackets. The foundation block was attached to the NCREE strong floor with twelve 69-mm-diameter (M69) threaded bars post-tensioned to 1570 kN (160 tonnes) to prevent foundation movement during testing. The loading brackets were attached to the specimen using seven M69 bars post-tensioned to 1570 kN per bar.

The displacement-controlled reversed cyclic loading protocol is presented in Figure 3. Two cycles

of loading with a speed of 0.2 mm/sec were imposed at each displacement increment. In each loading cycle, the specimen was pushed (loaded in the positive direction to the east) and then pulled. Testing was terminated after peak strength had been reached, at a displacement corresponding to a 30% reduction in resistance.

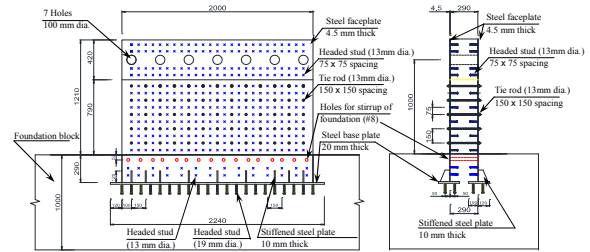


Figure 1. Elevation and cross-section of SC1.



Figure 2. SC wall test setup.

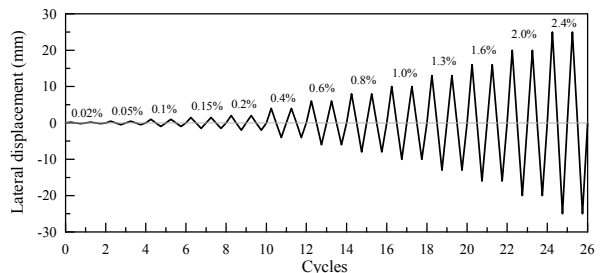


Figure 3. Loading history.

An optical measurement system, strain gauges, linear variable displacement transducers, and dial gauges were used to monitor the response of the wall piers. Linear variable displacement transducers were attached to the ends of the walls to measure in-plane displacement. The movement of the foundation block relative to the strong floor was monitored using dial gauges. The trackers of the optical measurement system were attached to one steel faceplate to measure in-plane and out-of-plane deformations. Strain gauges were installed at four heights above the foundation on the other faceplate to directly measure strains.

Experimental Results

Key test results are provided in Table 2 and Figure 4. The initial stiffness of the SC wall piers, calculated at drift angles of less than +0.1%, are presented in column 2 of Table 2. The values of the displacements corresponding to the onset of faceplate yielding are

listed in columns 3 and 4. The values of the displacements corresponding to the onset of faceplate yielding are listed in columns 5 and 6. First, yielding of the faceplates was identified using strain gauge data. Columns 7 and 8 present the peak loads and the corresponding drift angles in the first (positive) and third (negative) quadrants of Figure 4. Column 9 lists the loads at which the tests were terminated, for both positive (+) and negative (-) directions.

Yielding of the faceplates occurred prior to visible buckling of the faceplates. Buckling of the faceplates first occurred at the free vertical edges prior to reaching the peak load. Plate buckling extended towards the center of wall during subsequent cycles of loading and was affected by the connector spacing. Peak loads were observed at a drift angle of +1.1% for SC1, -1% for SC2, -0.7% for SC3, and +1% for SC4. The peak loads developed in SC1 and SC2 (SC3 and SC4) are similar. In the range investigated, the faceplate slenderness ratio did not impact the peak shearing resistance of the specimens.

Table 2. Summary of test results.

Specimen	Initial stiffness (kN/mm)	Test data						
		Onset of steel plate yielding		Onset of steel plate buckling		Peak load		Test termination
		Load (kN)	Drift angle (%)	Load (kN)	Drift angle (%)	Load (kN) (+/-)	Drift angle (%) (+/-)	Load (kN) (+/-)
SC1	2063	-2276	-0.16	-3272	-0.67	3450 / -3373	1.1 / -1	1584/-1096
SC2	2016	3294	0.4	-3093	-0.5	3390 / -3498	1.1 / -1	2038/-577
SC3	1981	-2159	-0.14	-3131	-0.69	3074 / -3150	0.56 / -0.7	1640/-779
SC4	1692	2856	0.38	-2813	-0.85	3229 / -3166	1 / -1.5	1684/-1286

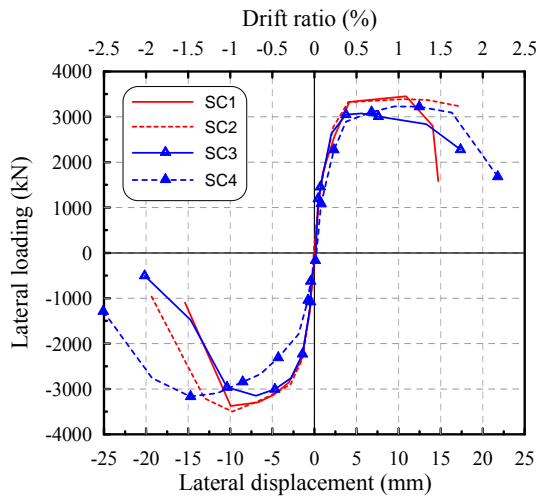


Figure 4. Cyclic backbone curves for the SC walls.

Figure 5 shows the damage to the SC wall piers at the end of testing. The progression of damage in the four SC walls was identical, namely, (1) tensile cracking of the concrete at both ends of the walls, (2) outward buckling and yielding of the steel faceplates at the base of the walls, and (3) crushing and spalling of concrete at the toes of the walls. A steel faceplate was removed from SC2 and SC4 to document damage to the infill concrete. Two wide diagonal cracks

formed in the infill concrete and most of the damage to the infill was concentrated immediately above the foundation at the level of the first row of tie rods.

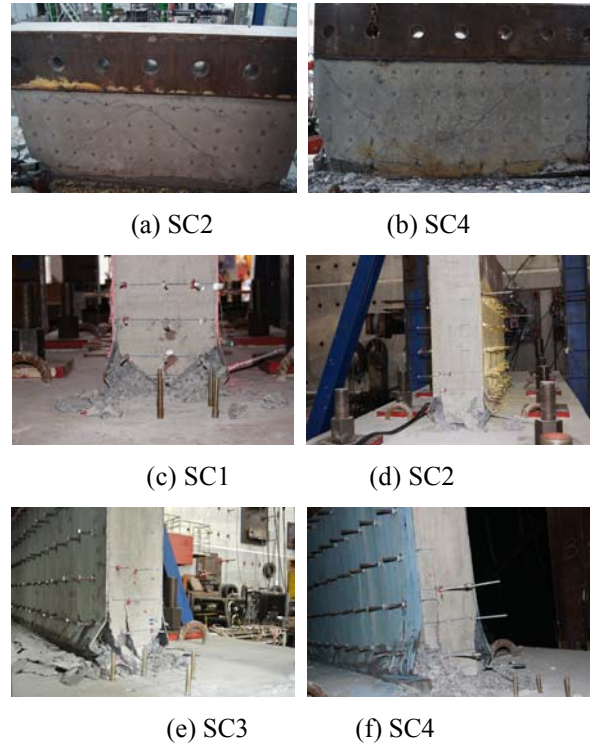


Figure 5. Damage to the SC walls.

The force–displacement relationships for SC1 through SC4 are presented in Figure 6. Consistent trends were observed regarding the impact of the faceplate slenderness ratio on the hysteresis behavior of the SC walls. Pinching was slightly more apparent for the walls with the larger of the two faceplate slenderness ratios.

Negative stiffness was observed in the third quadrant of each panel of Figure 6, followed by a significant reduction in the strength of the wall in the first quadrant of the panel. When negative stiffness occurred during the test, damage was observed in the surface of the RC foundation close to the faceplates at the end of the wall furthest from the actuators. This damage is similar to that shown in the lower left corner of in Figure 5(e). The damage in the foundations greatly influenced the post-peak behavior of the four specimens. More discussion can be found in the work of Chang *et al.* (2015).

Monotonic Analysis of SC Walls

Epacakchi *et al.* (2015) proposed a method to calculate the in-plane flexure-shear response of a SC wall pier subjected to lateral loading. The test results are used to validate the method. A row of holes was drilled in each faceplate to facilitate construction, which reduced the tensile strength of the faceplates near the base of each wall. The area of the holes is

24% of the cross-sectional area of the faceplate. To apply the Epackachi *et al.* method, the faceplate thickness was reduced by 24%. The results are presented in Figure 7; the analytical predictions and the experimental measurements are in excellent agreement.

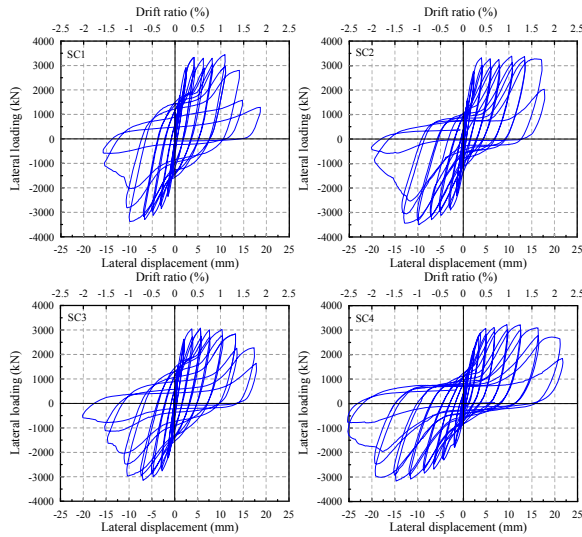


Figure 6. Lateral loading–displacement relationships for the SC walls.

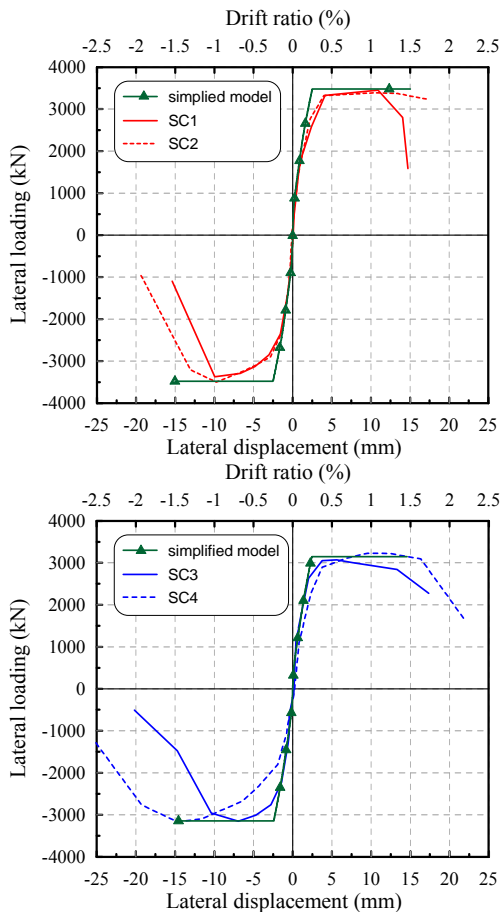


Figure 7. Cyclic backbone curves for the SC walls.

Conclusions

Four SC wall piers, SC1 through SC4, were constructed and tested under displacement-controlled reversed cyclic loading at the National Center for Research on Earthquake Engineering in Taiwan. Each pier had an aspect ratio of 0.5. SC1 and SC2 were 29.9 cm thick, while SC3 and SC4 were 20.9 cm thick. SC1 and SC3 had faceplate slenderness ratios of 17, while SC2 and SC4 had faceplate slenderness ratios of 33.

The key conclusions of this study are as follows:

1. For the two faceplate slenderness ratios studied here, the specimens with the smaller ratios, SC1 and SC3, had peak lateral load capacities similar to SC2 and SC4, respectively, and a less apparent pinching effect than SC2 and SC4, respectively.
2. The wall–foundation design of this study greatly influenced the post-peak hysteresis behavior of all SC wall piers.
3. The SC wall piers in this study sustained peak loads that were similar to those calculated using the analytical method of Epackachi *et al.* (2015).

References

- AISC (2015). "Specification for safety-related steel structures for nuclear facilities, Supplement No. 1." N690s1, American Institute of Steel Construction, Chicago, IL.
- Chang, C.-C., Huang, Y.-N., Chen, B.-A., Epackachi, S., and Whittaker, A. S. (2015). "An experimental study of the in-plane cyclic behavior of low-aspect-ratio steel-plate composite wall piers." paper in preparation.
- Epacakchi, S., Nguyen, N. H., Kurt, E. G., Whittaker, A. S., Varma, A. H. (2014). "In-plane seismic behavior of rectangular steel-plate composite wall piers." *Journal of Structural Engineering*. [http://dx.doi.org/10.1061/\(ASCE\)ST.1943-541X.0001148](http://dx.doi.org/10.1061/(ASCE)ST.1943-541X.0001148).
- Epacakchi, S., Whittaker, A. S., and Huang, Y.-N. (2015). "Analytical modeling of rectangular SC wall panels." *Journal of Constructional Steel Research*, 105 49-59.
- Ozaki, M., Akita, S., Osuga, H., Nakayama, T., Adachi, N. (2004). "Study on steel plate reinforced concrete panels subjected to cyclic in-plane shear." *Nuclear Engineering and Design*, 228 225–244.
- Varma, A. H., Malushte, S., Sener, K., Lai, Z., (2014). "Steel-plate composite (SC) walls for safety-related nuclear facilities: design for in-plane force and out-of-plane moments." *Nuclear Engineering and Design*, 269 240-249.

Corrosion Hazard Map on Reinforcement of Reinforced Concrete Bridges in Taiwan

Yu-Chi Sung¹, Chia-Chuan Hsu², Chian-Kuo Chiu³

宋裕祺¹ 許家銓² 邱建國³

Abstract

The influence of chloride invasion and neutralization on reinforced concrete (RC) bridges served as a target for the establishment of a hazard map of reinforcement corrosion in Taiwan. The hazard map was established on a grid basis and the climate information relating to corrosion models of salt-attack and neutralization in each grid was taken into account. Under natural circumstances, the time required for a specific loss ratio of the effective cross-sectional area of reinforcement as well as structural performance can be displayed on a map of Taiwan. The results obtained could benefit not only durability evaluation of existing bridges but also life-cycle-based design of new bridges.

Keywords: Chloride invasion, Neutralization, Durability, Life-cycle-based design

Introduction

The present study aims to explore the durability of reinforced concrete (RC) bridges with regard to chloride invasion and neutralization as well as to establish a corrosion hazard map for reinforcement. The map of Taiwan was divided into grids and the climate information relating to the deterioration model of chloride invasion and neutralization in each grid was determined by interpolation of the collected data at some specific stations. In addition, some important factors such as population density and the GIS of petrification-industry zones affecting the neutralization were considered in the gridded map. The deterioration trend of RC bridges due to chloride invasion and neutralization can be expressed by a plot of the effective cross-sectional area of corroded reinforcement versus service time. Under natural circumstances, the time required for a specific loss ratio of the effective cross-sectional area of reinforcement can be displayed on a grid basis on the map of Taiwan. The results thus obtained could help bridge management and life-cycle-based design.

Analysis of Salt Attack on RC Bridges

The reinforcement corrosion due to chloride invasion can be divided into four primary periods including incubation, propagation, acceleration front, and acceleration behind, as illustrated in Figure 1. (Hsiao et al., 2012)

In accordance with the codes of JCI (2004) and AIJ (2004), when the chloride diffusion from the concrete surface penetrates into reinforcement and the chloride concentration exceeds the critical point (assumed to be 0.6 kg/m³), the reinforcement begins to corrode and the concrete structure processes into the propagation period. The average annual loss rate of reinforcement weight $V_{corr}(t)$ (%/year) can be expressed by Equation (1). (Chuang, 2012)

$$V_{corr}(t) = \left(\frac{1}{c}\right)^2 (0.578 Cl(t) + 0.023(w/c) - 1.52) \quad (1)$$

where $Cl(t)$ is chlorine salinity at the surface of the reinforcement, c is the concrete cover depth (mm), and w/c is the water–cement ratio.

The acceleration front period can be defined as the duration between initial cracking to spalling of concrete; the corresponding corrosion speed is regarded as the same as that in the propagation period. When the weight loss rate of corroded

¹ Professor, Department of Civil Engineering, National Taipei University of Technology. sungyc@ntut.edu.tw

² Assistant Researcher, National Earthquake Engineering Research Center. chiachuan@ncree.narl.org.tw

³ Associate Professor, Department of Construction Engineering Research Center, National Taiwan University of Science and Technology. ckchiuntust@gmail.com

reinforcement exceeds the critical value $V_{cr} = 3.28\%$, concrete cover begins to spall. At this stage, the average annual loss rate of reinforcement weight $V_{crack}(t)$ (%/year) for the northern, middle, western, and eastern area in Taiwan are expressed, respectively, by Equation (2) through regression analysis.

$$\begin{aligned} V_{crack}(N) &= e^{-0.0809T} \times (RH - 0.45)^{0.2288} \times d^{-0.0374} \\ V_{crack}(M) &= e^{-0.0513T} \times (RH - 0.45)^{0.938} \times d^{-0.0522} \\ V_{crack}(S) &= e^{-0.0169T} \times (RH - 0.45)^{1.765} \times d^{-0.0601} \\ V_{crack}(E) &= e^{-0.0934T} \times (RH - 0.45)^{0.28} \times d^{-0.0875} \end{aligned} \quad (2)$$

where T is the average annual temperature, RH is the average annual humidity, d is the distant from the coast.

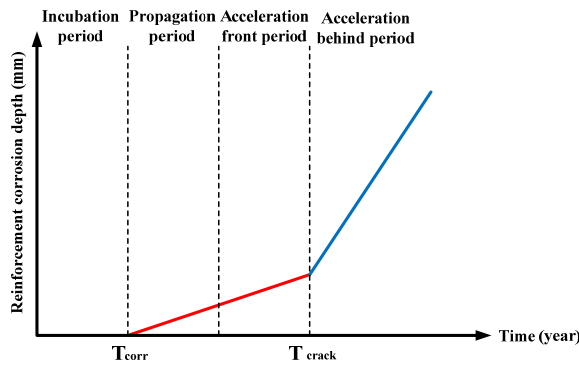


Figure 1. Corrosion rate of reinforcement due to chloride invasion (Hsiao et al., 2012)

Analysis of Neutralization of RC Bridges

In general, concrete neutralization depth can be expressed as the relationship between the neutralization coefficient and the neutralization time as shown in Equation (3).

$$D_c = K\sqrt{t} \quad (3)$$

where K is the neutralization coefficient and t is the time (year).

The neutralization coefficient K can be expressed by Equation (4) via regression analysis. (Sung et al., 2010; Sung & Su, 2011; Chen, 2015)

$$K = 0.43\left(\frac{280}{f'_c}\right) + 28\left(\frac{T}{50}\right) - 12.2RH(1 - RH) + 0.18\left(\frac{\alpha}{4}\right) + 2.85\left(\frac{\beta}{3}\right) + 2.76 \quad (4)$$

where f'_c is the concrete strength (kgf/cm²), T is the average annual temperature (°C), RH is the annual average humidity (%), α is the level of air pollution, indicated by the distance from a petrochemical industrial area, and β is the level of CO₂, indicated by population density.

The concrete neutralization process can be divided into four periods: incubation, propagation, acceleration, and deterioration (Figure 2). The reinforcement corrosion rate in the propagation stage is expressed by Equation (5). (Sung et al., 2010)

$$R_{corr}^{prop}(t) = 1.022 \times 10^{-3} \times \exp^{0.04T} \left(\frac{RH - 45}{100}\right)^{2/3} \times c^{-1.36} \times t^{-1.83} \quad (5)$$

where t is the service time of the bridge (year), RH is the annual average humidity (%), c is the concrete cover depth (mm), and T is the average annual temperature (°C).

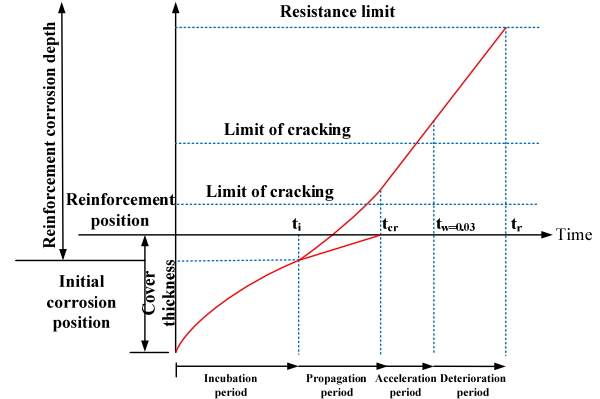


Figure 2. Reinforcement corrosion process caused by neutralization (Sung & Su, 2011)

The reinforcement corrosion rate in the acceleration stage $R_{corr}^{acee}(t)$ is preferably 2.5 times the propagation period (Sung et al., 2010), i.e., $R_{corr}^{acee}(t) = 2.5R_{corr}^{prop}(t)$. Furthermore, the reinforcement corrosion rate in the deterioration stage is assumed to be the same as that in the acceleration period. i.e., $R_{corr}^{dete}(t) = R_{corr}^{acee}(t)$. Therefore, the reinforcement corrosion depth during different stages can be expressed by Equations (6) and (7).

$$\delta_{prop}(t) = R_{corr}^{prop}(t) \times (t - t_i) \quad (6)$$

$$\delta_{acee}(t) = \delta_{prop}(t_{cr}) + R_{corr}^{acee}(t) \times (t - t_{cr}) \quad (7)$$

where t_i is the crucial time of the initial reinforcement corrosion in neutralized concrete, $\delta_{prop}(t)$ is the reinforcement corrosion depth during the propagation period (mm), $\delta_{acee}(t)$ is the reinforcement corrosion depth during the acceleration and deterioration periods (mm).

The critical time point between the propagation stage and the accelerated stage is defined as the time t_{cr} when concrete cracks. Based on reports of Sung, the corrosion rate at the time of cracking of concrete cover is estimated as $R_{corr}^{crack}(t) = 5.805 \times 10^{-3}$ (mm/year) (Sung et al., 2010), and t_{cr} can be determined by simultaneous solution of functions of $R_{corr}^{prop}(t)$ and R_{corr}^{crack} .

The initiation of reinforcement corrosion can be determined by Equation (8).

$$t_i = \left(\frac{c - D_0}{K}\right)^2 \quad (8)$$

$$D_0 = 5.9063(-RH^2 + 1.5RH - 0.45)(c - 5)(\ln f'_c - 2.3) \quad (9)$$

where D_0 is the residual depth of neutralization (mm), c is the concrete cover depth (mm), f'_c is the concrete strength (MPa).

Deterioration of Bridge Material

Reinforcement corrosion not only causes loss of the cross-sectional area of the reinforcement rebar but also directly affects the mechanical properties of structures. Since chloride invasion causes uniform corrosion on the reinforcement, the loss rate of the cross-sectional area and the weight of the reinforcement are almost the same. In addition, the reduced ultimate strength and the reduced cross-sectional area of reinforcement approximately follows a proportional relationship that can be expressed by Equations (10) and (11). (Niu, 2003)

$$\eta(t) = \left[1 - \frac{A_{s, \text{left}}(t)}{A_{s, \text{total}}} \right] \times 100\% \quad (10)$$

$$f_{y, \text{corr}}(t) = [1 - 1.077\eta(t)]f_y, \quad t \geq t_i \quad (11)$$

where $\eta(t)$ is the loss ratio of the cross-sectional area of the corroded reinforcement bars (%), $A_{s, \text{total}}$ is the cross-sectional area of the corroded reinforcement (mm^2), $A_{s, \text{left}}(t)$ is the cross-sectional area of the uncorroded reinforcement (mm^2), $f_{y, \text{corr}}(t)$ is the yield strength of the corroded reinforcement (MPa or kg/cm^2), f_y is the yield strength of the uncorroded reinforcement (MPa or kg/cm^2), and t_i is the time for the initial reinforcement corrosion (year).

The strength of the neutralized concrete was considered the same as that of the non-neutralized concrete. The effective cross section of neutralized concrete is calculated as follows:

$$\begin{cases} B_e(t) = B - 2 \times D_c(t) & , \quad t \geq t_{cr} \text{ and } D_c(t) \geq c \\ H_e(t) = H - 2 \times D_c(t) & , \quad t \geq t_{cr} \text{ and } D_c(t) \geq c \end{cases} \quad (12)$$

where $B_e(t)$ is the effective width of the concrete section (mm), $H_e(t)$ is the effective depth of concrete cross-section (mm), B is the cross-sectional width, H is the cross-sectional depth (mm), $D_c(t)$ is the neutralization depth (mm), and c is the concrete cover thickness (mm).

A schematic of the effective cross-section of the neutralization concrete is shown in Figure 3.

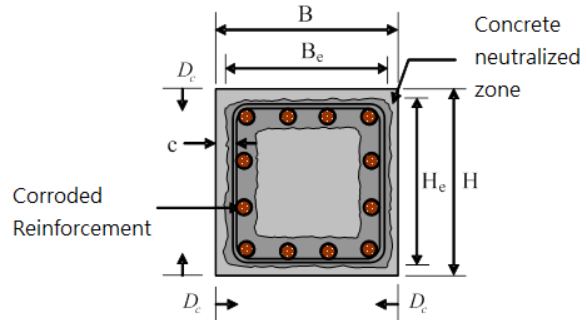


Figure 3. Effective cross-section of neutralized concrete (Sung et al., 2010)

Corrosion Hazard Map of Reinforcement in RC Bridges in Taiwan

By the aforementioned deterioration

characteristics of RC bridges, the decrease in the effective cross-sectional area of the reinforced concrete has a direct influence on the attenuation of structural performance. The present study focuses on the analysis of the loss rate of reinforcement in RC bridges with respect to each geographic grid, considering the specific environmental conditions. The time required for each grid to obtain a specific loss rate of reinforcement can be determined and displayed on the hazard map. The results are shown in Figures 9 and 10.

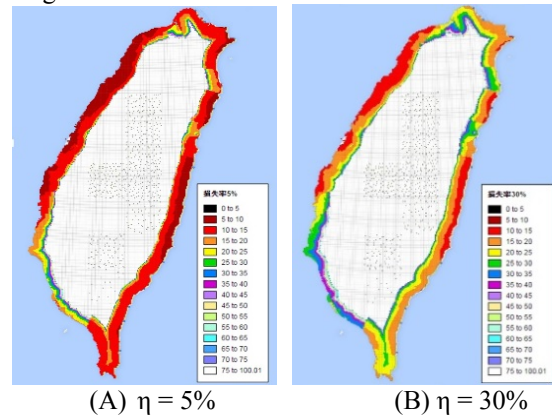


Figure 4. Chloride Hazard Map (Cover = 5 cm)

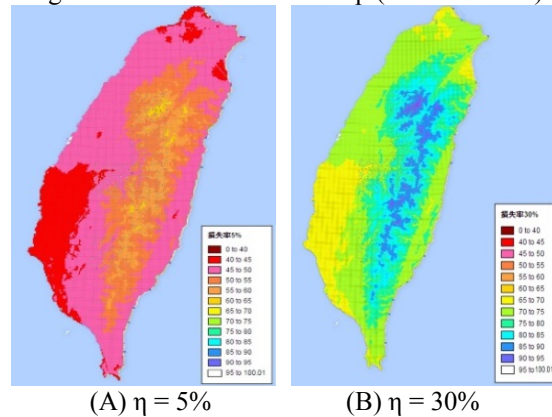


Figure 5. Neutralization Hazard Map (Cover = 5 cm)

The closer the distance from the coast, the more severe the chloride damage will be, as can be seen in Figure 4. The areas in the vicinity of Hsinchu, Hualien, and Taitung have a high concentration of air-borne chloride, and thus more serious corrosion of reinforcement is found. Figure 5 shows the hazard to reinforcement from neutralization. It can be seen that the more dense the population (i.e., more carbon dioxide) and the closer the distance to a petrification-industry zone (i.e., air pollution), the more serious the neutralization damage. Figure 5 shows that the petrochemical industry area in Yunlin and Kaohsiung and some northern areas with a high population density have the apparent neutralization reaction. The hazard map of reinforcement corrosion such as Figures 4 and 5 could benefit not only from a durability evaluation of existing bridges but also life-cycle-based performance design of new bridges.

Conclusions

A hazard map of reinforcement corrosion of RC bridges in Taiwan was established on a $1\text{km}\times 1\text{km}$ grid base. The climate information relating to corrosion models of chloride invasion and neutralization in each grid is taken into account. Under natural circumstances, the time required for a specific loss ratio of the effective cross-sectional area of reinforcement can be displayed on the map of Taiwan. The conclusions obtained can be drawn as follows:

1. For durability evaluation of existing bridges, the relationship between the effective cross-sectional area of reinforcement and the service time can be obtained. Accordingly, the deterioration of structural performance such as bending strength, shear strength, or deflection accompanied with service time can also be displayed for the grid where the existing bridge is located. This can benefit the bridge management institute in setting threshold values of time for repairing or retrofitting.

2. For the case of a new bridge design, the developed hazard map gives direct instructions on determining the concrete cover, concrete strength, and reinforcement required to achieve a satisfactory service time. In addition, a design table related to the different sets of the abovementioned data with the corresponding service time can be established for durability design. The developed hazard map gives not only qualitative but also quantitative expressions of structural performance and benefits life-cycle-based design of bridges.

References

- Architectural Institute of Japan (AIJ) (2004). *Durable design and construction guidelines of reinforced concrete buildings (draft)*, Japan. (in Japanese)
- Chen, S.D. (2015). *Establishment and Application of Corrosion Hazard Map on Reinforcement of Reinforced Concrete Bridges*, Thesis, National Taipei University of Technology, Taiwan, 2015. (in Chinese.)
- Chiu, C.N. and Lin, P.H. (2004). Spatial Interpolation of Air Temperature and Precipitation from Meteorological Stations at Taiwan, *Atmospheric Sciences*, 32 (4), 329-350. (in Chinese)
- Chiu, Y.F., Lo, C.M., Chen, K.C., Ko, J.L. and Hsieh, M.J. (2014). *2013 Atmosphere Corrosive Factors Data---Annual Report*, Taipei: Harbor & Marine Technology Center. (in Chinese)
- Chuang, Y.T. (2012). *Life-Cycle Seismic Performance Evaluation for Deteriorating RC Shear Walls*, Thesis, National Taiwan University of Science and Technology, Taiwan. (in Chinese.)
- Japan Concrete Institute (JCI) (2004). *Symposium on Long-term Performance According to Support Model of Concrete Structures*, Japan. (in Japanese)
- Japan Society of Civil Engineers (JSCE) (2008). *Achievement Report of Concrete Structures Research Subcommittee on Reliability Design*, Japan. (in Japanese)
- Niu, D.T. (2003). *Durability and life forecast of reinforced concrete structure*, Beijing: Science Press. (in Chinese)
- Siao, F.P., Chiu, C.K. and Tu, F.J. (2012). *Seismic performance evaluation for deteriorating and earthquake-damaged RC school buildings (NCREE-12-018)*, Taipei: National Center for Research on Earthquake Engineering (in Chinese).
- Sung, Y.C. and Su, C.K. (2011). Time-dependent Seismic Fragility Curves on Optimal Retrofitting of Neutralized Reinforced Concrete Bridges, *Structure and Infrastructure Engineering*, 7 (10), 797-805.
- Sung, Y.C., Hsu, C.C., Hung, H.H. and Chang, Y.J. (2013). Seismic Risk Assessment System of Existing Bridges in Taiwan, *Structure and Infrastructure Engineering*, 9 (9), 903-917
- Sung, Y.C., Huang, C.H., Liu, K.Y., Wang, C.H., Su, C.K. and Chang, K.C. (2010). Life-Cycle Evaluation on Deteriorated Structural Performance of Neutralized Reinforced Concrete Bridges, *Structure and Infrastructure Engineering*, 6 (6), 741-75
- Weyers, R.E. (1998). Service life model for concrete structures in chloride laden environments, *ACI Materials Journal*, 95 (4), 445-453.

Experimental Study on Post-Tensioned Rocking Columns with Replaceable Energy Dissipaters

Hsiao-Hui Hung¹ and C. W. Huang², C. R. Jiang³ and P. X. Luo⁴

洪曉慧¹、黃仲偉²、江奇融³、羅培軒⁴

Abstract

To mitigate the column damage during seismic events and to reduce the recovery time after a major earthquake, a post-tensioned bridge column with a rocking interface above the foundation and externally-installed energy dissipation devices was proposed. The energy dissipation devices were specially designed to serve as fuse elements that can be easily replaced after yielding. In addition, a mechanical joint that can rotate freely in all directions was incorporated at one end of the dissipater to ensure bending was not transmitted into this device. To verify the seismic performance of the proposed system, two proposed specimens with different prestressing forces and design details in the rocking base were constructed and tested at the National Center for Research on Earthquake Engineering (NCREE) in Taiwan. From the experiments, it was found that the proposed post-tensioned specimens suffered minor damage after cyclic loadings. All of the damage was concentrated on the inelastic deformation that occurred at the external energy dissipaters. The ease of replacement for the external energy dissipaters was also confirmed. However, the stiffness of the proposed system was less than that of the conventional cast-in-place monolithic specimen.

Keywords: rocking mechanism, prestressing forces, energy dissipation device

Introduction

In the wake of the rapid economic growth and advancements in design technology seen in recent years, the seismic design philosophy of bridges has gradually evolved from the assurance of life-safety by preventing collapse during a major earthquake to the maintenance of acceptable serviceability after a major seismic event. Previously, the mainstream seismic design methodology for bridges was ductility design by allowing bridges to deform inelastically to dissipate energy and maintain appropriate strength during severe earthquake attack. Thus, after a severe earthquake, bridge columns have most likely suffered severe damage and traffic interruption is unavoidable while bridges are retrofitted or rebuilt. As a consequence, in order to ensure post-earthquake functionality and to reduce the retrofit cost, designs that reduce the residual displacements and enhance the

residual performance of the bridge after an earthquake have become crucial for the new generation of seismic design for bridges. According to a previous study, the rocking mechanism of a properly designed shallow foundation can effectively reduce the seismic demand, and thereby prevent the severe damage of a column at the plastic hinge area (Hung et al. 2014). However, a pure rocking mechanism lacks reliable energy dissipation mechanisms and may induce large displacements. In order to enjoy the advantages of a rocking mechanism while preserving proper energy dissipation capacity and having a controllable rocking motion, the use of unbonded post-tensioned/pre-tensioned columns with rocking interfaces and supplemental energy dissipation devices has become a promising solution (Roha and Reinhorn 2010, Palermo and Mashal 2012, Mohamed and Ahmad 2011). Based on a similar concept, this study proposed a post-tensioned rocking column with external energy

¹ Research Fellow, National Center for Research on Earthquake Engineering, hhung@narlabs.org.tw

² Associate Professor, Department of Civil Engineering, Chung Yuan Christian University

³ Research Assistant, National Center for Research on Earthquake Engineering

⁴ Graduate Student, Department of Civil Engineering, Chung Yuan Christian University

dissipaters. The column is prestressed by unbonded post-tensioned tendons to ensure self-centering behavior and the supplemental energy dissipaters are easily replaced to reduce post-earthquake recovery time for bridges. The energy dissipaters were obtained from steel bars with a reduced diameter over a specific length and the dissipation was provided by the hysteresis of the material due to axial elongation. To ensure that the dissipater was only subjected to axial forces and bending was not transmitted into the dissipaters, a mechanical joint that can rotate freely in all directions is also incorporated at one end of the dissipaters. To investigate the seismic performance of the proposed system, two specimens with different prestressing forces and rocking base details were constructed and tested at NCREE. For comparison, a conventional cast-in-place monolithic column specimen without connections was also constructed and tested.

Specimen Design

Two post-tensioned bridge column specimens denoted as RB-P1 and RB-P2 were prefabricated at NCREE. These two specimens differed in post-tensioning forces and design details in the rocking base as shown in Fig 1 (a) and (b). The design post-tensioning forces for RB-P1 and RB-P2 were $0.04f_c'A_g$ and $0.07f_c'A_g$, respectively. Herein, A_g is the gross cross-sectional area of the column, and f_c' is the concrete compressive strength of the column. In addition, specimen RB-P2 had a 60 cm square neoprene pad with a thickness of 3 cm placed at the interface between the foundation and the bottom segment to release the high compression forces that may arise at the rocking toes. In order to realize the seismic resistance of the current proposed system as compared to the one with the conventional design details, a conventional cast-in-place monolithic column specimen without connections (BM01) was also constructed and tested. As can be observed in Fig. 1, all these specimens are 3.6 m in effective height with a cross section of 60 cm \times 60 cm. The equivalent monolithic specimen BM01 was reinforced with 16-D19 SD420 rebars and transversely reinforced with D13@10 cm perimeter hoops and internal stirrups. Both RB-P1 and RB-P2 specimens were reinforced with 12-D19 SD420 rebars and one tendon. However, only tendons were passed through the interface between the column and foundation. The tendons for specimens RB-P1 and RB-P2 comprised of 8 and 12 seven-wire strands, respectively. The strands were made of steel equivalent to ASTM A416 Grade 270 and each strand had a nominal diameter of 15.2 mm.

Both post-tensioned specimens RB-P1 and RB-P2 were precast in advance and were separated into 3 segments, including two precast column segments and a precast foundation. The height of the bottom column segment and the top column segment are 2 m and 1.94 m, respectively. Each column segment was precast with one 15 cm polyvinyl chloride (PVC) duct within

the center to allow tendons to pass through. In addition, both the bottom column segment and the foundation were precast with several threaded rods in the proper locations for the subsequent connection with the external replaceable energy dissipaters. To provide protection for the highly strained cover concrete during rocking, the edge of the rocking base of the precast column element was chamfered to a chamfer distance of 5 cm. In addition, 5 mm steel plates were cast into the top surface of the foundation and the bottom surface of the bottom column segment to give the rocking surface sufficient strength for repeated rocking motions.

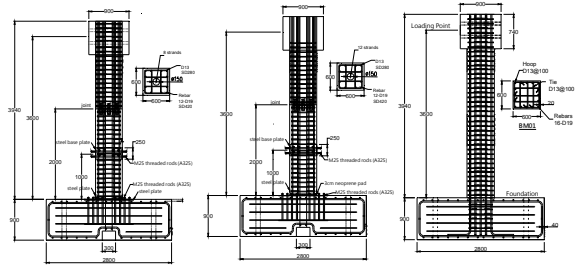


Fig. 1. Design details of specimens (a) RB-P1 (b) RB-P2 (c) BM01 (unit: mm)

Specimens RB-P1 and RB-P2 were constructed by stacking precast segments on top of each other with reinforcing bar passing through the interface between two column segments and then connecting the assembly structure with tendons. After the tendons were prestressed to a predetermined value, and the axial forces representing the dead load of the superstructures were applied, the energy dissipaters were externally installed to the precast specimens.

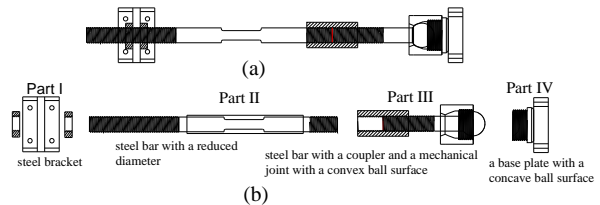


Fig. 2. Design details of the energy dissipaters: (a) fully assembled view (b) exploded view

Fig. 2 schematically shows the design details of the energy dissipaters. For the ease of replacement, the energy dissipater was separated into 4 parts and connected by mechanical joints or bolts. The major part (Part II) was fabricated from 32 mm JIS S450 steel bar with a fused diameter of 20 mm over a length of 220 mm. A 40 mm (outside diameter) steel tube, with a wall thickness of 2 mm, was located over the machined area and epoxy was injected into the space between the tube and bar. The top end of Part II was bolted to a steel bracket (Part I) that was mounted on the side of the precast column. Part III was connected to Part II and Part IV by couplers. Part IV was bolted to the top of the foundation through the precast threaded rods. A specially designed mechanical joint that can rotate freely in all directions was located between Part III and Part IV. Prior to the specimen

testing, the energy dissipaters were tested to characterize their energy dissipation capacity. The cyclic loading test results are given in Fig. 3.

Experimental Program

In order to investigate the seismic performance of the proposed column system, cyclic loading tests were conducted at NCEE. Fig. 4 illustrates the test setup. Four high tensile strength tie-down rods were placed through the footing and anchored into the strong floor of the laboratory to simulate the fixed-base condition of the foundation. During the test, an axial load of 1260 kN was applied to the test column through a tap beam using two vertical high tensile strength rods. The vertical loading was kept constant throughout the test to simulate the tributary dead load of the deck, which was around $0.1f_c'A_g$. In addition, one horizontal actuator was used to apply the lateral force to the column's top to simulate the seismic loading. The location of the application force was 3.6 m up from the top of the footing. Displacement-controlled cyclic loading testing was performed on these specimens. Fig. 5 (a) and (b) show the displacement loading protocol for the test of the post-tensioned specimens and the monolithic test specimen, respectively. In addition, in order to verify the replaceability of the external energy dissipaters, two cyclic tests were conducted on each of the post-tensioned specimens. The first cyclic test stopped after the third cycle of 3.5% drift. At this instant, the outermost energy dissipaters were expected to rupture. Thus, all the energy dissipaters were replaced and the second cyclic test was performed. It should be noted that only the major part of the energy dissipater, i.e., Part II as shown in Fig. 2, needs to be replaced. The other parts can remain in use. The first test and second test of specimen RB-P1 are denoted as RB-P1-1 and RB-P1-2, respectively. Similarly, tests for specimen RB-P2 are denoted as RB-P2-1 and RB-P2-2.

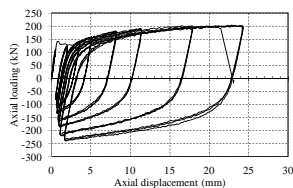


Fig. 3. Cyclic testing results of the energy dissipaters



Fig. 4. Schematics of the experimental setups

Test Results

The measured post-tensioning force histories during the tests for the post-tensioned specimens are given in Fig. 6. The design prestressing forces for specimens RB-P1 and RB-P2 were $0.04f_c'A_g$ (494 kN) and $0.07f_c'A_g$ (864 kN), respectively. However, loss of prestressing forces was observed during the tests due

to mechanical take-up of the tendon anchorages as the load in the tendon increased. Fig. 7 shows the load-displacement curve for each specimen. For tests RB-P1-1 and RB-P2-1, the outermost external energy dissipaters started to fracture at a drift of 3.5% and a sudden loss in strength can be observed in the load-displacement curves. The tests stopped after the second cycle of the 3.5% drift. At this point, all the energy dissipaters were replaced with new ones and the second tests were performed. The test results for the second tests are also given in Fig. 7. As can be seen, the hysteresis behavior for the second tests was almost consistent with that of the first tests as the drift ratio was less than or equal to 3.5. This observation confirmed the advantage of the external energy dissipaters after a strong earthquake.

For the second test, as the drift ratio continued to increase, the strength of the column gradually decreased as the energy dissipaters fractured successively. After the second cycles of 6% drift, all of the energy dissipaters had ruptured. However, the entire vertical load bearing capacity of the system was still maintained at this time due to the strength contribution from the prestressing forces. By comparing the hysteretic curves of the proposed specimens in Fig. 7(a) and (b) with that of the specimen BM01 given in Fig. 7(c), specimen BM01 exhibited more energy dissipation as its hysteresis curve seems fuller. However, the residual displacements for the proposed specimens were much smaller than that of specimen BM01. Both specimens RB-P1 and RB-P2 exhibited flag-shaped hysteretic behavior. The nonlinear behavior was a result of the opening at the rocking base and the material nonlinearity that resulted from the action of the energy dissipaters. However, the stiffness for the post-tensioned specimens was also much smaller than that of specimen BM01.

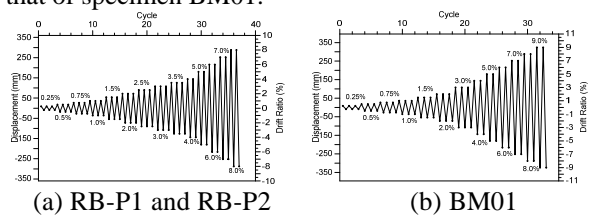


Fig. 5. Loading protocol

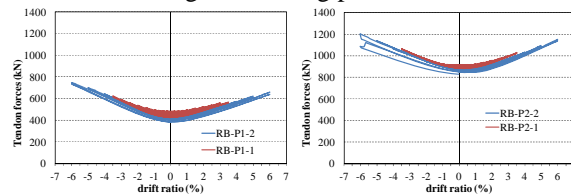


Fig. 6. Tendon forces versus drift ratio

Fig. 8 shows the distribution of the rotation increment along the height of the columns after the excitation of the first cycle for each drift ratio. The rotation increment was obtained by taking the difference between the readings of two adjacent tiltmeters. Because the rotation of the foundation was

assumed to be zero, the bottommost values in Fig. 8 included the influence of joint opening. It is obvious that the contribution of the rotation was mainly due to the joint opening at the column base for specimens RB-P1 and RB-P2. For instance, the rotation increments at the column base were 0.059 and 0.054 radians at the drift ratio of 6 for specimens RB-P1 and RB-P2, respectively. These values were nearly equal to the total rotation of the columns. This result also implies that the curvature at the column itself was rather small and the damage to the column was rather minor. On the other hand, the rotation increment of specimen BM01 was much larger than that of the post-tensioned specimens as the influence of interface opening was excluded. This observation implies that the curvature of the conventional monolithic column specimen was much larger than of the precast post-tensioned specimens and that the conventional column suffered more damage at the plastic hinge area. Furthermore, by comparing specimen RB-P1 to RB-P2, it can be seen that joint between the foundation and the bottommost segment of RB-P1 experienced larger opening than the corresponding joint in RB-P2. This implies that a higher axial force decreased the percentage contribution to the total column rotation from the column base. This is because a higher axial force would restrain the uplift of the of the column base.

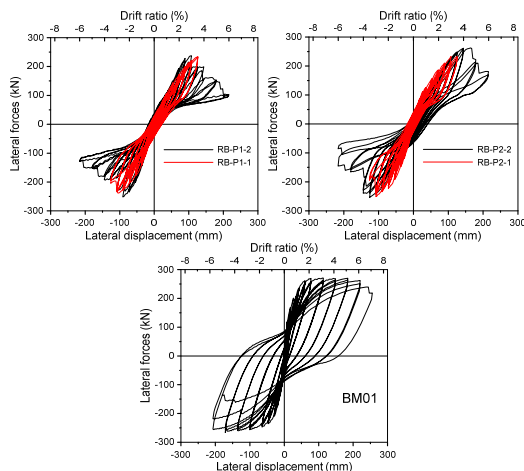


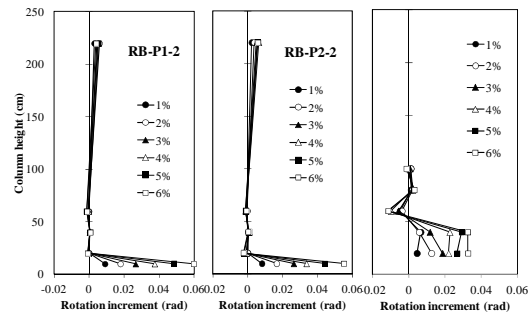
Fig. 7. Load-displacement hysteretic curves

A similar conclusion can also be drawn from the failure photos taken after the excitation of 6% drift, as shown in Fig. 9. For RB-P1, the damage was limited to a minor crack of the cover concrete. For RB-P2, where a neoprene pad was inserted between the rocking base and the foundation, only hairline cracks can be observed. The damage observed in these specimens can be easily repaired and the strength and ductility of the column can be restored after the replacement of energy dissipaters. On the other hand, at the end of the test for BM01, both vertical and transverse reinforcements were exposed, many longitudinal bars were buckled, and the bulging of the rectilinear hoops caused by the large lateral dilation of the concrete was severe. This kind of damage is not

easily repaired immediately after an earthquake.

Conclusions

This paper investigates the seismic behavior of two post-tensioned rocking column specimens with replaceable energy dissipaters by performing cyclic loading tests. From the experimental results comparing these two specimens with an equivalent monolithic cast-in-place ductile column specimen, the benefits of the rocking column base in limiting damage to the column and external energy dissipater in absorbing earthquake energy were recognized. The advantage of the external energy dissipaters being replaceable after a strong earthquake was also confirmed.



(a) RB-P1 (b) RB-P2 (c) BM01

Fig. 8. Rotation increment for specimens at different drift ratios



(a) RB-P1 (b) RB-P2 (c) BM01

Fig. 9. Photographs of the specimens after cyclic loading tests.

References

- Hung, H.H., Liu, K.Y. and Chang, K.C., Rocking behavior of bridge piers with spread footings under cyclic loading and earthquake excitation, *Earthquakes and Structures*, 7(6), 1001-1024, 2014.
- Roha, H., and Reinhorn, A.M., Modeling and seismic response of structures with concrete rocking columns and viscous dampers, *Engineering Structures*, 32(8), 2096–2107, 2010.
- Palermo, A., and Mashal, M., Accelerated bridge construction (ABC) and seismic damage resistant technology: a New Zealand challenge, *Bulletin of the New Zealand Society for Earthquake Engineering*, 45(3), 123-134, 2012.
- Mohamed A.E., and Ahmad S., Seismic behavior of self-centering precast segmental bridge bents, *Journal of Bridge Engineering*, 16(3), 328-339, 2011.

Experimental and Design Investigation of a Viscous Damper Filled with Shear Thickening Fluids

Fang-Yao Yeh¹, Chung-Han Yu², Kuo-Chun Chang³ and Tsung-Wu Chen⁴

葉芳耀¹、游忠翰²、張國鎮³、陳宗斌⁴

Abstract

This paper studies the rheological properties of shear thickening fluids (STFs) and the performance of a viscous damper filled with an STF by performing a cyclic loading test. A hydraulic steel tube was filled with an STF to develop an innovative passive damper device. A performance test of this device showed that the area and shape of hysteresis loops can vary with different loading conditions. In addition, the hysteresis loops of the developed STF damper under various loading conditions were observed. The experimental results and theoretical study showed that STF-filled dampers are potentially useful in practical engineering applications.

Keywords: Shear thickening fluid; STF-filled damper; Non-linear viscous damper

Introduction

The seismic response of structures can be reduced appropriately by the installation of damper devices. However, dampers deployed on buildings or bridges are generally designed only for specific structural systems under specific loading conditions. Therefore, several researchers have developed adjustable passive dampers in recent years [1, 2]. Electrorheological (ER) dampers and magnetorheological (MR) dampers are well-known adjustable damper systems, but the durability and stability of the external power supply needed for these are insufficient for long-term application during the structure's service life. Consequently, a new material, shear thickening fluid (STF), which changes its properties according to different loading rates without external power needed, is considered to be a good filling material for innovative damper devices [3]. Lee et al. [4] applied STF to develop liquid body armor, which is a bulletproof material with flexibility. Fisher et al. [5] focused on the feasibility of integrating STF into a composite sandwich structure that can lead simultaneously to changes in stiffness and damping under dynamic loading as the strain and/or frequency

are varied.

This paper studies the feasibility of applying STF materials to a conventional viscous damper device by using a simplified piston device and changing the concentration of the STF fill to develop an innovative passive damper that behaves similar to an MR damper. In this study, STF samples composed of nanosized fumed silica particles suspended in a solvent polypropylene glycol (PPG) were fabricated in the laboratory. The shear properties of STF samples under the steady state and the oscillatory state were tested separately using a rheometer. Furthermore, a prototype STF damper was developed and tested with preliminary performance experiments. In addition, hysteresis loops of the STF damper developed under various loading conditions were observed. The results show the feasibility of the STF damper proposed in this study and indicate that it might have good potential in practical engineering applications.

¹ Research Fellow, National Center for Research on Earthquake Engineering, fyyeh@ncree.narl.org.tw

² Ph. D. Student, Department of Civil Engineering, National Taiwan University

³ Director, National Center for Research on Earthquake Engineering,
Professor, Department of Civil Engineering, National Taiwan University

⁴ Ph. D., Department of Civil Engineering, National Taiwan University

Principles of Fluid Mechanics in Viscous Fluid Dampers

The mechanical behavior of viscous dampers can be described by the equation $F_D = C|\dot{u}|^\alpha \text{sgn}(\dot{u})$, where F is the damping force produced by the damper, C is the damping coefficient of the damper, $|\dot{u}|$ is the velocity of the piston head movement, and α is the nonlinearity coefficient. Consequently, the damping force is only related to the relative velocity and does not have a stiffness effect. When the damper is at its highest velocity, the relative displacement of its two sides is minimum and the damping force is maximum. When the velocity of the damper is zero, the relative displacement of its two sides is maximum and the damping force becomes zero.

If an axial force, F , acts on the damper, it causes an inner pressure difference ΔP and a piston movement velocity v_0 . The relationship between the force and the pressure difference will be $F_D = \Delta P \times A_p$, where A_p is the cross-sectional area of the piston and ΔP is the pressure difference between both sides of the piston head. If the width of the region in which the viscous fluid flows between the piston and the steel tube is d , which is much smaller than R , the radius of the piston, the annular section of the cross-section can be approximated as a thin rectangular section of width $b \approx 2\pi(R - d/2)$. In this way, the fluid can be regarded as flowing between two parallel plates. Wereley and Pang [6] proposed that, for such a fluid motion between parallel plates and the variation of ΔP between the intervals of the fluid action section, L , the boundary conditions decrease linearly. This theory was proven experimentally. Based on the theoretical derivation of Poiseuille flow, the following assumptions can be made: (1) the width of the zone of fluid action is small compared with the tube diameter; (2) the fluid is incompressible; (3) if the fluid properties are assumed to be homogenous between the interval of the fluid action section (L), it can be seen as a one-dimensional problem; and (4) the fluid is in the laminar flow state, so the acceleration changes can be ignored. In this way, the pressure difference in the interval L is a linear change. The governing equation for Poiseuille flow can therefore be simplified as $d\tau/dy = -\Delta P/L$, where τ is the shear stress. Fig. 1a shows the stress distribution at the orifice.

The continuity equation for Newtonian fluids between two parallel plates is $\tau = \mu \frac{dv}{dy} = \mu \dot{\gamma}$, where v is the function of velocity of the parallel plates along the y -axis and μ is the viscosity coefficient. Fig. 1b shows the relationship between shear stress and shear strain. The gradient of the curve is the viscosity coefficient μ .

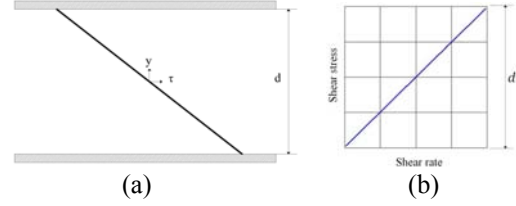


Fig. 1 (a) Distribution of shear stress at the orifice, (b) a plot of shear stress vs. shear rate at the orifice

STFs have the following properties. If the shear strength exceeds the yield stress and the viscosity of the fluid after yielding is smaller than before, the fluid loses viscosity with increasing shear strength. This is called shear thinning behavior. Alternatively, if the shear strength exceeds the yield stress and the viscosity of the fluid after yielding is greater than before, the fluid will become highly viscous as the shear strength increases. This is called shear thickening behavior. Fig. 2 shows the relationship between shear stress and shear strain of the STF.

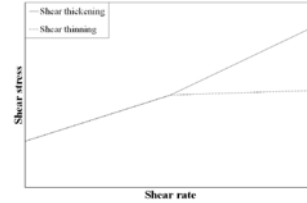


Fig. 2 Shear stress vs. shear strain rate for shear thickening and thinning fluids

The equation describing the relationship between the shear strength and the shear strain of a viscous fluid can be divided into two parts—before the yielded state, as shown in equation (1), and after yielding, as shown in equation (2):

$$\tau = \mu_{pr} \frac{dv}{dy} \quad \tau \leq \tau_y \quad (1)$$

$$\tau = \tau_y + \mu_{po} \left(\frac{dv}{dy} - \dot{\gamma}_y \right) \quad \tau \geq \tau_y \quad (2)$$

where μ_{pr} and μ_{po} refer to the viscosity before and after the yielding, respectively, and $\dot{\gamma}_y$ is the shear strain rate at the time of yielding. Integrating the equations (1) and (2) with respect to the state areas of the two types of flow velocity, equations (3) to (6) can be obtained as follows:

$$\frac{dv_{pr}}{dy} = -\frac{\Delta P}{L\mu_{pr}} y + A_1 \quad \tau \leq \tau_y \quad (3)$$

$$v_{pr} = -\frac{\Delta P}{2L\mu_{pr}} y^2 + A_1 y + A_2 \quad \tau \leq \tau_y \quad (4)$$

$$\frac{dv_{po}}{dy} = -\frac{\Delta P}{L\mu_{pr}} y + B_1 \quad \tau \leq \tau_y \quad (5)$$

$$v_{po} = -\frac{\Delta P}{2L\mu_{pr}} y^2 + B_1 y + B_2 \quad \tau \geq \tau_y \quad (6)$$

These simultaneous equations have four boundary conditions: the viscosity of the fluid at the edges of the parallel plates is zero; the rate of change in the flow velocity at the central orifice is zero; and in accordance with the continuity property of fluid, the

flow velocity at the junction of the two areas is equal to the rate of change in the flow velocity of the fluid. Solving these equations produces A_1 , A_2 , B_1 , and B_2 :

$$A_1 = 0 \quad (7)$$

$$A_2 = \frac{\Delta P \delta^2}{8L} \left(\frac{1}{\mu_{po}} - \frac{1}{\mu_{pr}} \right) - \frac{\Delta P \delta d}{4L} \left(\frac{1}{\mu_{po}} - \frac{1}{\mu_{pr}} \right) + \frac{\Delta P d^2}{8L \mu_{po}} \quad (8)$$

$$B_1 = \frac{\Delta P \delta}{2L} \left(\frac{1}{\mu_{po}} - \frac{1}{\mu_{pr}} \right) \quad (9)$$

$$B_2 = \frac{\Delta P d^2}{8L \mu_{po}} - \frac{\Delta P \delta d}{4L} \left(\frac{1}{\mu_{po}} - \frac{1}{\mu_{pr}} \right) \quad (10)$$

in which $\delta = 2L \tau_y / \Delta P$.

By substituting A_1 , A_2 , B_1 , and B_2 into equations (4) and (6), the flow velocity type of a damper filled with a bi-viscosity fluid can be known. Equation (11) is the flow velocity equation of the area before yielding, while equation (12) is the same after yielding

$$v_{pr} = -\frac{\Delta P}{2L \mu_{pr}} y^2 + \frac{\Delta P \delta^2}{8L} \left(\frac{1}{\mu_{po}} - \frac{1}{\mu_{pr}} \right) - \frac{\Delta P \delta d}{4L} \left(\frac{1}{\mu_{po}} - \frac{1}{\mu_{pr}} \right) + \frac{\Delta P d^2}{8L \mu_{po}} \quad (11)$$

$$v_{po} = -\frac{\Delta P}{2L \mu_{po}} y^2 + \frac{\Delta P \delta}{2L} \left(\frac{1}{\mu_{po}} - \frac{1}{\mu_{pr}} \right) y + \left[\frac{\Delta P d^2}{8L \mu_{po}} - \frac{\Delta P \delta d}{4L} \left(\frac{1}{\mu_{po}} - \frac{1}{\mu_{pr}} \right) \right] \quad (12)$$

Integrating the two flow velocity areas produces the equation for the flow at a unit time:

$$Q = \frac{\Delta P b d^3}{24L \mu_{po}} \left[(1 - \bar{\delta})^2 (1 + 2\bar{\delta}) + \bar{\mu} \bar{\delta} (3 - \bar{\delta}^2) \right] \quad (13)$$

The index $\bar{\mu}$ is the ratio of the viscosity before yielding to that after yielding, and $\bar{\delta} = \delta/d$, where d is the thickness between the parallel plates.

The damping force in equation (14) and the damping coefficient in equation (15) can be obtained from $F_D = C V_0 = \Delta P A_p$.

$$F = \frac{12 A_p^2 L \mu_{po}}{b d^3} \left[(1 - \bar{\delta})^2 (1 + 2\bar{\delta}) + \bar{\mu} \bar{\delta} (3 - \bar{\delta}^2) \right] \times v_0 \quad (14)$$

$$C = \frac{12 A_p^2 L \mu_{po}}{b d^3} \left[(1 - \bar{\delta})^2 (1 + 2\bar{\delta}) + \bar{\mu} \bar{\delta} (3 - \bar{\delta}^2) \right] \quad (15)$$

Performance Test of STF Damper

The mechanism of the STF damper we developed is similar to that of a conventional single-tube damper that consists of a piston, one flow tunnel, and a cylinder. The STF damper consists of four part elements: the cylinder, piston head, oil seal, and fluid. The photo of the experimental layout of the dynamic performance tests is shown in Fig. 3.



Fig. 3 Layout of the STF damper performance test

In this paper, the 10% w/w STF damper was tested under two conditions of harmonic excitations. The first condition was different frequencies at a constant stroke; the test frequency values were 0.1 Hz, 0.3 Hz, 0.5 Hz, 1 Hz, and 3 Hz at a constant stroke of 1 mm, 5 mm, 10 mm, and 15 mm. The second condition was varying strokes at a constant frequency; the test stroke values were 1 mm, 5 mm, 10 mm, and 15 mm at a constant frequency of 0.1 Hz, 0.3 Hz, 1 Hz, and 3 Hz.

The experimental results in terms of the damping force versus the displacement at different frequencies are shown in Figs. 4 and 5. For each test, six cycles were repeated, and average values were taken to obtain the stabilized hysteresis loops. As can be seen from Figs. 4 and 5, the shape of the displacement damping force loop is strongly dependent on the loading frequency. For example, the peak damping force shows an increasing trend with frequency. In the low frequency range, such as 1 Hz, the STF presents a Newtonian fluid character. The area of the hysteresis loop per cycle denotes the energy dissipation capability. As the excitation frequency increases, the slope of the low velocity hysteresis loop increases. At low viscosity, the damper works in the transition state and in the shear-thickened state when the excitation frequency is at 3 and 5 Hz, respectively. The hysteresis loop changes significantly as the excitation frequency passes 1 Hz.

Furthermore, the results of the performance test under various excitation frequencies and strokes are shown in Tables 1 and 2. Clearly, the STF-filled damper device has various damping coefficients with different loading frequencies. Fig. 6 shows the force and velocity relationship of the 10% w/w STF damper with R972 nanoparticles. By applying the derived design formula, equations (14) and (15), we obtain the relation between the damping force and velocity of the STF damper. These values are compared with the experimental results as shown in Fig. 7.

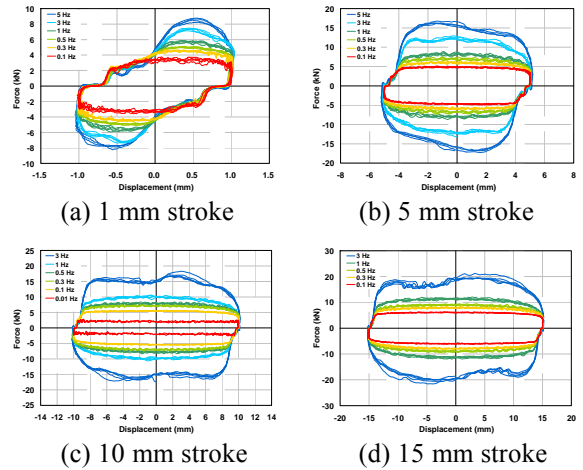


Fig. 4 Hysteresis loop of the 10% (w/w) STF damper (Frequencies 0.1 Hz–3 Hz)

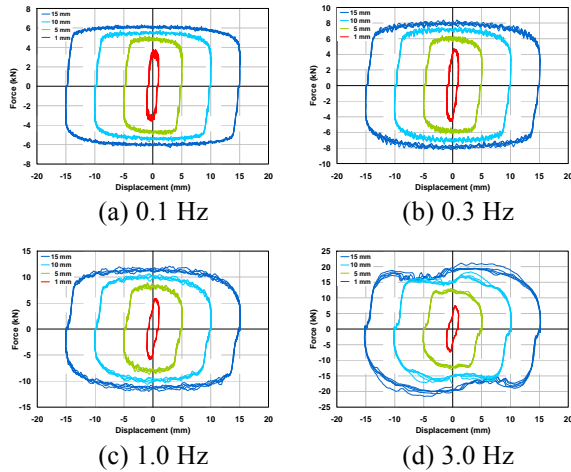


Fig. 5 Hysteresis loop of the 10% (w/w) STF damper (1 mm–5 mm stroke).

Table 1 Damping coefficient and index of the 10% (w/w) STF damper under various excitation frequencies

Stroke (mm)	Frequency (Hz)	Maximum force (kN)	Damping coef. C (kN (s/mm) ^α)	Damping index α
10	0.1	5.738	3.857	0.187
10	0.3	7.484	3.603	0.228
10	1.0	10.627	0.870	0.598
10	3.0	16.289	1.266	0.494

Table 2 Damping coefficient and index of the 10% (w/w) STF damper under various strokes

Stroke (mm)	Frequency (Hz)	Maximum Force (kN)	Damping coef. C (kN (s/mm) ^α)	Damping index α
1	3.0	4.546	4.555	0.136
5	3.0	13.199	1.161	0.591
10	3.0	16.289	1.266	0.494
15	3.0	18.597	1.118	0.521

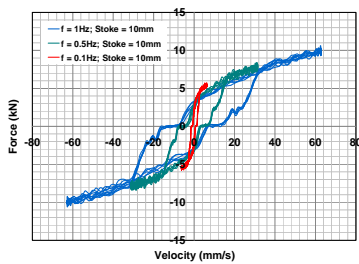


Fig. 6 Force vs. velocity of the 10% (w/w) STF damper filled with R972 nanoparticles.

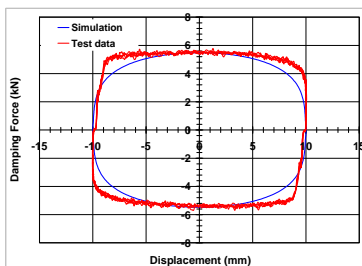


Fig. 7 Comparison of the experimental results and hysteresis loop of the STF damper obtained from design formulas

Concluding remarks

In this study, a hydraulic steel tube was filled with an STF to develop an innovative passive damper device. The STF damper presents nonlinear damper characteristics under different loading frequencies. By applying such a characteristic, the developed device can be used for structural semi-passive control applications under different loading criteria. The preliminary experimental results proved the feasibility of the STF-filled damper device.

The rheological test showed that a mixture of nanoparticles (R972) and polyethylene glycol can provide high rheological behavior. The performance of the STF damper can then be modified by the rheological properties of shear thickening and thinning.

The current STF mixture can be used as a liquid medium for viscous dampers. The results of the performance tests suggest that the STF-filled viscous damper can provide $\alpha < 1$ nonlinear behavior, similar to that of an MR damper device, without the need for electricity.

Development of intelligent viscous dampers can satisfy the need for structural control in multiple structures. The intelligent viscous damper can change the damping coefficient and the energy dissipation at different stroke and vibration frequencies. It can also be designed to meet the various requirements of shock resistance of buildings.

References

- Wereley N M, Lindler J, Rosenfeld N and Choi Y T 2004 *Smart Mater. Struct.* 13:4 743
- Dimock G A, Yoo J H and Wereley N M 2002 *Journal of Intelligent Material Systems and Structures* 13:9 549
- Zhang X Z, Li W H and Gong X L 2008 *Smart Mater. Struct.* 17:3 35
- Lee Y S, Wetzel E D, Egres Jr. R G and Wagner N J 2002 23rd Army Science Conference (Orlando, FL.)
- Fisher C, Braun S A, Bourban P E, Michaud V, Plummer C J G and Manson J A E 2006 *Smart Mater. Struct.* 15:5 1467
- Wereley N M and Pang L 1998 *Smart Mater. Struct.* 7:5 732

Reliability-based Design Method for Scoured Bridges

Chun-Chung Chen¹, Chun-Jen Liu², Kuo-Chun Chang³ and Tsu-Chun Tseng⁴

陳俊仲¹、劉俊仁²、張國鎮³、曾子俊⁴

Abstract

There are many reasons for the failure of a crossing bridge. Domestic and international studies have pointed out that one of the main reasons is scour events. In existing bridge design codes, the scouring effect is not considered as a load effect. When considering multiple-hazard reliability design, engineers face problems with load and resistance factor design (LRFD) that do not consider the scouring effect as a load. This study offers a novel approach of transferring the scouring effect into a load pattern and applying load combinations, yielding a more direct design method.

This research continues on from previous results, starting with the concept of an equivalent scour load. We propose two applications of equivalent scour load: one is building a scour fragility curve, the other is calculating the load factors of multiple-hazard LRFD. The objective is to help engineers to evaluate and design a crossing bridge with scour events. We use a Monte Carlo method to simulate hazards and evaluate bridge failure probability with conditional probability. Finally, we obtain the scour fragility curve in order to calculate the load factors in multiple-hazard LRFD through reliability analysis.

After developing a scour fragility curve, engineers can quickly obtain the failure probability versus scour depth. The load factor of the multiple-hazard LRFD can be used in the design of a crossing bridge, which will make the design procedure smoother.

Keywords: bridge scouring, equivalent scour load, scour fragility curve, multiple-hazard load and resistance factor design.

Introduction

Numerous major natural disasters have occurred worldwide in recent years. Hurricane Katrina caused catastrophic damage to New Orleans in the United States in 2005, and the torrential rain from Typhoon Morakot triggered mudslides and severe flooding throughout the central and southern regions of Taiwan in 2009. Because such natural disasters typically lead to substantial loss of human life and property, scholars worldwide have begun investigating the effects of multiple disaster events on the safety of bridge structures. The results of such studies have also been incorporated into developing structural designs and regulations. To ensure the safety of bridges exposed to multiple disasters, G.C. Lee et al. (2014) proposed using the scour effect as an equivalent static load and incorporated this equivalent load it into a design

equation. A cooperative research between Taiwan and US was established to attempt to look into the nature of bridge failures produced by the effects of the occurrence of individual extreme hazards or their possible combinations and the consistency of bridge design principles used in handling these load effects.

This study comprises three parts. In the first part, an equivalent static scour model is established. Because scour depth is an issue that engineers examine following bridge scouring, this study aims to identify a relationship for converting scour depth into a corresponding equivalent static load, which can be compared with other types of load (e.g., static load and live load). In addition, a lateral bearing capacity test is conducted on a downscaled bridge pier to verify the proposed equivalent scour load model. In the second part of this research, combinations of static

¹ Associate Researcher, National center for Research on Earthquake Engineering, jingochen@narlabs.org.tw

² Graduate Student, Department of Civil Engineering, National Taiwan University

³ Director, National Center for Research on Earthquake Engineering

⁴ Research Assistant, Department of Civil Engineering, National Taiwan University

and live loads are incorporated into the proposed equivalent scour load model, as given by

$$\phi R > \gamma_{DL} \times DL + \gamma_{LL} \times LL + \gamma_{SC} \times SC \quad (1)$$

Reliability analysis is performed to calculate the reduction coefficient of the bearing capacity and the load amplification factor. The third part of the study uses scour fragility curves derived from the proposed equivalent scour load model and a conditional probability approach.

Figure 1 depicts the research process employed in this study. First, a literature review of studies related to bridge scouring was conducted, from which the concept of equivalent scour load was applied to establish a theoretical model. The model was subsequently verified by conducting a static bearing capacity test on a pile foundation, whose the results were then used to modify the theoretical model. Subsequently, a probability simulation was performed using the Monte Carlo method, yielding a mechanical model for equivalent scour load and bearing capacity, which was employed to plot scour fragility curves and develop bridge designs.

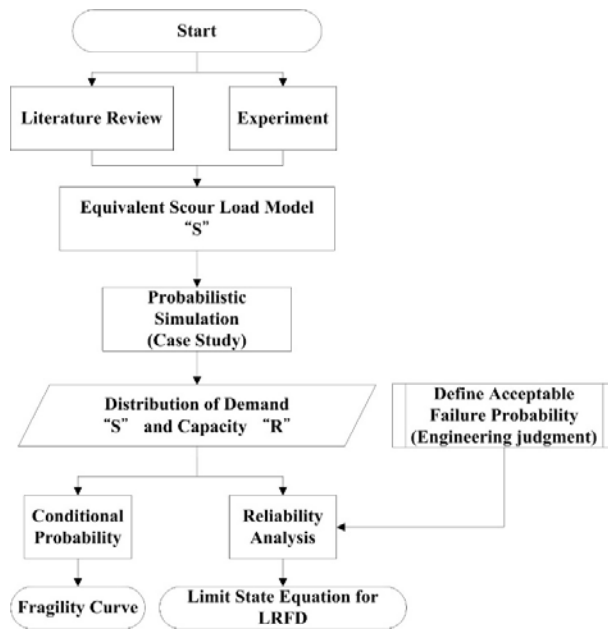


Fig. 1. Research process in this study

Equivalent Static Scour Model

Chen et al. (2014) derived the equivalent scour load model to depict the relationship between resistance reduction and the normalized scour depth. Figure 2 presents the results of the proposed equivalent scour load model. The results of the unadjusted model demonstrate sufficient accuracy at a scour depth ratio (SDR) of <0.3 . Therefore, the model should be modified so that it remains accurate when $SDR > 0.3$ and the effect of the pile diameter is accounted for. Therefore, the assumption pertaining to the soil spring was modified.

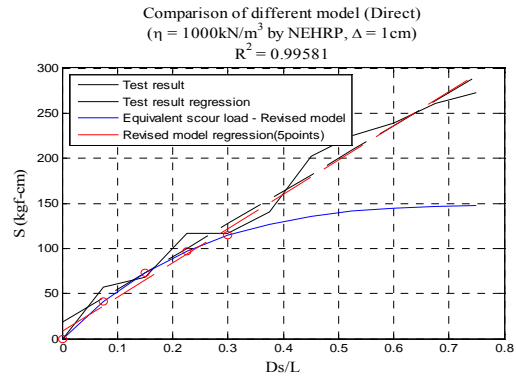


Fig. 2. Comparison of the developed scour load model and test result

The initial linear soil spring was replaced with the nonlinear soil spring proposed by Reese et al. (1997). Subsequently, a soil spring was placed at the center position of each soil layer. This setup was used to simulate the reaction force of the soil.

To verify the assumption of the new soil spring, it was applied to specimens with various scour depths. Subsequently, a pushover experiment was conducted to obtain a curve depicting the effect of lateral force on pile displacement. To calculate the reduction in bearing capacity as scour depth and pile diameter varied, tests were conducted at four embedded depths, with three pile diameters examined at each depth. During testing, a dial indicator was used to measure the lateral displacement at the top of the pile foundation specimen. As shown in Figure 3, the specimen was rotated and pushed manually by using a displacement load-application device, and a load cell was employed to measure the reaction force.

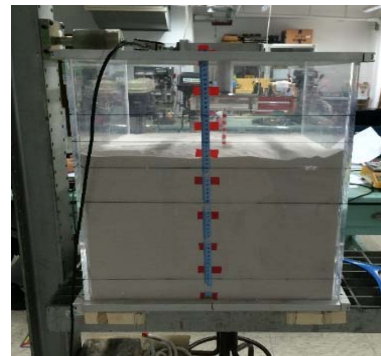


Fig. 3. The photo of the pushover experiment

After obtaining the test results, the applicability of the modified equivalent scour load model can be verified through a comparison of the experimental curve with the analytical curve. The comparison shown in Figure 4 reveals that the two curves are identical, indicating that the assumption of the proposed soil spring is a reliable model of soil behavior. Moreover, relationships between scour depth, pile diameter, and the reduction in bearing capacity were obtained.

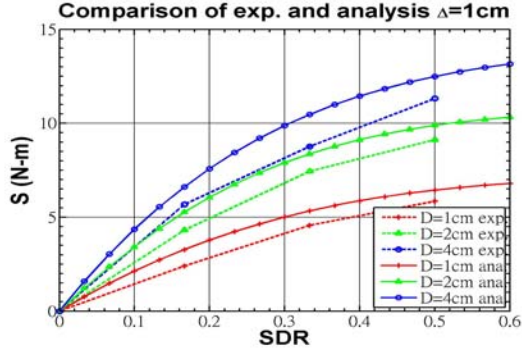


Fig. 4. Comparison of the modified scour load model and test result

Reliability-based bridge design procedure and calculation example

In the following section, the results obtained in this paper are applied to discuss the proposed equivalent scour load model. The modified equivalent scour load model and its corresponding bearing capacity model are presented, and we verify the modified model. According to the verification results, the scouring phenomenon of a downscaled single pile-foundation pier is expressed as an equivalent scour load. Subsequently, the modified equivalent scour load model is applied to plot a scour fragility curve and develop a multiple-hazard load and resistance factor design (LRFD).

Prior to plotting the curve and LRFD, the parameters of the equivalent scour load model were analyzed to determine the distribution and sensitivity of these parameters to various variables. To plot the scour fragility curve, a conditional probability method developed in a previous study was applied using the characteristics of the unmodified equivalent scour load model. This method was employed to deduce the probability of bridge failure. In developing the multiple-hazard LRFD, the load amplification factor and reduction coefficient of the bearing capacity were calculated through a reliability analysis.

For the case of Xibin Bridge, the probability of failure, which must be calculated before the scour fragility curve can be plotted, was determined as an example of using the aforementioned conditional probability method. The results obtained are shown in Figure 5.

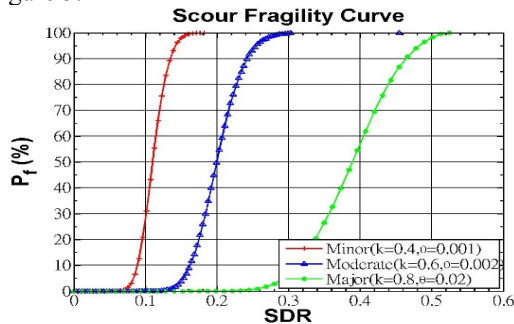


Fig. 5. Evaluated scour fragility curve for Xibin Bridge

In the following section, the equivalent scour load model is applied to multiple-hazard LRFD. A load combination of static, live, and equivalent scour loads was selected for this study. The mode of failure for a crossing bridge is lateral toppling failure, which occurs when the soil has insufficient bearing capacity. The loads can be calculated after the limit state design (LSD) has been defined. Table 1 shows the means, standard deviations, and coefficients of variation of the static, live, and equivalent scour loads on Xibin Bridge.

Table 1. Probability Parameters of Xibin Bridge.

	Mean value(kN-m)	std	c.o.v
Resistance	1.71×10^6	2.34×10^5	0.136
Equivalent Scour Load	8.96×10^5	1.37×10^5	0.154
Dead Load	268.77	21.5	0.08
Live Load	9.44	2.50	0.265

First, the linear function defined in

$$g(x) = R - DL - LL - SC \quad (2)$$

was used to calculate the reliability indicator in

$$\beta = \frac{\mu_R - \mu_{DL} - \mu_{LL} - \mu_{SC}}{\sqrt{\sigma_R^2 + \sigma_{DL}^2 + \sigma_{LL}^2 + \sigma_{SC}^2}}, \quad (3)$$

which was estimated on the basis of the current status of Xibin Bridge, and the failure probability in

$$p_f = 1 - \Phi(\beta) \quad (4)$$

under the four load combinations.

The limit state design method in Equation (1) involves a design problem. Engineers must define a target reliability indicator to obtain the load amplification factor and the reduction coefficients of resistance by using the target reliability indicator to calculate the point of probable failure. Therefore, the direction cosine was calculated using

$$\alpha_i^* = \frac{\alpha_i \sigma_{X_i}}{\sqrt{\sum_i (\alpha_i \sigma_{X_i})^2}}, \quad (5)$$

where α_i^* denotes the direction cosine corresponding to each variable, α_i represents the coefficient in the linear function, and σ_{X_i} is the standard error of each variable (from Table 1). After the direction cosine of each variable was calculated, the load coefficients (*i.e.*, the load amplification factor and reduction coefficient of resistance) were determined using

$$\gamma_i = 1 - \alpha_i^* \beta \Omega_{X_i}, \quad (6)$$

where β represents the target reliability indicator defined by users according to their needs, and Ω_{X_i} is the coefficient of variation corresponding to each

variable. It is defined as the standard error of the mean:

$$\Omega_{x_i} = \frac{\sigma_{x_i}}{\mu_{x_i}} \quad (7)$$

Table 1 lists the parameters. Inputting the parameter values listed in Table 1 into Equation (5), Equation (6), and Equation (7) yielded the load amplification factor and reduction coefficients of resistance, which are required for the multiple-hazard LRFD. Figures 6 and 7 show the results.

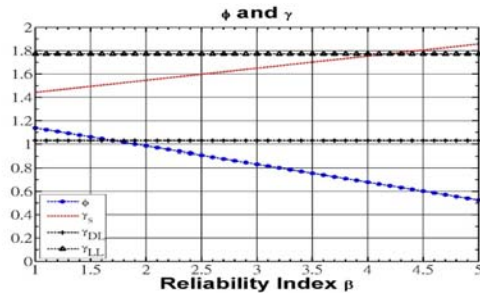


Fig. 6. Evaluated load amplification factor and reduction coefficients of resistance versus reliability index

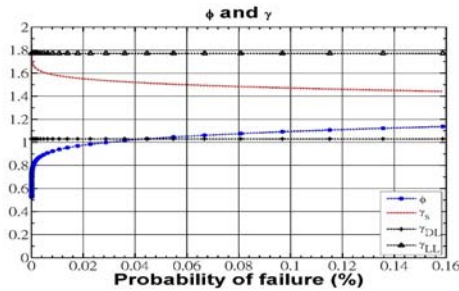


Fig. 7. Evaluated load amplification factor and reduction coefficients of resistance versus probability of failure

By using these two figures, engineers can quickly obtain the load coefficients corresponding to the target reliability indicator or failure probability. Finally, using data published by the United States Department of Transportation, the failure probability for a bridge subjected to scouring is approximately 0.002. Therefore, a target reliability indicator of 3.5 and a corresponding failure probability of 2.35×10^{-4} were selected, and the load coefficient is expressed as

$$0.726R > 1.03DL + 1.77LL + 1.70SC \quad (8)$$

Conclusions

This study adopted the concept of equivalent static load and converted scour depth into an equivalent scour load. A specimen of a downscaled bridge pier with a pile foundation was then used to verify the modified equivalent scour load model. Subsequently, the conditional probability method was employed to plot a scour fragility curve, and a reliability analysis

was conducted to calculate the load coefficients required for use in a multiple-hazard load and resistance factor design.

References

- Zach Liang, and George C. Lee. "Bridge Pier Failure Probabilities under Combined Hazard Effects of Scour, Truck and Earthquake. Part I: Occurrence Probabilities" *Journal of Earthquake Engineering and Engineering Vibration*, Vol. 12, Issue 2. (2013).
- Zach Liang, and George C. Lee. "Bridge Pier Failure Probabilities under Combined Hazard Effects of Scour, Truck and Earthquake. Part II: Failure Probabilities" *Journal of Earthquake Engineering and Engineering Vibration*, Vol. 12, Issue 2. (2013).
- Zach Liang. "Principles and Approaches for Multi-Hazard (MH) LRFD" 7th National Seismic Conference on Bridge and Highways. Keynote Speech, (2013).
- American Association of State Highway and Transportation Officials. "AASHTO LRFD Bridge Design Specifications, Fifth Edition" (2010).
- Andrzej S. Nowak. "Calibration of LRFD Bridge Code" *Journal of Structural Engineering*, Vol. 121, No. 8, (1995).
- Chen, C.-H., "Study on the Methodology for Reliability-based Bridge Design Considering the Equivalent Scour Load" Master Thesis, National Taiwan University (2014).
- Reese, L. C., W. R. COX, and F. D. KOOP, "Analysis of Laterally Loaded Piles in Sand." *Proceeding, Offshore Technology Conference*, Houston, Texas, Vol. II, Paper No.2080, (1974).
- FHWA "Principles of Multiple-Hazard Design for Highway Bridges", (2013).
- J.-F., Teng, T.-J. and Liao, W.-I, (2004). "Numerical Simulation of Near-fault Ground Motions and Induced Structural Responses," *Proceedings of the 13th WCEE (CD-Rom)*, Vancouver, Canada, Paper # 3309.
- Nielsen, S. and Carlson, J. M. (2000), "Rupture pulse characterization: self-healing, self-similar, expanding solutions in a continuum model of fault dynamics", *Bull. Seism. Soc. Am.* 90, 1480-1497.
- Zheng, G. and Rice, J. R. (1998), "Conditions under which velocity-weakening friction allows a self-healing versus a cracklike mode of rupture", *Bull. Seism. Soc. Am.* 88, 1466-1483.

Evaluation of Current Installation Schemes for Viscous Dampers in Taiwan

Wang-Chuen Lin ¹, Shiang-Jung Wang ², Jenn-Shin Hwang ³ and Cho-Yen Yang ⁴

林旺春 ¹、汪向榮 ²、黃震興 ³、楊卓諺 ⁴

Abstract

The installation schemes for viscous dampers implemented into seismic design and retrofit for buildings worldwide have included diagonal-braced, K-braced, and toggle-braced damper systems. In recent practical applications in Taiwan, a few new types of installation schemes other than the aforementioned have been adopted for the purposes of increasing the flexibility of space accommodation and/or architectural lighting consideration to meet the requirements of architects and engineers. Therefore, the purpose of this study is to investigate how the appropriateness of the new installation schemes for viscous dampers affects the energy dissipation design for building structures, such as the flexibility of the connected beams and the additional moment caused by damper force. Moreover, the results from a numerical analysis model, a five-story frame adopting the new installation schemes, show that the schemes cannot reach the desired damping ratio. Finally, this study utilized a Single Degree-of-Freedom (SDOF) system model composed of the damper and connected beams in series, and the analysis results explore that the new installation schemes should implement greater numbers of dampers with lower force capacity for each so as to reduce the flexibility effect of the connected beams. Thus, the designed dampers can provide sufficient damping ratio as expected.

Keywords: installation scheme, viscous damper, energy dissipation design, viscous damping coefficient

Introduction

The design specifications for viscous dampers implemented into buildings, such as FEMA 274 (1997), have provided design formulas to calculate the supplemental damping ratio by dampers. Based on the first vibration mode of structure, the design formulas are derived for linear and nonlinear viscous dampers as below, respectively (Hwang et al., 2008).

$$\xi_d = \frac{T \sum_j C_j f_j^2 \phi_j^2}{4\pi \sum_i m_i \phi_i^2} \quad (\text{linear damper}) \quad (1)$$

$$\xi_d = \frac{T^{2-\alpha} \sum_j \lambda_j C_j f_j^{1+\alpha} \phi_j^{1+\alpha}}{(2\pi)^{3-\alpha} A^{1-\alpha} \sum_i m_i \phi_i^2} \quad (\text{nonlinear damper}) \quad (2)$$

where C_j = the damping coefficient of the damper at the j^{th} story; f_j = the magnification factor depending on the installation scheme of dampers; ϕ_i = the horizontal modal displacement of the i^{th} story; ϕ_{rj} = the first modal relative displacement between the ends of the damper j in the horizontal direction; m_i = the mass of the i^{th} story; T = the natural period of the first vibration mode; α = the damping exponent which is often prescribed by designers; A = the roof response amplitude corresponding to the modal displacement ϕ_j normalized to a unit value at the roof; and λ = the parameter listed in FEMA 274. The installation schemes for viscous dampers implemented into seismic design and retrofit for

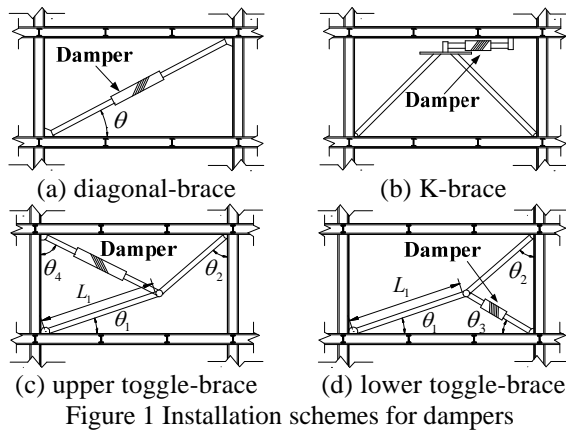
¹ Assistant Researcher, National Center for Research on Earthquake Engineering, wclin@narlabs.org.tw

² Research Fellow, National Center for Research on Earthquake Engineering, sjwang@narlabs.org.tw

³ Division Director, National Center for Research on Earthquake Engineering, jshwang@narlabs.org.tw

⁴ Assistant Researcher, National Center for Research on Earthquake Engineering, cyyang@narlabs.org.tw

buildings worldwide have included diagonal-braced, K-braced, and toggle-braced damper systems, as shown in Figure 1.



However, in recent practical applications in Taiwan, several new types of installation schemes other than the aforementioned, including steel frame, wall frame, RC support, and A-type steel frame systems shown in Figure 2, have been adopted for the purposes of increasing the flexibility of space accommodation and/or architectural lighting consideration to meet the requirements of architects and engineers. Figure 3 presents the practical cases of the steel and wall frame installation schemes for viscous dampers in high-rise buildings. This study aims to numerically discuss the advantages and drawbacks of the new installation schemes in terms of design and installation.

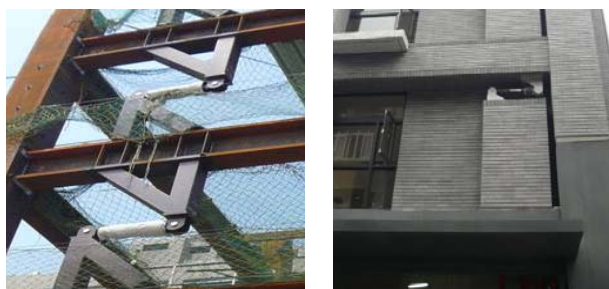
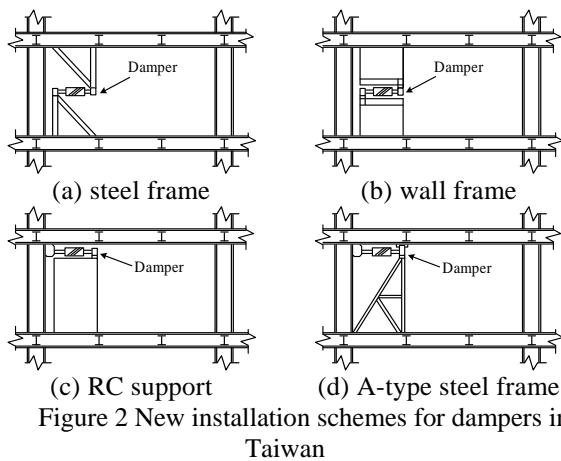


Figure 3 Cases of new installation schemes for dampers in Taiwan

Discussion on new installation schemes for dampers

Taking the wall frame installation scheme shown in Figure 4 as an example, obviously, this scheme will result in an additional moment exerted on the beams connected with the viscous damper during an earthquake. The flexibility of the connected beams will undoubtedly reduce the axial deformation of the damper and thus affect its desired seismic-resistant performance.

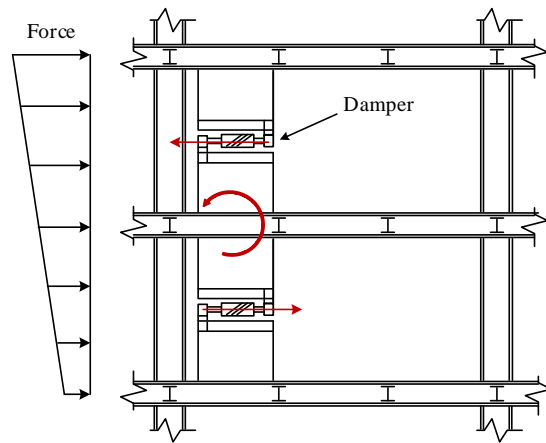


Figure 4 Additional moment caused by damper force

To further illustrate this point, a five-story frame is designed as per the seismic design code for buildings in Taiwan and the steel frame installation scheme for linear viscous dampers is adopted, as shown in Figure 5. It is assumed that the effective damping ratio of the damped structure is designed to be 12%, including 2% inherent damping ratio and 10% contributed by the dampers. Obtained from the modal analysis result, the first modal period (T) in X direction is 0.586 sec. The sectional dimensions of the columns, beams, and braces are summarized in Table 1. The story mass and the first modal shape are listed in Table 2. Assuming that the damping coefficients assigned to all stories are identical (i.e. uniform distribution), the linear damping coefficient at each story is calculated to be 144.75 ton-sec/m.

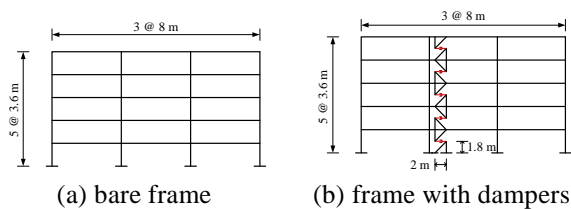


Figure 5 Five-story frame

Table 1 Sectional dimensions of the five-story frame

	Beam	Column	Brace
1F~5F	H450×300×12×22	H800×400×16×38	H300×300×12×22

Table 2 Story mass and first modal shape of the five-story frame

Story	Mass (ton-sec ² /m)	ϕ_i
5	6.606	1
4	6.606	0.8214
3	6.606	0.5954
2	6.606	0.3438
1	6.606	0.1167

Excited by a sinusoidal acceleration pulse (see Figure 6) and taking logarithm decay of the free vibration response history (see Figure 7), the damping ratio of the damped structure can be identified by using the formula as below:

$$\xi = \frac{Q}{2n\pi\sqrt{1+\left(\frac{Q}{2n\pi}\right)^2}} \quad (3)$$

where $Q = \ln(u_m/u_{m+n})$.

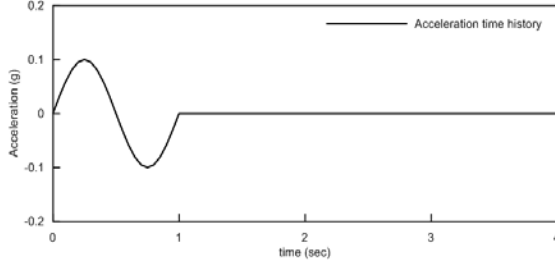


Figure 6 Sinusoidal acceleration pulse

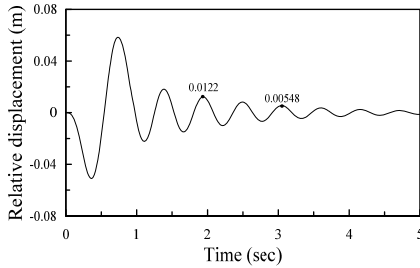


Figure 7 Free vibration displacement response history

Therefore, for this design case, the identified damping ratio is about 6.37%.

$$Q = \ln \frac{0.0122}{0.00548} = 0.803$$

$$\xi_{eff} = \frac{0.803}{2 \times 2 \times \pi \sqrt{1 + \left(\frac{0.803}{2 \times 2 \times \pi}\right)^2}} \times 100\% = 6.37\% \quad (4)$$

The identified damping ratio is much smaller than the expected damping ratio 12%. The numerical result indicates that the new installation schemes cannot guarantee the desired damping ratio to the damped structure due to the flexibility effect of the connected beams. In other words, if adopting the new installation schemes, the actual damping ratio cannot completely reach the design damping ratio calculated by using Equation (1) or (2).

SDOF system model based on damper and beam in series

In this study, a Single Degree-of-Freedom (SDOF) system, i.e. the equivalent system A shown in Figure 8(b), is utilized to equivalently represent the linear damper and the connected beams in series (see Figure 8(a)) (Xiao, 2007) (Guo, 2008). In Figure 8, K_f is the storage stiffness of the beams in phase to displacement; K_d'' is the loss stiffness of the linear damper and it has a phase lag of 90° to displacement; K_a' and K_a'' are the storage stiffness and loss stiffness of the equivalent system A, respectively. $u_b, u_d, u_a, F_b, F_d,$ and F_a are the deformation and force of the beams, damper, and equivalent system A, respectively. Assuming that a sinusoidal motion is capable of representing the deformation of the equivalent system A, the deformation and force in series are given as below:

$$u_b(t) + u_d(t) = u_a(t) = u_{a\max} \sin \omega t \quad (5)$$

$$F_b(t) = F_d(t) = F_a(t) = K_a' u_{a\max} \sin \omega t + K_a'' u_{a\max} \cos \omega t \quad (6)$$

where $u_{a\max}$ is the amplitude of the equivalent system A; ω is the vibration frequency.

$$F_b(t) = K_f u_b(t) \quad (7)$$

$$F_d(t) = K_d'' u_d(t + \frac{\pi}{2\omega}) \quad (8)$$

Based on Equations (7) and (8), u_b and u_d can be represented as below:

$$u_b(t) = \frac{F_b(t)}{K_f} \quad (9)$$

$$u_d(t) = \frac{F_d(t - \frac{\pi}{2\omega})}{K_d''} \quad (10)$$

Substituting Equations (9) and (10) into Equation (5), the storage stiffness (K_a') and loss stiffness (K_a'') of the equivalent system A can be represented by K_f and K_d'' as below:

$$K_a' = \frac{K_f K_d''^2}{K_f^2 + K_d''^2} \quad (11)$$

$$K_a'' = \frac{K_f^2 K_d''}{K_f^2 + K_d''^2} \quad (12)$$

The energy dissipated by the damper per cycle, W_D , is

$$W_D = \oint F_d du = \oint K_d'' u_{\max} \cos(\omega t) d(u_{\max} \sin \omega t) = \pi K_d'' u_{\max}^2 \quad (13)$$

Based on the relationship between the energy dissipated by the damper (W_D) and the effective damping coefficient (C_d), the greater the beam stiffness is, the larger value of energy dissipated by

the damper raises, as shown in Figure 9. With the new installation schemes, the limitlessly added on effective damping coefficients will increase the damper force, also resulting in the enhancement of deformation of the connected beams. It makes the dampers in the new schemes fail to demonstrate the desired energy dissipation ability. Therefore, it is suggested that stiffening the connected beams and adopting greater numbers of dampers with lower force capacity for each can reduce the flexibility effect of the connected beams so that the designed dampers can provide sufficient damping ratio.

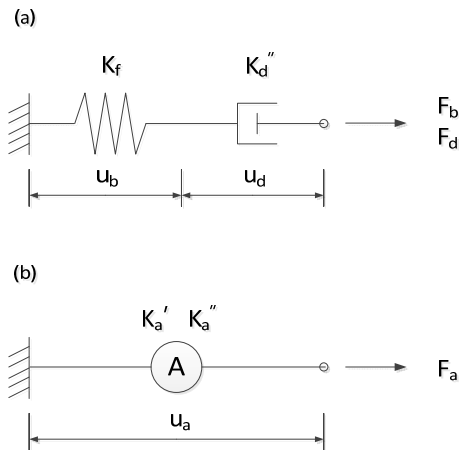


Figure 8 SDOF system model; (a) linear damper and beam in series; (b) equivalent system A

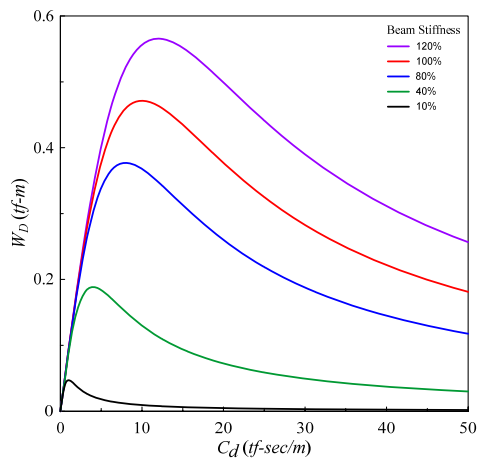


Figure 9 Relationships between energy dissipated by damper (W_D) and effective damping coefficients (C_d)

Conclusions

This study has illustrated that the new installation schemes for viscous dampers make the connected beams subjected to an additional moment under an earthquake, thus reducing the energy dissipation ability. The flexibility of the connected beams gives rise to the fact that the actual damping ratio to the structure is lower than the expected one. Moreover, the relations between the energy dissipation (W_D) and effective damping coefficient (C_d) by derivation from the SDOF system model composed of the damper and

connected beams in series revealed that although the effective damping ratio can be elevated by increasing damping coefficients, less energy dissipation ability is demonstrated due to the more significant deformation of the connected beams by increased damper force. Therefore, in order to achieve the expected seismic-resistant performance provided by dampers in the new installation schemes, this study suggests stiffening the connected beams and adopting greater numbers of dampers with lower force capacity for each to reduce the flexibility effect of the connected beams.

References

- FEMA, NEHRP Guidelines and Commentary for the Seismic Rehabilitation of Building, Reports No.273 and 274, October, Washington, D.C., 1997.
- Hwang, J.S., Huang, Y.N., Yi, S.L. and Ho, S.Y., "Design Formulations for Supplemental Viscous Dampers to Building Structures," Journal of Structural Engineering, ASCE, (special issue on design and analysis of structures with damping systems), Vol. 134, No.1, pp. 22-31, 2008.
- Xiao Y. N. (2007). A Design Method for Viscous Dampers Considering Flexibility of Connecting Braces (Master's thesis). National Taiwan University of Science and Technology, Taipei, Taiwan, ROC.
- Guo, Y. Z. (2008). Design of Viscous Dampers Considering Flexibility of Connecting Braces (II) (Master's thesis). National Taiwan University of Science and Technology, Taipei, Taiwan, ROC.

Experimental and Analytical Study on Multiaxial Hysteresis Behavior of High-Damping Rubber Bearings

Wang-Chuen Lin ¹, Shiang-Jung Wang ², Jenn-Shin Hwang ³ and Cho-Yen Yang ⁴

林旺春¹、汪向榮²、黃震興³、楊卓諺⁴

Abstract

High-damping rubber (HDR) bearings have gradually become a commonly used type of seismic isolators worldwide. Because of the complex material compound, their actual hysteresis behavior is highly nonlinear and may not be very well represented by the existing bilinear approximation. In this study, first, a modified mathematical model is proposed for comprehensively characterizing the unilateral hysteresis behavior of HDR bearings under sinusoidal and triangular reversal loading. In addition to unilateral reversal loading tests, HDR bearings are tested with different non-proportional plane loading patterns, including circular and figure-eight orbits. It is found that under bilateral reversal loading, the torsional coupling effect is significant on the mechanical properties and hysteresis behavior of HDR bearings. Therefore, integrating the three-dimensional constitutive law and the plane vector concept with the modified unilateral model, a further extended mathematical model for HDR bearings under non-proportional plane loading is developed. The accuracy and applicability of the modified and further extended mathematical models are verified through comparison with the test results.

Keywords: high-damping rubber bearing; multiaxial hysteresis behavior; non-proportional plane loading; mathematical model; torsional coupling effect

Introduction

Although the bilinear approximation may not very well represent the highly nonlinear hysteresis behavior of HDR bearings, it is still commonly adopted in current practical isolation design as long as the design result can be guaranteed on safe side. A few sophisticated models which are capable of more accurately characterizing the hysteresis behavior of HDR bearings have been provided in past researches. However, their complexity more or less impedes the implementation into most commercial computation tools. A simple mathematical model accounting for the unilateral shear force experienced by HDR bearings as a combination of restoring force and damping force was proposed and experimentally verified by Hwang et al. (2002). To further predict the multi-axial hysteresis behavior of laminated rubber bearings, Abe et al. (2004a, 2004b) derived a

two-dimensional model on the basis of the Özdemir model (1973) and the three-dimensional constitutive law. It was also experimentally demonstrated that the hysteresis behavior of HDR bearings under bilateral loading can be well simulated by the model.

In this study, a scaled-down HDR bearing is tested with different loading patterns, including unilateral reversal loading and non-proportional plane loading. Accordingly, two mathematical models modified from Hwang's and Abe's analytical models respectively accounting for the hysteresis behavior of HDR bearings under unilateral and bilateral loading are developed. The accuracy and applicability of the two modified models are verified through comparison with a series of test results. In addition, the torsional coupling effect on the mechanical properties and hysteresis behavior of HDR bearings is experimentally discussed.

¹ Assistant Researcher, National Center for Research on Earthquake Engineering, wclin@narlabs.org.tw

² Research Fellow, National Center for Research on Earthquake Engineering, sjwang@narlabs.org.tw

³ Division Director, National Center for Research on Earthquake Engineering, jshwang@narlabs.org.tw

⁴ Assistant Researcher, National Center for Research on Earthquake Engineering, cyyang@narlabs.org.tw

Mathematical Model by Hwang et al.

In the mathematical model proposed by Hwang et al. (2002), the shear force experienced by an elastomeric bearing was characterized in the form of

$$F(x(t), \dot{x}(t)) = K(x(t), \dot{x}(t))x(t) + C(x(t), \dot{x}(t))\dot{x}(t) \quad (1)$$

where $x(t)$ and $\dot{x}(t)$ are the relative displacement and relative velocity of the elastomeric bearing at time t , respectively. The stiffness and damping coefficient at time t are respectively given by

$$K(x(t), \dot{x}(t)) = a_1 + a_2 x^2(t) + a_3 x^4(t) + \frac{a_4 \exp\left[a_9 \int_0^t F(x(t), \dot{x}(t)) dx(t)\right]}{\cosh^2(a_5 \dot{x}(t))} \quad (2)$$

$$C(x(t), \dot{x}(t)) = \frac{a_6 + a_7 \dot{x}^2(t)}{\sqrt{a_8^2 + \dot{x}^2(t)}} \left\{ 1 + \exp\left[a_{10} \int_0^t F(x(t), \dot{x}(t)) dx(t)\right] \right\} \quad (3)$$

where $a_1 \sim a_{10}$ are to-be-determined coefficients from cyclic loading or dynamic tests by using the nonlinear-least squares method or downhill simplex method. The cyclic softening behavior of an elastomeric bearing can be regarded as a function of energy dissipation. Thus, the integral term $\int_0^t F(x(t), \dot{x}(t)) dx(t)$ together with the to-be-determined coefficients are applied in Equations (2) and (3) to respectively describe the degradation of stiffness and the variation of hysteresis loop area.

Multi-axial Loading Testing

A scaled-down HDR bearing is schemed to be tested under unilateral reversal loading and non-proportional plane loading. The diameter of the HDR bearing specimen is 150mm. It comprises 25 layers of rubber with a thickness of 1.97mm for each as well as 24 layers of steel shim with a thickness of 1.2mm for each. The test setup is illustrated in Figure 1. As observed from Figure 1, the vertical load on the bearing is exerted by an oil jack, while the lateral displacement is executed by two mutually orthogonal servo-control actuators connected with the moveable platen. A linear guide system is installed underneath the platen to reduce the friction force induced by the test system. An external load cell is installed to measure the actual force responses of the bearing during tests. The unilateral test protocols under triangular and sinusoidal reversal loading are respectively detailed in Tables 1 and 2, and the bilateral ones under non-proportional plane loading, including circular and figure-eight orbits, are detailed in Table 3. The equations of the plane loading paths shown in Figure 2 are given by

Circular orbit:

$$U_x = U_0 \sin \omega t \quad (4)$$

$$U_y = U_0 \cos \omega t \quad (5)$$

Figure-eight orbit:

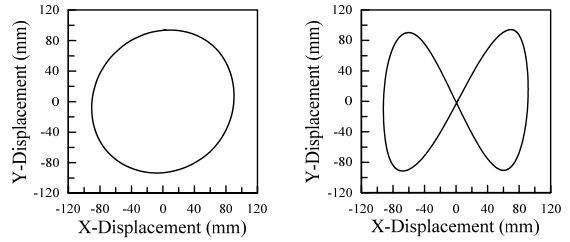
$$U_x = U_0 \sin \omega t \quad (6)$$

$$U_y = U_0 \sin 2\omega t \quad (7)$$

where U_x and U_y are the displacement components in two principal horizontal directions, i.e. X and Y directions, respectively; U_0 is the displacement amplitude; ω is the angular frequency.



Figure 1 Test installation



(a) circular orbit (b) figure-eight orbit

Figure 2 Plane loading paths

Table 1 Unilateral test protocols under triangular reversal loading

Vertical Stress (kg/cm ²)	Horizontal Shear Strain (%)	Horizontal Disp. Amplitude (mm)	Horizontal Vel. (mm/sec)	Cycles
50	50	24.63	24.63 49.26 73.89	3
	100	49.25		
	150	73.88		
	200	98.50		
	250	123.13		

Table 2 Unilateral test protocols under sinusoidal reversal loading

Vertical Stress (kg/cm ²)	Horizontal Shear Strain (%)	Horizontal Disp. Amplitude (mm)	Freq. (Hz)	Cycles
50	50	24.63	0.125 0.25	3
	100	49.25		
	150	73.88		
	200	98.50		
	250	123.13		

Table 3 Bilateral test protocols under non-proportional plane loading

Orbit	Vertical Stress (kg/cm ²)	Horizontal Shear Strain (%)	Horizontal Disp. Amplitude (mm)	Freq. (Hz)	Cycles
Circular	50	50	24.63	0.0125	3
		100	49.25	0.05	
		150	73.88	0.1	
		200	98.50	0.2	
Figure-eight	50	50	24.63	0.0125	3
		100	49.25	0.05	
		150	73.88	0.1	
		200	98.50	0.2	

Modified Mathematical Model under Unilateral Reversal Loading

The comparison of unilateral test results and predictions by Hwang's analytical modal is shown in

Figure 3. As observed from Figure 3(a), the prediction for the hysteresis behavior of HDR bearings under sinusoidal reversal loading has a good agreement with the test result. However, the prediction result is not acceptable when subjected to triangular reversal loading. It is because that not only the relative displacement $x(t)$ but the relative velocity $\dot{x}(t)$ also is the variable of the mathematical model given in Equations (2) and (3). Under triangular reversal loading, the relative velocity history will become a typical step function, leading to a sudden force change at the transition of velocity directions. It implies that Hwang's analytical modal might be only appropriate for characterizing the unilateral hysteresis behavior of HDR bearing under harmonic loading.

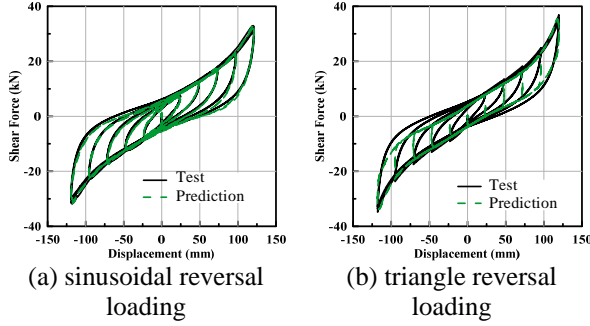


Figure 3 Experimental and predicted hysteresis behavior under different unilateral loading patterns (Hwang's modal)

The analytical models developed by both Hwang et al. and Abe et al. feature the hysteresis behavior of HDR bearings as a combination of restoring force and damping force. Therefore, referring to Hwang's and Abe's analytical models, a modified mathematical model for comprehensively characterizing the unilateral hysteresis behavior of HDR bearings is proposed herein.

$$F(x(t), \dot{x}(t)) = F_1(t) + F_2(t) \quad (8)$$

$$F_1(t) = [a_1 + a_2 x^2(t) + a_3 x^4(t)] \dot{x}(t) \quad (9)$$

$$\dot{F}_2(t) = [a_4 + a_5 x^2(t)] \left[\dot{x}(t) - |\dot{x}(t)| \left| \frac{F_2(t)}{Y_t} \right|^{a_6} \text{sgn}\left(-\frac{F_2(t)}{Y_t}\right) \right] \quad (10)$$

$$Y_t = a_7 + \left[1 + \left| \frac{x(t)}{a_8} \right|^{a_9} \right] \quad (11)$$

where $F_2(t)$ is the restoring force of the elastoplastic spring which is adopted to simulate the hysteresis behavior; Y_t represents the variation of hysteresis loop area; $a_1 \sim a_9$ are to-be-determined coefficients from cyclic loading or dynamic tests.

Through comparison with the test results shown in Figure 4, the modified mathematical model indeed can well capture the unilateral hysteresis behavior of HDR bearings under both sinusoidal and triangular reversal loading.

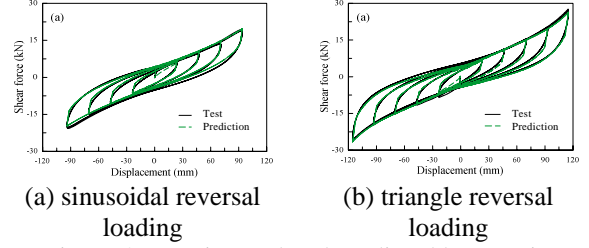


Figure 4 Experimental and predicted hysteresis behavior under different unilateral loading patterns (modified model)

Non-proportional Plane Loading Test Results and Further Extended Mathematical Model

Based on experimental observation, Yamamoto et al. (2012) indicated that the torsional coupling effect plays a crucial role in the bilateral hysteresis behavior of HDR bearings. As observed from the comparison of X directional hysteresis loops under unilateral reversal loading and non-proportional plane loading shown in Figure 5, there exists a significant difference because of the torsional coupling effect, which results in the local shear strain increased. Besides, it is apparent that different plane loading patterns cause diverse torsional coupling extents.

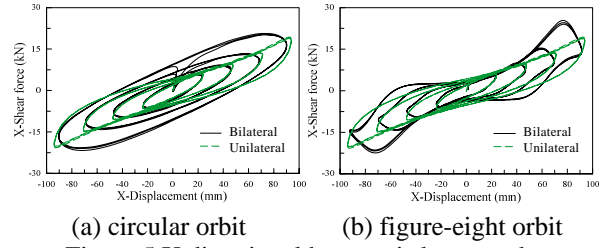


Figure 5 X directional hysteresis loops under unilateral and bilateral loading

The comparison of X directional effective shear modulus and equivalent damping ratio under unilateral reversal loading and non-proportional plane loading with the same shear strain level is shown in Figure 6. It is found that the calculated effective shear modulus under unilateral loading is the largest, while that under figure-eight orbit loading is the smallest. In addition, the calculated equivalent damping ratio under circular orbit loading is the largest, while that under unilateral loading is the smallest.

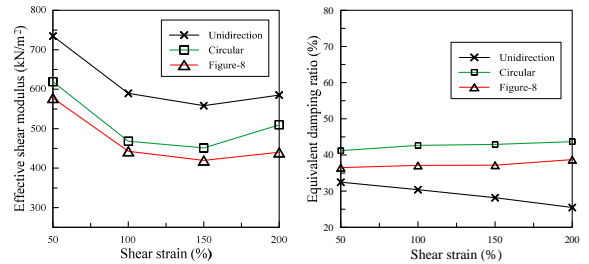


Figure 6 X directional properties under unilateral and bilateral loading

Referring to the modified model, a further extended mathematical model for characterizing the bilateral hysteresis behavior of HDR bearings is

proposed herein.

$$\bar{F} = \begin{Bmatrix} F_x \\ F_y \end{Bmatrix} = \bar{F}_1 + \bar{F}_2 \quad (12)$$

where F_x and F_y are the force components in two principal horizontal directions, i.e. X and Y directions, respectively.

Based on the plane vector concept, the relative displacement, relative velocity, and shear force in two principal horizontal directions, X and Y directions, can be expressed in the form of vectors herein.

$$\bar{U} = \{U_x \quad U_y\}^T, |\bar{U}| = \sqrt{U_x^2 + U_y^2} \quad (13)$$

$$\bar{\dot{U}} = \{\dot{U}_x \quad \dot{U}_y\}^T, |\bar{\dot{U}}| = \sqrt{\dot{U}_x^2 + \dot{U}_y^2} \quad (14)$$

$$\bar{F} = \{F_x \quad F_y\}^T, |\bar{F}| = \sqrt{F_x^2 + F_y^2} \quad (15)$$

Similarly, Equation (9) to Equation (11) can be respectively expressed as

$$\bar{F}_1 = \begin{Bmatrix} F_{1x} \\ F_{1y} \end{Bmatrix} = K\bar{U}(t) = a_1\bar{U}(t) + a_2\bar{U}^3(t) + a_3\bar{U}^5(t) \quad (16)$$

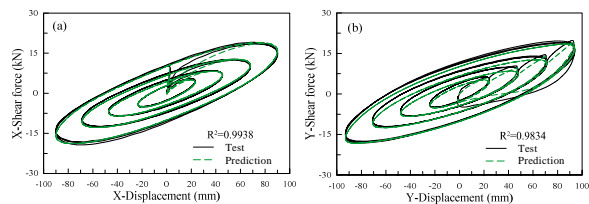
$$\bar{F}_2 = [a_4 + a_5\bar{U}^2(t)] \left[\bar{\dot{U}}(t) - \left| \frac{\bar{F}_2}{Y_i} \right|^{a_6-1} \right] \frac{\bar{F}_2}{Y_i} \quad (17)$$

$$Y_i = a_7 + \left[1 + \left| \frac{\bar{\dot{U}}(t)}{a_8} \right|^{a_9} \right] \quad (15)$$

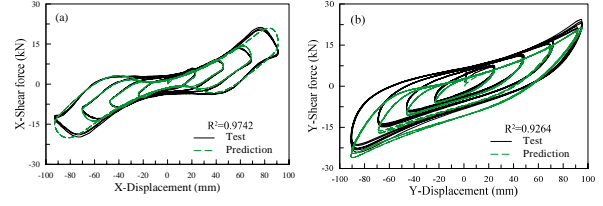
Through mathematically fitting the bilateral test result under one of the test conditions, circular orbit loading with a horizontal shear strain of 200% and a frequency of 0.0125Hz, a set of $a_1 \sim a_9$ in the further extended mathematical model can be identified and are listed in Table 4. To demonstrate the robustness of the extended model, these determined coefficients are also applied to predict the bilateral hysteresis behavior of HDR bearings under another test condition listed in Table 3. The comparison of the prediction with the test result under circular and figure-eight orbit loading with the same shear strain but a different frequency, 0.1Hz, is shown in Figure 7. The coefficient of determination R^2 is adopted to quantitatively evaluate the difference between the predictions and test results. Apparently, the nine coefficients identified from one test result are also capable of well predicting the bilateral hysteresis behavior of HDR bearings under other test conditions.

Table 4 Identified nine coefficients
(circular orbit, 200%, 0.0125Hz)

a_1	a_2	a_3	a_4	a_5	a_6	a_7	a_8	a_9
0.12796	-2.5E-6	0.426	0.3477	1.31	1.31921	3.05825	61.3706	2.44623



(a) circular orbit (test: 0.1Hz; prediction: 0.0125Hz)



(b) figure-eight orbit (test: 0.1Hz; prediction: 0.0125Hz)
Figure 7 Experimental and predicted hysteresis behavior under different bilateral loading patterns (further extended model)

Conclusions

In this study, a series of unilateral and bilateral tests are conducted on a scaled-down HDR bearing. Referring to Hwang's and Abe's analytical models, a modified mathematical model which can comprehensively account for the unilateral hysteresis behavior of HDR bearings under sinusoidal and triangular reversal loading is proposed. Besides, a further extended mathematical model is developed for characterizing the bilateral hysteresis behavior of HDR bearings. By comparing the predictions with the test results under circular and figure-eight orbit loading with different excitation frequency (or velocity) conditions, it can be concluded that the proposed extended mathematical model can well capture the bilateral hysteresis behavior of HDR bearings. The test results also reveal that since the torsional coupling effect results in the local shear strain increased, the effective shear modulus and equivalent damping ratio under non-proportional plane loading become smaller and larger, respectively, compared with those under unilateral reversal loading. It should be carefully taken into account during the design process.

References

- Abe M, Yoshida J, Fujino Y. Multiaxial behaviors of laminated rubber bearings and their modeling. I: experimental study. *Journal of Structural Engineering* 2004; 130(8): 1119-1132.
- Abe M, Yoshida J, Fujino Y. Multiaxial behaviors of laminated rubber bearings and their modeling. II: modeling. *Journal of Structural Engineering* 2004; 130(8): 1133-1144.
- Hwang JS, Wu JD, Pan TC, Yang G. A mathematical hysteretic model for elastomeric isolation bearing. *Earthquake Engineering and Structural Dynamics* 2002; 31(4): 771-789.
- Özdemir, H. Nonlinear transient dynamic analysis of yielding structures. PhD Dissertation 1973, University of California, Berkeley, Berkeley, Calif.
- Yamamoto M, Minewaki S, Yoneda H, Higashino M. Nonlinear behavior of high-damping rubber bearings under horizontal bidirectional loading: full-scale tests and analytical modeling. *Earthquake Engineering and Structural Dynamics* 2012; 41: 1845-1860.

Experimental Study on Building Mass Damper Using Optimum Dynamic Response Control Algorithm

Bo-Han LEE¹, Shiang-Jung WANG², Jenn-Shin HWANG³ and Kou-Chun CHANG⁴

李柏翰¹、汪向榮²、黃震興³、張國鎮⁴

Abstract

To overcome the concern of limited response reduction due to insufficient tuned mass in the conventional tuned mass damper (TMD) design, the design method and seismic performance of the building mass damper (BMD) system are analytically and numerically discussed in this preliminary study. In this research, a simplified three-lumped-mass structural model, simulating superstructure, control layer and substructure, represents a building with the BMD system. The objective function for the BMD design is determined by the dynamic response control of both the substructure and superstructure. Considering appropriate system parameters, the optimum parameters for the BMD system are derived.

Then by applying the shaking table test, a series of shaking table tests will be performed to verify the feasibility of the BMD concept and the effectiveness of the optimum BMD design on seismic protection of buildings. Based on the research results, the BMD design method can reduce responses of both superstructure and superstructure effectively.

Keywords: Mid-story isolation system, Tuned mass damper, Building mass damper, Objective function, Numerical analysis, Shaking table test.

Introduction

The optimum design method for the building mass damper (BMD) system is proposed in this research application. The mass of the superstructure is taken into account to derive the design parameters from the motion equation. To develop the interaction between primary structure and building mass absorber, they are controlled to move out of phase. The optimum building mass damper (OBMD) system design method is proposed and a series of numerical and experimental analyses are performed to verify the feasibility of the BMD concept.

Analytical Study

A simplified three-lumped-mass structure model, as shown in Fig.1, in which three lumped mass are respectively assigned at the building mass absorber, the control layer and the primary structure is rationally assumed to represent a building structure with a BMD

system. For doing so is that inherent dynamic characteristics (fundamental modal characteristics of vibration) of both the building mass absorber and primary structure can be considered comprehensively in the simplified structure model. The motion equation of the simplified structure model can also be expressed in terms of the nominal frequency ω_1 , frequency (or tuning) ratio f_i ($i = 2, 3$), mass ratio μ_i ($i = 2, 3$) and component damping ratio ζ_i ($i = 1\sim 3$) as defined in the following

$$f_i = \frac{\omega_i}{\omega_1}, i = 2, 3 \quad (1)$$

$$\mu_i = \frac{m_i}{m_1}, i = 2, 3 \quad (2)$$

$$\zeta_i = \frac{c_i}{2 \sum_{j=1}^3 m_j \omega_j}, i = 1\sim 3 \quad (3)$$

¹ Assistant Research Fellow, National Center for Research on Earthquake Engineering

² Research Fellow, National Center for Research on Earthquake Engineering

³ Professor, College of Civil Engineering, National Taiwan University of Technology

⁴ Professor, College of Civil Engineering, National Taiwan University

where $i = 1, 2$ and 3 denote the primary structure, control layer and building mass absorber, respectively; and the nominal frequencies ω_1 , ω_2 and ω_3 are defined as $\sqrt{k_1/m_1}$, $\sqrt{k_2/(m_2 + m_3)}$ and $\sqrt{k_3/m_3}$, respectively. When the support excitation is harmonic and its acceleration amplitude is fixed and independent of frequency, i.e. $u_g = Ge^{i\omega t}$. The equation of motion for the whole system can be expressed as

$$e^{i\omega t} \begin{bmatrix} -m_1\omega^2 + k_1 + k_2 + i\omega(c_1 + c_2) & -k_2 - i\omega c_2 & 0 \\ -m_2\omega^2 + k_2 + k_3 + i\omega(c_2 + c_3) & -k_3 - i\omega c_3 & 0 \\ \text{sym.} & -m_1\omega^2 + k_1 + i\omega c_1 & 0 \end{bmatrix} \begin{bmatrix} u_1 \\ u_2 \\ u_3 \end{bmatrix} = -Ge^{i\omega t} \begin{bmatrix} m_1 \\ m_2 \\ m_1 \end{bmatrix} \quad (4)$$

the ratio of the vibration amplitude to the input amplitude can be solved from equation (4)

$$\begin{aligned} \frac{\omega_1^2 |u_1|}{G} &= \frac{|b_1(a_3 a_5 - a_4^2) - b_2 a_2 a_5 + b_3 a_2 a_4|}{|a_1 a_3 a_5 - a_2^2 a_5 - a_1 a_4^2|} \\ \frac{\omega_1^2 |u_2|}{G} &= \frac{|-b_1 a_2 a_5 + b_2 a_1 a_5 - b_3 a_1 a_4|}{|a_1 a_3 a_5 - a_2^2 a_5 - a_1 a_4^2|} \\ \frac{\omega_1^2 |u_3|}{G} &= \frac{|b_1 a_2 a_4 - b_2 a_1 a_4 + b_3 (a_1 a_3 - a_2^2)|}{|a_1 a_3 a_5 - a_2^2 a_5 - a_1 a_4^2|} \end{aligned} \quad (5)$$

Considering the response of each degree of freedom could not exceed the input amplitude, set the sum of response in three degrees of freedom to be the objective function.

$$\text{Objective function} = \text{Min.} \left(\frac{\omega_1^2 |u_1|}{G} + \frac{\omega_1^2 |u_2|}{G} + \frac{\omega_1^2 |u_3|}{G} \right) \quad (6)$$

Based on the objective function with the necessary parameters ω_1 , μ_2 , μ_3 , ξ_1 and ξ_2 , the optimum design parameters for ξ_2 , f_2 and f_3 can be determined.

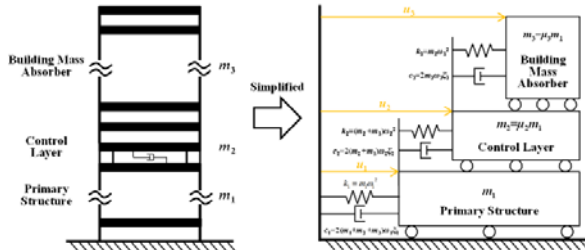


Fig. 1 Simplified three-lumped-mass structure model

Experimental Study

Experimental structure model

The experimental model is designed to be a 8-story steel structure of 1.5m in the X direction and of 1.1m in the Y direction, as shown in Figure 2(a). The height of each story is 1.1m. The sections of columns and beams are wide flanges with a dimension of 100×100×6×8 and 100×50×5×5 (mm), respectively. All the members are made of A36 steel. A mass blocks with uniform load of 500 kgf/m² is assigned at each floor.

After a series of numerical analyses are performed, the model which upper four-story and lower three-story structures and primary structure with an inherent damping ratio of 2% (B3C2) has a good

potential in reducing the acceleration of superstructure and displacement responses of building structures subjected to seismic loading. Therefore, the model B3C2 is selected to be the optimum building mass damper system (OBMD), as shown in Figure 2(b).

The control layer of OBMD system between the building mass absorber and primary structure is designed to be composed of four natural rubber bearings (RBs) installed at each column, as shown in Fig. 3. Calculating the masses and natural frequencies of the fundamental modes of the building mass absorber and primary structure, the optimum BMD design parameters for the control layer and building mass absorber can be obtained (i.e. $\xi_2^{opt} = 17\%$, $f_2^{opt} = 0.95$ and $f_3^{opt} = 1.6$). Either stiffening the primary structure or softening the building mass absorber can be considered to achieve the calculated demand of f_3^{opt} . In this experimental study, the building mass absorber is stiffened with angle braces a dimension of 15×15×2.



(a) Specimen BF (b) Specimen B3C2

Fig. 2 Elevation of each specimen



Fig. 3 Isolayer detail

Analytical program

Five real earthquake records denoted as EL Centro, Kobe, TCU047, TCU072 and THU are selected for the ground acceleration inputs along the X direction of the following experimental study, as summarized in

Table 2. The 5% damped response spectra of these input acceleration histories normalized to a PGA value of 1g are illustrated in Fig. 4.

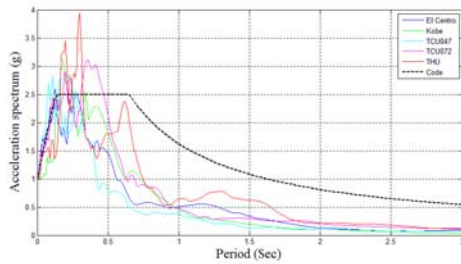


Fig. 4 Acceleration spectra of earthquake excitations
Table 1 Earthquake test program

Test Name	Earthquake Record	Test PGA
EL Centro	El Centro/I-ELC270, Imperial Valley, U.S., 1940/05/19	0.209g
Kobe	KJMA/KJM000, Kobe, Japan, 1995/01/16	0.167g
TCU047	Chi-Chi/TCU047, Chi-Chi, Taiwan, 1999/09/21	0.241g
TCU072	Chi-Chi/TCU072, Chi-Chi, Taiwan, 1999/09/21	0.190g
THU	Tohoku/THU, Tohoku, Japan, 2011/03/11	0.134g

Comparison of bare frame and experimental model with OBMD design

In this section, the results of the shaking table test will be demonstrated, and the isolation efficiency of the BMD will be evaluated based on the test data. In order to compare the maximum inter story drift between bare frame and specimen B3C2, Figure 5 are vertical distributions of maximum inter story displacement response, based on the results, compared to bare frame the specimen B3C2 can reduce the inter story drift of superstructure(above the control layer) more effective, make it like rigid motion behavior, however, for control the maximum inter story drift of substructure(below the control layer), the difference between specimen B3C2 and bare frame are quite small, but still smaller than bare frame. Figure 6 are vertical distributions of maximum acceleration responses, obviously, compared to bare frame the specimen B3C2 can reduce the maximum acceleration responses of both substructure and superstructure much effectively.

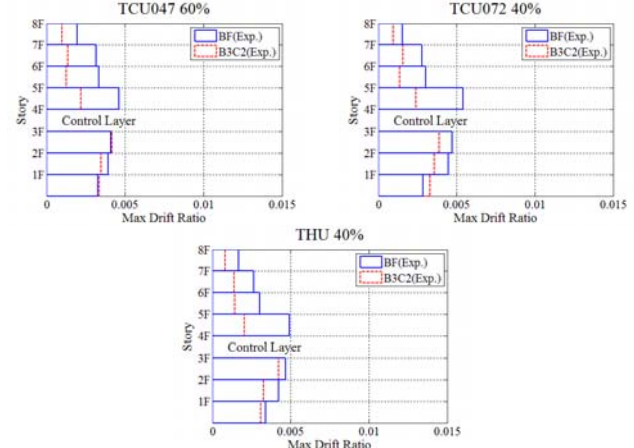
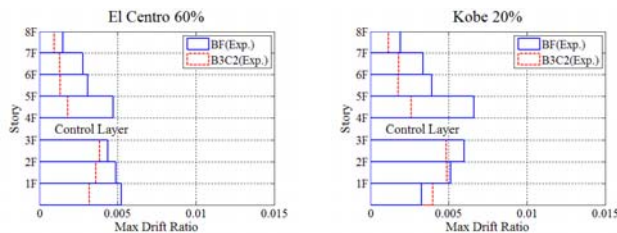


Fig. 5 Vertical distributions of maximum inter story displacement responses

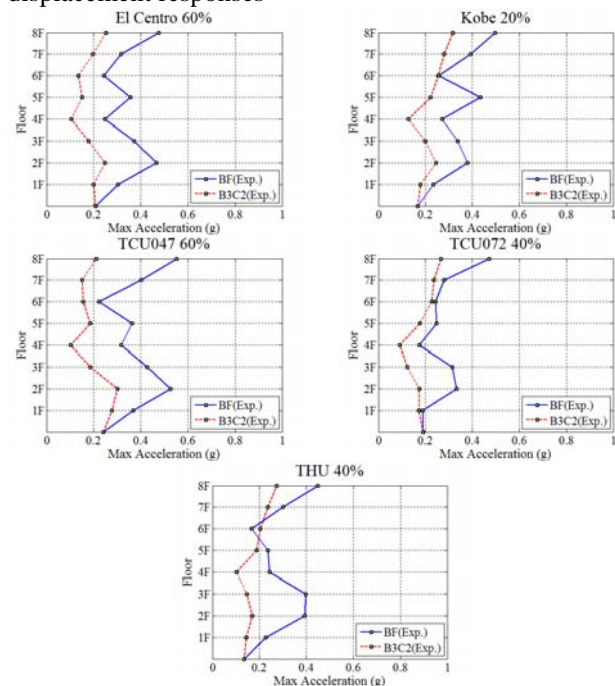


Fig. 6 Vertical distributions of maximum acceleration responses

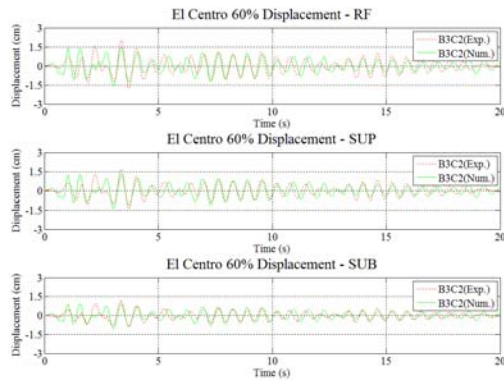
Comparison with Theoretical Results

In order to verify the feasibility of the BMD concept and the effectiveness of the optimum BMD design on seismic protection of buildings, the experimental data will be used to verify the BMD theory developed previously. To this end, Figure 7 Comparison of experimental and simulated responses of B3C2 frame subjected to the El Centro earthquake (PGA=0.209g). The theoretical responses are simulated by using the Sap2000 numerical tool. In Figure 7(a) and 8(b), the relative displacement (substructure, superstructure and roof) and absolute acceleration (substructure, superstructure and roof) are compared, respectively. the acceleration signals picked up by the accelerometer directly placed on the shaking table are taken as the input ground

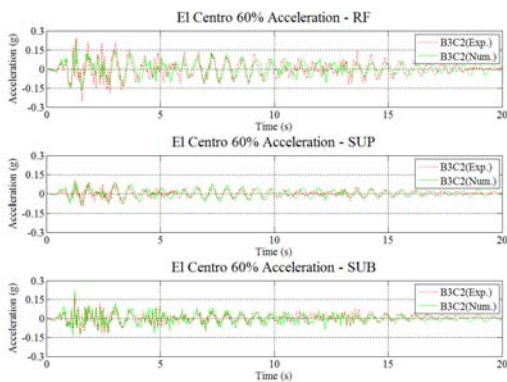
acceleration, so the theoretical system has the exactly same excitation as the experimental one. From Figures 7, it is observed that the simulated responses match much well with the experimental one, especially for the displacement responses. This indicates that the developed analysis method is able to accurately predict the seismic behavior of a BMD system. It also implies that the test data are reliable since they are consistent with the predicted ones.

provided.

The preliminary comparison discloses that the proposed optimum design method for the BMD system is practicable. In the next stage, Semi-active or active control devices can be considered at control layer. Also applications of BMD design to practical structures, especially for high-rise buildings, should be numerically studied to verify the feasibility of BMD in practical applications.



(a) Displacement time history



(b) Acceleration time history

Fig. 7 Comparison of experimental and simulated responses of B3C2 frame subjected to the El Centro earthquake (PGA=0.209g)

Concluding Remarks and Future Study

The BMD design has numerous advantages in which the most attractive feature is that the use of partial structural mass to be an energy absorber can solve the argument of insufficient tuned mass in the conventional TMD design. In this study, to protect both the primary structure and building mass absorber in the BMD design, an optimum design method is proposed. A series of numerical analyses and shaking table tests will be performed to verify the feasibility of the BMD concept and the effectiveness of the optimum BMD design on seismic protection of buildings. Based on the research results, the appropriate design procedures for practical applications of passive BMD systems will be

References

- Hartog Den J P. (1956), *Mechanical Vibrations*, 4th ed., McGraw-Hill, New York
- Rahul Rana and T. T. Soong (1997), "Parametric study and simplified design of tuned mass dampers", Eng. Struct.
- Sadek F, Mohraz B, Taylor AW and Chung RM (1997), "A Method of Estimating the Parameters of Tuned Mass Dampers for Seismic Applications", Earthq. Eng. Struct. Dyn., 26:617-635
- Tsai HC and Lin GC (1993), "Optimum Tuned-Mass Dampers for Minimizing Steady-State Response of Support-Excited and Damped Systems", Earthq. Eng. Struct. Dyn., 23:957-973
- Warburton GB and Ayorinde EO (1980), "Optimum Absorber Parameters for Simple Systems", Earthq. Eng. Struct. Dyn., 8:197-217
- Warburton GB (1981), "Optimum Absorber Parameters for Minimizing Steady-State Response", Earthq. Eng. Struct. Dyn.

Development of a Simplified Seismic Evaluation Program for Equipment in Hospitals

Tzu-Chieh Chien¹, Juin-Fu Chai² and Fan-Ru Lin³

簡子婕¹、柴駿甫²、林凡茹³

Abstract

In order to facilitate the issuing of governmental policies and practical engineering services regarding the seismic upgrading of hospitals, this study determines the seismic rehabilitation objectives of essential medical equipment and nonstructural components in hospitals responsible for emergency services. Further, it proposes seismic evaluation and strengthening guidelines. Owing to the onerous work required to improve the seismic performance of various nonstructural components, a simplified program is established using Microsoft Excel to execute a preliminary seismic evaluation and to retrofit the design of individual pieces of medical equipment. Users fill in details about the hospital information and the parameters of selected equipment; then, based on these entries, the program identifies the performance objective of each piece of equipment. It also determines whether the equipment requires retrofitting. In addition, the program can automatically check the preliminary designs of post-installation anchor bolts for seismic retrofitting against specified seismic demands.

Keywords: Nonstructural components, Hospital equipment, Simplified evaluation.

Introduction

The National Centre for Research on Earthquake Engineering released a report, “Rehabilitation Objectives and Evaluation Criteria for Hospitals” (Chai et al., 2013), to facilitate upgrading of hospital equipment such that hospitals possess the desired functional conditions for emergency services. This study follows these criteria prescribed by Chai et al. (2013), and to promote the evaluation process efficiency, a program is established to execute preliminary seismic evaluation for individual medical equipment.

This program uses Microsoft Excel spreadsheets, where the users fill information under the categories *Hospital Information*, *Equipment*, and *Bolt Information*. *Hospital Information* includes the seismic parameters and is the reference for equipment performance level estimation. *Equipment* includes details of all pieces of equipment in the hospital, and the program will estimate them one by one. If any equipment is determined to be strengthened, the information filled under *Bolt Information* serves as the

reference for that device in the strengthening evaluation.

Program Framework

Figure 1 shows the framework and flowchart of the proposed program. For the purpose of seismic evaluation for a hospital, users should follow the steps shown in the flowchart. First, to estimate the hazard level of an earthquake, the *Hospital Information* spreadsheet needs the basic parameters of the hospital; second, the *Equipment* spreadsheet requires the details of each piece of equipment for seismic evaluation, including its name, type, dimensions, and location. Finally, for the equipment-strengthening evaluation, information such as dimensions and test data of anchor bolts need to be entered into the *Bolt Information* spreadsheet, which would be then referenced to evaluate whether the equipment strength reaches the desired performance level.

¹ Research Assistant, National Center for Research on Earthquake Engineering

² Research Fellow, National Center for Research on Earthquake Engineering

³ Assistant Researcher, National Center for Research on Earthquake Engineering

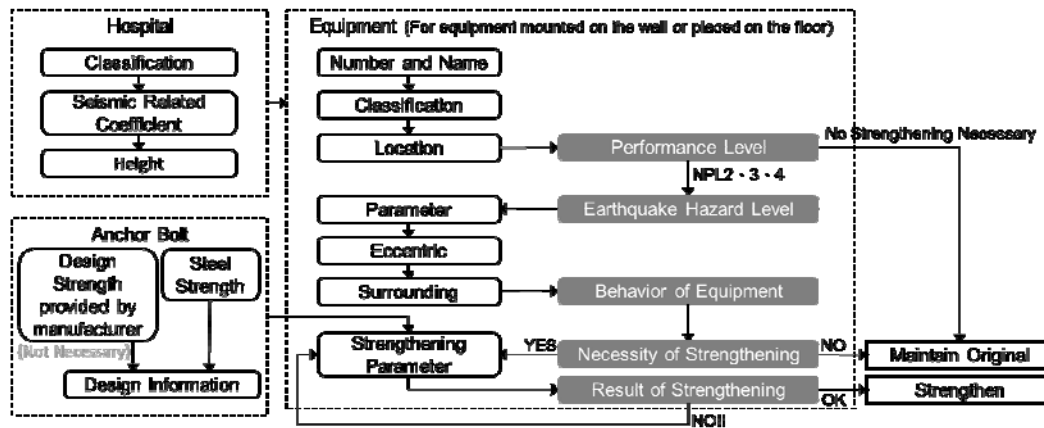


Figure 1. Framework and flowchart of the program

In Figure 1, the frame with dotted lines indicates the spreadsheets in the program and all the items in it. The frame with the gray background represents the data output by the program, determined from the information that the users filled in previously. For equipment that needs to be strengthened, an additional spreadsheet is used to display the seismic design of equipment retrofitted with anchor bolts.

Program Interface

Spreadsheet for Hospital Information

Figure 2 shows the spreadsheet for *Hospital Information*. The spreadsheet includes the classification and location of the hospital of interest, seismic parameters according to the Seismic Design Code (CPAMI, 2011), and the heights of each floor in the hospital.

For the first and second cells, hospitals are classified into three levels according to hospital accreditation: academic medical centers, metropolitan hospitals, and local community hospitals. Furthermore, hospitals designated responsible for acute services are classified into three levels: severe, moderate and general, according to their assigned capability for particular emergency treatments. For seismic site, the Seismic Design Code (CPAMI, 2011) is referenced. The red bordered cells can be filled by choosing from a drop down list of options, while the others cells need to be filled by typing in the information directly.

Spreadsheet for Equipment

Figures 3 and 4 show similar spreadsheets, to be filled for details regarding equipment placed on the floor and that mounted on the wall, respectively. For equipment placed on the floor, the program estimates whether the equipment has the potential to slide or overturn, while for equipment mounted on the wall, the program checks the seismic ability of the original anchorage.

In the *Equipment* spreadsheet, the first column shows the titles of the items to be filled, while the second column indicates the contents or the unit for each item. The cells that must be filled by a drop down list of options are noted in a corresponding cell. In the third column onward, the user must fill in each column with the details of each piece of equipment in the hospital in order to check their seismic ability.

The items consist of the information of the selected equipment (e.g., name, sort, location, weight, and height). Equipment can be classified according to types, sorts, and categories, whose details can be found in Chai et al.(2013). For the follow up, when the user chooses the location from the drop down list and enters the floor number in the corresponding cell, the location classification, as shown in Figure 5, is decided with staff members belonging to the hospital. Next, the parameters, including length, width, and height, and the eccentric condition are input, based on which the user measures equipment status device by device.

Hospital Accreditation :	Medical Center
Emergency Responsibility Hospitals :	General Designated Responsibility Hospitals
Coefficient in seismic code of Taiwan	
Site :	Near Fault
DBE Coefficient of Horizontal Design	0.8
Spectrum Acceleration-factor (S_g^D) :	
DBE Nea-Fault Factor(N_a) :	1.42
DBE Coefficient of F_a :	1
MCE Coefficient of Horizontal Design	1
Spectrum Acceleration-factor (S_g^M) :	
MCE Nea-Fault Factor(N_a) :	1.32
MCE Coefficient of F_a :	1
Floor	Height of Each Floor(cm)
RF	5450
15F	
14F	
13F	
12F	5050
11F	4650
10F	4250
9F	3950
8F	3450
7F	3050
6F	2650
5F	2100
4F	1580
3F	1050
2F	540
1F	0

Figure 2. Spreadsheet for hospital information

Number and Name		001	002	003
Number:		001	002	003
Name:		Electric Cabinet	Electric Cabinet	Electric Cabinet
Classification				
Types:	Drop Down List	Mechanical Equipment	Mechanical Equipment	Mechanical Equipment
Sorts:	Drop Down List	Electrical and communications	Electrical and communications	Electrical and communications
Categories:	Drop Down List	Electrical and communications	Electrical and communications	Electrical and communications
Location				
Location:	Drop Down List	Essential Care Areas	Essential Care Areas	Essential Care Areas
Floor:	Number (R for Roof, -1~-5 for Basement)	5	5	1
Parameter				
Weight (W _c) :	kgf	1100	1100	1100
Supporting Structural Component	Drop Down List	Floor	Floor	Floor
Dimension:				
	Length of X-Axes (L _x) m	0.80	0.80	0.80
	Length of Y-Axis (L _y) m	0.40	0.40	0.40
	Height (Container Included) (h) m	2.00	2.00	2.00
Distance between top to floor:	(Container Included) m	2.00	2.00	2.00
Eccentric				
X-Axis Eccentric :	(Filled with Y or N)	N	N	N
X-Axis Distance between the Edge to the Center of Gravity :	(Blank Space for Non-Eccentric or Uncertain) (L _{ec})			
Y-Axis Eccentric :	(Filled with Y or N)	N	N	N
Y-Axis Distance between the Edge to the Center of Gravity :	(Blank Space for Non-Eccentric or Uncertain) (L _{ec})			
Z-Axis Eccentric :	(Filled with Y or N)	N	N	N
Z-Axis Distance between the Edge to the Center of Gravity :	(Blank Space for Non-Eccentric or Uncertain) (h _c) m			
Surrounding				
Connection with Structure :	Drop Down List	Non-Fixed	Non-Fixed	Non-Fixed
Material of Floor Surface :	Drop Down List	Rubber	Rubber	Rubber
Material of floor :	Drop Down List	Concrete	Plastic flooring	Concrete
Lean on the Wall :	Drop Down List	Independent	Independent	Independent
Seismic Evaluation Required		Y	Y	Y
Performance Level		NPL3	No Necessary	NPL3
Earthquake Hazard Level		MCE	-	MCE
Seismic Response of Equipment		Sliding	-	Non
Necessary for Strengthening		Y	-	-
Bolt Strengthening	(Blank Space for No Strengthening Necessary)			
Total Number of bolts :		4		
Number of bolts on X-Axis:		2		
Number of bolts on Y-Axis:		2		
Type or Size:	Drop Down List	Hilti-M8		
Depth in concrete:	in	3.00		
Anchorage on Concrete or Other Material :	Drop Down List	Concrete		
Strength of Base Material :	psi	2700		
Result		OK	-	-

Figure 3. Spreadsheet for equipment placed on the floor

Number and Name		001	002	003
Number:		001	002	003
Name:		Electric Cabinet	Electric Cabinet	Electric Cabinet
Classification				
Types:	Drop Down List	Mechanical Equipment	Furniture contents	Mechanical Equipment
Sorts:	Drop Down List	Electrical and communications	Cabinet	Electrical and communications
Categories:	Drop Down List	Electrical and communications	Cabinet	Electrical and communications
Location				
Location:	Drop Down List	Essential Care Areas	Others	Emergency exit access
Floor:	Number (R for Roof, -1~-5 for Basement)	5	5	1
Parameter				
Weight (W _c) :	kgf	200	1000	4000
Dimension:				
	Length of X-Axes (L _x) m	0.40	1.00	0.40
	Length of Y-Axis (L _y) m	0.40	0.40	0.40
	Height (Container Included) (h) m	1.00	2.00	1.00
Distance between top to floor:	(Container Included) m	2.00	2.00	2.00
Eccentric				
X-Axis Eccentric :	(Filled with Y or N)	N	N	N
X-Axis Distance between the Edge to the Center of Gravity :	(Blank Space for Non-Eccentric or Uncertain) (L _{ec})			
Y-Axis Eccentric :	(Filled with Y or N)	N	N	N
Y-Axis Distance between the Edge to the Center of Gravity :	(Blank Space for Non-Eccentric or Uncertain) (L _{ec})			
Z-Axis Eccentric :	(Filled with Y or N)	N	N	N
Z-Axis Distance between the Edge to the Center of Gravity :	(Blank Space for Non-Eccentric or Uncertain) (h _c) m			
Original Bolt				
Total Number of bolts :		2	2	2
Number of bolts on X-Axis:		2	2	2
Number of bolts on Y-Axis:		4	4	4
Type or Size:	Drop Down List	Hilti-M8	Hilti-M8	Hilti-M8
Depth in concrete:	in	3.00	3.00	3.00
Anchorage on Concrete or Other Material :	Drop Down List	Concrete	Concrete	Concrete
Strength of Base Material :	psi	2500	2500	2500
Seismic Evaluation Required		Y	Y	Y
Performance Level		NPL3	NPL1	NPL2
Earthquake Hazard Level		MCE	-	MCE
Necessary for Strengthening		N	N	Y
Bolt Strengthening	(Blank Space for No Necessary Strengthen)			
Total Number of bolts :				3
Number of bolts on X-Axis:				2
Number of bolts on Y-Axis:				6
Type or Size:	Drop Down List			Hilti-M10
Depth in concrete:	in			3.00
Anchorage on Concrete or Other Material :	Drop Down List			Concrete
Strength of Base Material :	psi			2500
Result			-	OK

Figure 4. Spreadsheet for equipment mounted on the wall

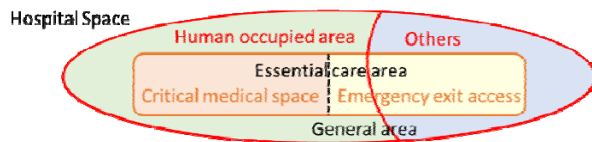


Figure 5. Classification of the hospital space

According to the values input in all the above-mentioned cells, the results of “Seismic Evaluation Required”, “Performance Level”, and “Earthquake Hazard Level” are shown in the cells with yellow background in the spreadsheet. Finally, for equipment placed on the floor, data regarding the surrounding situation should be input in order to determine the behavior of the equipment. For equipment having potential to slide or overturn, the output for the item “Strengthening Necessary” will be ‘Y’. For equipment mounted on the wall, the current situation about the anchor bolts should be entered in order to estimate the original seismic ability. If the anchor bolt does not have sufficient capacity, the output for the item “Strengthening Necessary” will be ‘Y’. Based on these outputs, the program determines whether the equipment should be retrofitted. For equipment that needs strengthening, the items under “bolt strengthening” can be used for a preliminary design of the anchor bolts for seismic retrofitting against the seismic demands specified automatically by the program.

Spreadsheet for Bolt Information

For equipment that needs the evaluation of anchor bolts, a database for target bolt strength should be prepared. The user must fill the anchor bolt spreadsheet shown in Figure 6. The data about the yield and ultimate stress and the various parameters of the anchor bolts in each specification provided by the manufacturer must be entered here. Furthermore, if available, the program prioritizes experimental test data provided by the manufacturer.

Once the details for strengthening anchor bolts information are filled, in the equipment-related spreadsheets, the program will determine whether the strength of the anchor bolts are sufficient or not based on the target values. After all, the target is that the seismic ability of all the pieces of equipment is satisfactory. If strengthening is required for any equipment, the user should make different trial-and-error entries under the bolt strengthening spreadsheet until the result displays ‘OK’.

Steel Strength of Anchor Bolt	(psi)		d _o	he(min)	Ase	N _p
	f _{ya}	f _{uta}				
	f _{ya}	92800				
	f _{uta}	116000				
Design Information of Anchor Bolt	Data	d _o	he(min)	Ase	N _p	
	Item Number	in	in	in ²	lb	
Design Information of Anchor Bolt	Hilti-M8	0.47	2.36	0.057	2810	
	Hilti-M10	0.59	2.76	0.090	4496	
	Hilti-M12	0.71	3.15	0.131		
	Hilti-M16	0.94	3.94	0.243		
Design Strength of Anchor Bolt in Different Base - Provided by Manufacturer)	φ T _n (psi)		Strength of Concrete			
	Item Number		2500	3000	4000	6000
Design Strength of Anchor Bolt in Different Base - Provided by Manufacturer)	Hilti-M8	1825	2000	2310	2830	
	Hilti-M10	2920	3200	3695	4525	
	Hilti-M12	4360	4775	5515	6755	
	Hilti-M16	6095	6675	7705	9440	
Design Strength of Anchor Bolt in Different Base - Provided by Manufacturer)	φ V _n (psi)		Strength of Concrete			
	Item Number		2500	3000	4000	6000
Design Strength of Anchor Bolt in Different Base - Provided by Manufacturer)	Hilti-M8	2160	2365	2730	3345	
	Hilti-M10	7685	8420	9720	11905	
	Hilti-M12	9390	10285	11880	14550	
	Hilti-M16	13125	14375	16600	20330	

Figure 6. Spreadsheet for bolt information

Conclusion and perspective

To facilitate the issuing of governmental policies and practical engineering services for the seismic upgrading of hospitals, the project “Seismic Evaluation and Strengthening Guidelines for Hospital Buildings” (Chai et al., 2013) was organized by the National Centre for Research on Earthquake Engineering. The seismic rehabilitation objectives of nonstructural components and systems in a hospital and the associated evaluation criteria were defined. Here, a program using Microsoft Excel was established for executing the seismic evaluation and retrofitting the design of individual items of medical equipment more easily and conveniently. Further studies are underway, including the development of a seismic evaluation and design program for equipment attached to the ceiling as well as for equipment strengthened by z-shape stoppers or welding.

References

- J.F. Chai et al., (2013), Seismic Evaluation and Strengthening Guidelines for Hospital Buildings, Taipei: National Center for Research on Earthquake Engineering, NCREE-13-037, 2013.
- Seismic Design Specifications and Commentary of Buildings, Construction and Planning Agency Ministry of the Interior (CPAMI), 2011.

Seismic Fragility Analysis of a Fire Sprinkler Piping System in a Hospital

Fan-Ru Lin¹, Pei-Wen Hu², Chang-Chen Yeh², Juin-Fu Chai³, Kuo-Chun Chang⁴

林凡茹¹ 胡佩文² 葉昶辰² 柴駿甫³ 張國鎮⁴

Abstract

Fire sprinkler piping systems are likely to become damaged during earthquakes, owing to their vulnerability and mechanical properties. Worse still, leakage and falling obstacles caused by damaged piping and adjacent ceiling systems significantly affect normal operation of critical buildings such as hospitals. This research aims to quantify the seismic capacity of sprinkler piping in hospitals by means of fragility curves, in order to conduct seismic evaluation or design its seismic performance. A typical sprinkler piping system in a medium-scale hospital in southern Taiwan, which was damaged in the 2010 Jiashian earthquake, is used as an example. Experimental results of *in situ* ambient vibration tests and shaking table tests of the piping sub-system are used to verify the accuracy of the numerical model, including hangers, screwed fittings of small-bore pipes, adjacent partition walls, and ceiling boards. Fragility curves of the sprinkler piping system are then established according to a large quantity of numerical analysis results, and a fragility analysis procedure is also suggested.

Keywords: Sprinkler piping systems, screwed fittings of pipes, fragility curves.

Introduction

Owing to improvements in seismic design for building structures, earthquakes do not necessarily result in damage to building structures, but instead may damage non-structural components and equipment. For instance, common seismic failures in hospitals include damage to fire sprinkler piping systems and tearing of adjacent ceiling panels. The leakages in piping and dust from broken ceiling boards during small earthquakes can result in not only a lack of fire protection and medical functions, but also malfunctions of medical equipment and the need to repair them. In strong earthquakes, broken piping segments may fall and further wound occupants and obstruct means of egress after the earthquake.

Adopting a medium-scale hospital as an example, this research aims to conduct a fragility analysis in order to develop seismic performance evaluation and design technologies for fire sprinkler systems in hospitals. The content of this research is summarized below:

1. Ambient vibration testing: An ambient vibration test in the example hospital is conducted using

velocimeters to clarify the structural characteristics of the building structure and the sprinkler piping system.

2. Numerical analysis of the piping system: A simplified numerical model of the fire sprinkler system in the example hospital is established for fragility analysis with SAP2000 software. Proper parameters for simulating 1-inch screwed fittings and gaps between adjacent partition walls or ceiling systems are proposed and verified through shaking table test results.

3. Fragility analysis of the piping system: Seismic fragility curves for the fire sprinkler system in the example hospital are constructed and verified against real damage states from the 2010 Jiashian earthquake. An analysis procedure for sprinkler piping systems in buildings is also suggested.

Ambient Vibration Testing

The ambient vibration test in the example hospital was conducted using velocimeters to clarify the structural characteristics of the building structure and the sprinkler piping system. With an understanding of

¹ Assistant Researcher, National Center for Research on Earthquake Engineering.

² Graduate Student, Department of Civil Engineering, National Taiwan University.

³ Researcher, National Center for Research on Earthquake Engineering.

⁴ Professor, Department of Civil Engineering, National Taiwan University.

the interaction relationship between the sprinkler piping system and the example hospital, numerical models of the example hospital and the sprinkler piping system were then constructed. The locations of the velocimeters at each elevation are shown in Fig. 1. The main frequencies of the piping system and the hospital structure are shown in Table 1.

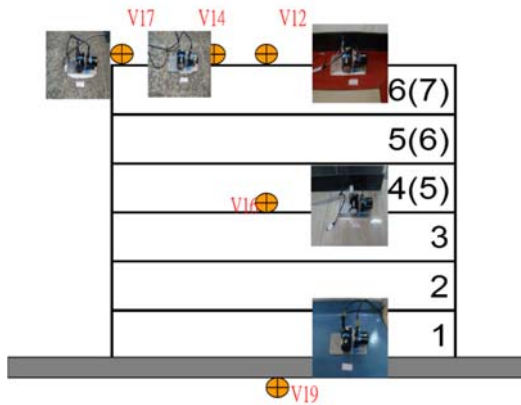


Fig. 1 Locations of velocimeters for ambient vibration testing.

Table 1 Main frequencies of the example hospital and the sprinkler piping system.

Perpendicular to the main pipe	Parallel to the main pipe
Main frequency of the sample hospital structure	
2.417 Hz	2.433 Hz
Main frequency of the sprinkler piping system	
5.322–6 Hz	11 Hz

Numerical Analysis of the Piping System

A simplified numerical model of the fire sprinkler piping system in the example hospital was established for fragility analysis using SAP2000 v.15 software. In reality, sprinkler piping systems in buildings typically contain many non-linear components, especially at the interface between the hanger and the piping system and between the piping system and the ceiling system. Therefore, appropriate parameters to simulate the threaded joint in a piping system and the gap between adjacent partition walls or ceiling systems were proposed and verified through shaking table test results.

According to the hysteresis loop found from the component tests, the behavior of the threaded joints is close to linear, so they can be simulated with linear links in the numerical model. Partition walls and the ceiling system are the most common adjacent components at the ends of sprinkler piping. After the Jiashian earthquake, a leakage failure was observed in the example hospital at a location where piping passed

through the partition wall. The reason for this failure was that the opening of the partition wall was smaller than the displacement of the piping system during the earthquake. This led to impacts between the piping system and the partition wall and resulted in a higher acceleration response in the piping system. In order to simulate this behavior, a non-linear link element “gap” is required for the numerical model. A similar phenomenon is observed between the sprinkler heads and ceiling, and again a non-linear gap link element is used to simulate impact effects. The numerical model of the sprinkler piping system is shown in Fig. 2. Comparisons between the results of numerical analysis and the experimental results are shown in Fig. 3 to Fig. 6.

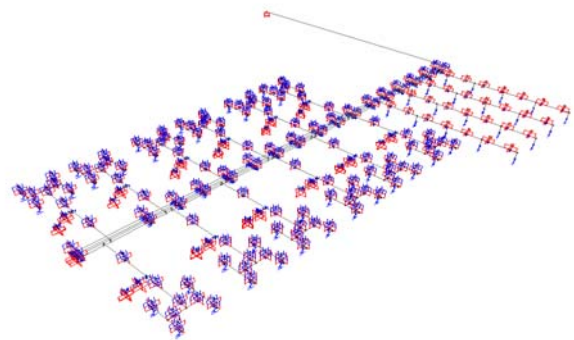


Fig. 2 Numerical model of the piping system.

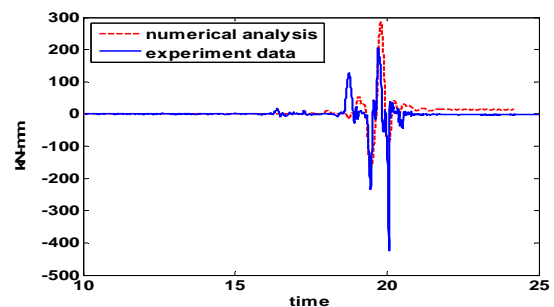


Fig. 3 Moment response of the 1-inch threaded joint under the Jiashian earthquake.

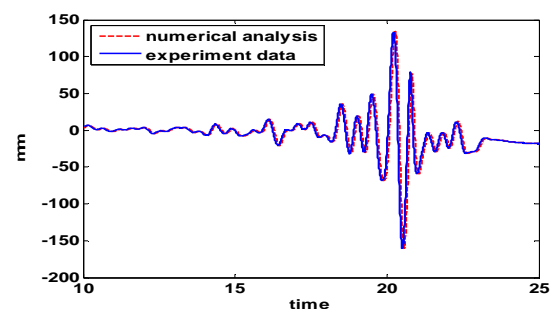


Fig. 4 Displacement response of the 1-inch threaded joint under the Jiashian earthquake.

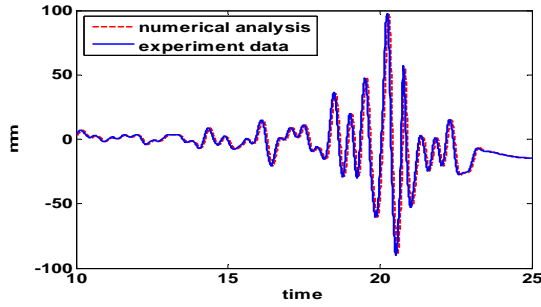


Fig. 5 Displacement response of the partition wall under the Jiashian earthquake.

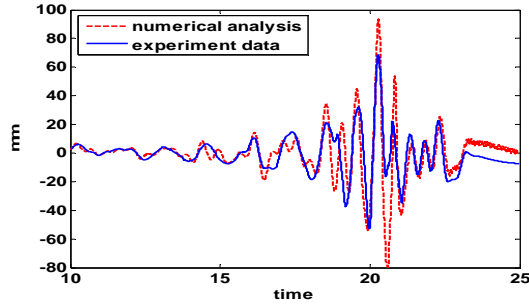


Fig. 6 Displacement response of the ceiling under the Jiashian earthquake.

Fragility Analysis of the Piping System

This research proposes a fragility analysis procedure for a sprinkler piping system. The first step is to select an earthquake. Ten different time-histories recorded from nearby strong-motion stations were selected, with earthquake magnitudes ranging from 6.4 to 7.3 on the Richter magnitude scale. The second step is to obtain the floor response acceleration by inputting the selected earthquake into the numerical model of the example hospital. The resulting floor response acceleration was used as the input for the sprinkler piping system. The final step is to conduct fragility analysis.

Prior to the second step to conduct numerical analysis of the example hospital, the input time-histories were complied with a normalization process according to FEMA P695 (Federal Emergency Management Agency). First, the peak ground velocity is adjusted to the median value of the ten peak ground velocities in two directions. Note that each time-history has different normalization factors. Next, the time-histories are scaled to eight spectral acceleration levels from 0.02 g to 1 g. Each time history is scaled by the same factor, *i.e.*, the median spectral acceleration at the fundamental period of the building out of the ten time histories to the analysis level.

The fragility function of the piping system can be expressed by a cumulative distribution function on a lognormal scale:

$$F(D) = \Phi\left(\frac{\ln(D/\theta)}{\beta}\right), \quad (1)$$

where Φ denotes the standard normal (Gaussian) cumulative distribution function, θ denotes the

median value of the probability distribution, and β denotes the logarithmic standard deviation. In FEMA P58 (Federal Emergency Management Agency), D indicates the Engineering Demand Parameter (EDP), such as peak ground motion (PGA) or peak floor acceleration (PFA). In this research, different kinds of EDP were used to investigate the sensitivity of the expression of the fragility of sprinkler piping in buildings. Fig. 7, Fig. 8, and Fig. 9 depict respectively the fragility of the adjacent ceiling system; the fragility of the threaded joint of a 1-inch pipe, which is the most vulnerable part of the piping system; and the fragility of the hangers of the piping system. In Fig. 8, the threaded joint is found to have an over 50% chance of being damaged under the level of the Jiashian earthquake (0.168 g). The adjacent ceiling system is easily damaged in small-scale earthquakes, in comparison to the piping system (Fig. 7). However, PFA is a more appropriate EDP than PGA for vulnerable components such as ceiling systems.

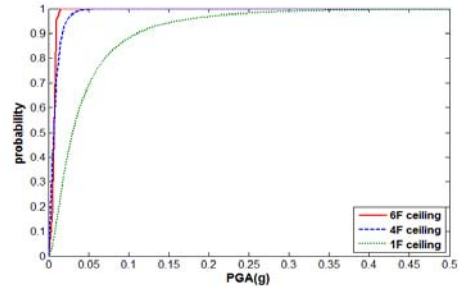


Fig. 7 Fragility curves for ceiling systems.

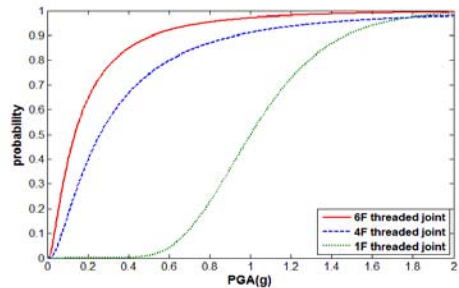


Fig. 8 Fragility curves for the 1-inch pipe.

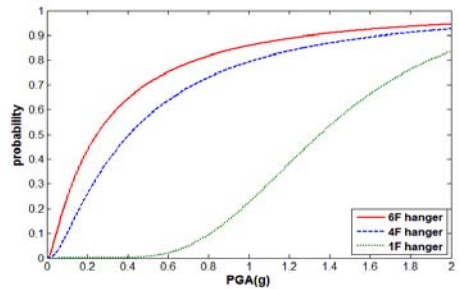


Fig. 9 Fragility curves for the hangers.

Conclusion

This study constructed non-structural fragility curves for an example hospital and verified them against the real damage states under the 2010 Jiashian earthquake. A fragility analysis procedure for sprinkler piping systems in buildings was also suggested. The analysis results showed that the fragility curve can predict leakage effects of the threaded joint and the failure probability of a ceiling. Using peak ground acceleration (PGA) as the Engineering Demand Parameter (EDP) is more convenient for the design of non-structural components in structural engineering, compared to using peak floor acceleration (PFA). However, PFA is recommended for use as the EDP index to obtain a more accurate performance evaluation. It is found that the seismic performance of the sprinkler piping system would be improved if the example hospital followed the NFPA 13 criteria in its design.

Future study would involve upgrading seismic improvement devices on the sprinkler piping system. For example, the connection between the pipe and the sprinkler head can be replaced by a flexible hose, and the vulnerable threaded joint can be replaced by a flexible coupling joint, which has a larger rotational capacity. After arranging seismic improvement devices, the fragility analysis and shaking table tests will be conducted again to verify their benefits to sprinkler piping systems.

References

- George Antaki, Aiken, SC. Various (2002), Seismic Design and Retrofit of Piping Systems July 2002, American Lifelines Alliance.
- Minimum Design Loads for Buildings and Other Structures, American Society of Civil Engineers.
- Standard for The Installation of Sprinkler Systems 2010 Edition, NFPA.
- Approval Standard for Pipe Couplings and Fittings for Aboveground Fire Protection System, Class Number 1920, November 2007, FM Approval LLC.
- Timber structures - Joints made with mechanical fasteners - Quasi-static reversed cyclic test method, International Organization for Standardization.
- Suneel K. Gupta, et al. (2007), Effects of Simulated Seismic Loading on LBB Assessment of High Energy Piping, Bhabha Atomic Research Center.
- Bu Seog Ju, et al. (2011), Fragility Analysis of Threaded T-Joint Connections in Hospital Piping Systems, ASME 2011 Pressure Vessel and Piping Division Conference.
- Arash E. Zoghi, E, Manos Maragakis, Ahmad Itani, Elliott Goodwin(2012), Experimental and Analytical Studies of Hospital Assemblies Subjected to Seismic Loading, Earthquake Engineering Research Institute.
- Qualification of building seismic performance factors (2009), FEMA P695.
- K.C. Kuo, et al. (2012), Experimental Evaluation of the Seismic Performance Hospital Sprinkler Systems, NCREE.
- Seismic Performance Assessment of Buildings (2012), FEMA p-58-1.

Modelling Contact and Collapse Behavior of Neighboring Trusses with VESEN

Wei-Tze Chang ¹

張慰慈 ¹

Abstract

Modern structures often face uncertain external environments caused by severe natural disasters and man-made impacts. The subsequent member failure and collapse of neighboring structures is difficult to illustrate using continuum-based numerical methods. For modelling such a complex structural system, this study proposes a coupled continuous–discontinuous method by integrating two explicit-form numerical methods, the Vector Form Intrinsic Finite Element method and the Discrete Element Method. To achieve the proposed simulation, an object-oriented software platform, named VESEN (Versatile Engineering Simulation ENvironment), designed by the National Center for Research on Earthquake Engineering under the National Applied Research Laboratories in Taiwan, is used. Object-oriented programming technology and design patterns in software engineering are used to facilitate the usability and extensibility of VESEN software for adapting to future changes in requirements. Simulation results are presented for an example of a two-truss collapse system.

Keywords: Versatile Engineering Simulation Environment, Vector-Form Intrinsic Finite-Element Method, Discrete Element Method, coupled continuous–discontinuous simulation.

Background

Old residential areas or construction sites often consist of neighboring structures with narrow distances between them, leading to a high risk of contact and collapse during earthquakes. The subsequent dynamic behavior involves large-scale deformation, movement, and failure of members; this behavior relates to the knowledge of failure and contact theory and is difficult to illustrate. Thus, we consider the introduction of a coupled continuous–discontinuous simulation to study such a complex engineering problem. Two explicit-form numerical methods, the vector-form intrinsic finite-element (VFIFE) method and the discrete element method (DEM), were chosen because they can deal with continua and discontinua.

However, in software development for this type of simulation, integrating different numerical methods while retaining the flexibility of the software is difficult. To address this issue, the National Center

for Research on Earthquake Engineering (NCREE) under the National Applied Research Laboratories (NARLabs) in Taiwan initiated a project in 2011 to design an in-house software platform using a particle-based method (PBM) for the purpose of modelling multi-hazard phenomenon. The platform was named the Versatile Engineering Simulation Environment, or VESEN (Chang, *et al.*, 2013 & 2014).

VESEN has recently been integrated with two PBMs, the VFIFE method and DEM. VFIFE discretizes a structure into control points instead of elements for solving the governing equations. Continuity constraints are not enforced in the VFIFE method, which makes it capable of simulating large-scale motion, deformation, and even failure behavior of structures. Meanwhile, the DEM focuses on modelling granular and discontinuous materials and efficiently integrates contact theory and various algorithms, thus providing VESEN with the ability to

¹ Assistant Researcher, National Center for Research on Earthquake Engineering

deal with complex interactions between solid interfaces.

Contact Procedure

The numerical contact procedure in VESEN follows the contact theory in DEM and can be divided into three stages: (1) contact detection, (2) impulse solving, and (3) impulse application (see Fig. 1). In the first stage (steps A to C), the boundary (influence range) of an element and several control points are illustrated with the assigned geometric

shape. For example, a truss member is controlled by a line element and two points. Its boundary can be described as a cylinder, as shown in Fig. 2. The radius and length will change during simulation according to the position of the two control points to ensure conservation of mass. After considering geometric shapes with the position and orientation of two elements, contact information (e.g., contact point, contact direction, and overlap between two elements) can be determined.

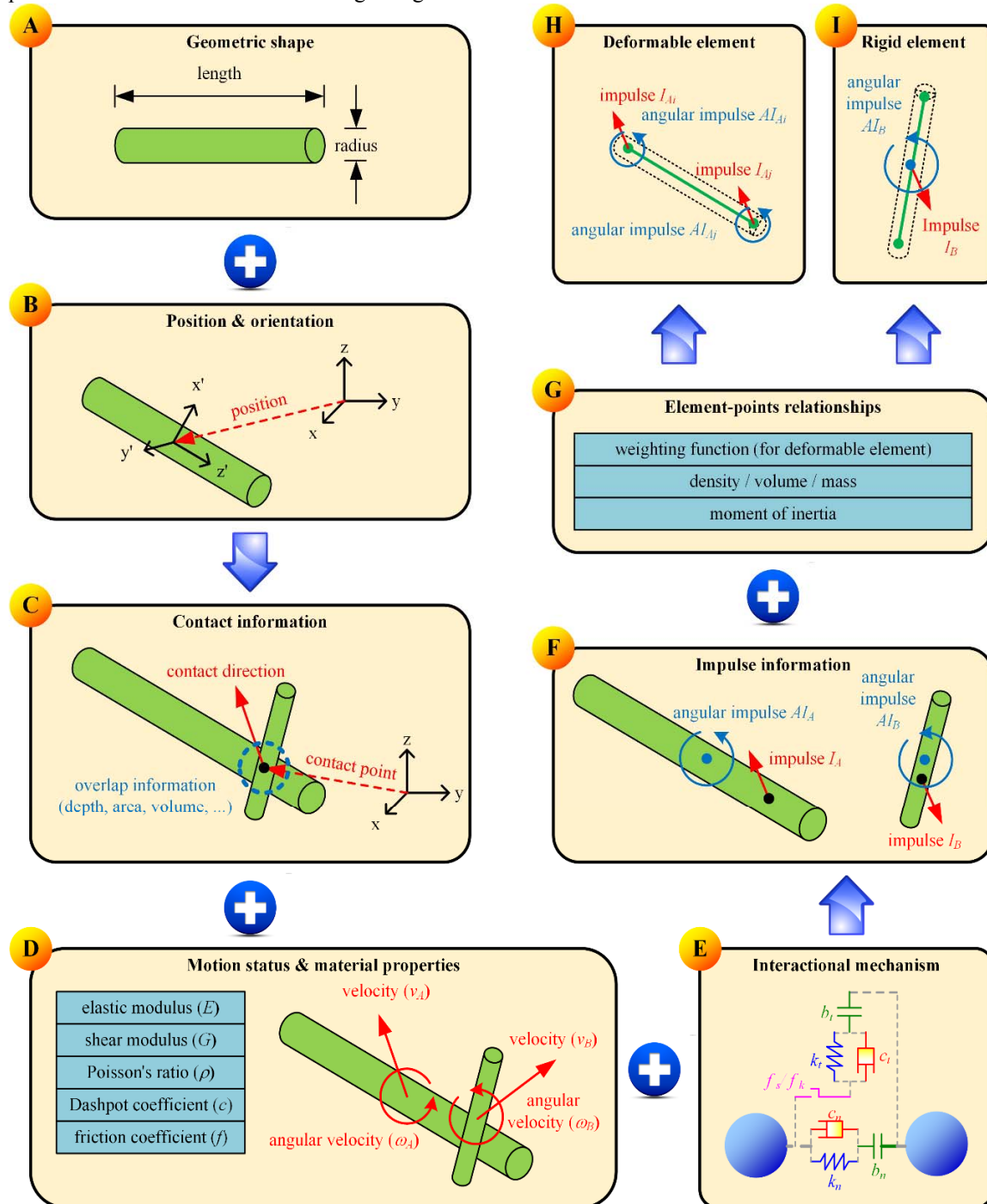


Fig. 1: Numerical contact procedure in VESEN: contact detection (A to C), impulse solving (C to F), and impulse application (F to I).

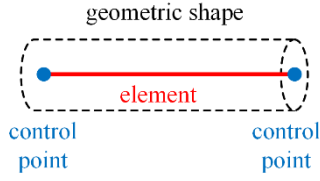


Fig. 2: Relationship between element, points, and geometric shape in VESEN.

Two-quasi-cylinder Contact Detection Algorithm

Following the three-stage contact procedure, we define the geometric shapes of the truss members in order to analyze a truss system. A quasi-cylinder shape combined with a cylinder with two half-spherical ends is used for defining the boundary of a truss member with a circular cross-section; this helps avoid the singular condition in determining contact points and their direction. Then, a two-quasi-cylinder contact detection algorithm is applied. This paper classifies five different conditions for two quasi-cylinders, as shown in Fig. 3. For two skew lines as conditions A and B, a common perpendicular line that indicates their nearest distance can be determined (see Fig. 3). Considering radii r_A and r_B of the two cylinders in contact, the overlap depth d can be calculated as:

$$d = \max\{0, r_A + r_B - \overline{PQ}\}, \quad (1)$$

and the vector perpendicular to the common perpendicular line indicates the contact direction. For conditions C and D, there is no single solution for the common perpendicular line. We define the corresponding contact information as shown in Fig. 3.

The above four conditions are sufficient for contact detection in the DEM but not for the truss system. For two truss members (line elements) connected with a hinge joint (control point), the common perpendicular line reduces to a point on the joint, so the contact direction and overlap depth cannot be determined. In this study, we define a minimal allowable angle α_{min} between two truss members, that is, the angle of the central lines of two line elements. When angle α is less than α_{min} , the corresponding contact information can be determined as shown in Fig. 3 (E).

Numerical Example and Simulation Results

Two 72-member truss systems (Fig. 4) (Sun, *et al.*, 1995) were chosen to show the contact and collapse behavior modelled by VESEN using the proposed two-quasi-cylinder contact detection algorithm.

Young's modulus $E = 10^4$ ksi and density $\rho = 0.1$ lbs/in³. Vertical loads of 5 kip are added on each hinge joint of the roof. The initial areas of the circular cross-sections of the truss members are shown in Table 1. A double-height 72-member truss was located within 10 in from the side of the first truss. In this design, the second truss has a longer natural period than the lower one; thus, the two trusses have different dynamic behaviors even under the same earthquake. The base excitation given is the sine profile and the corresponding base displacement is:

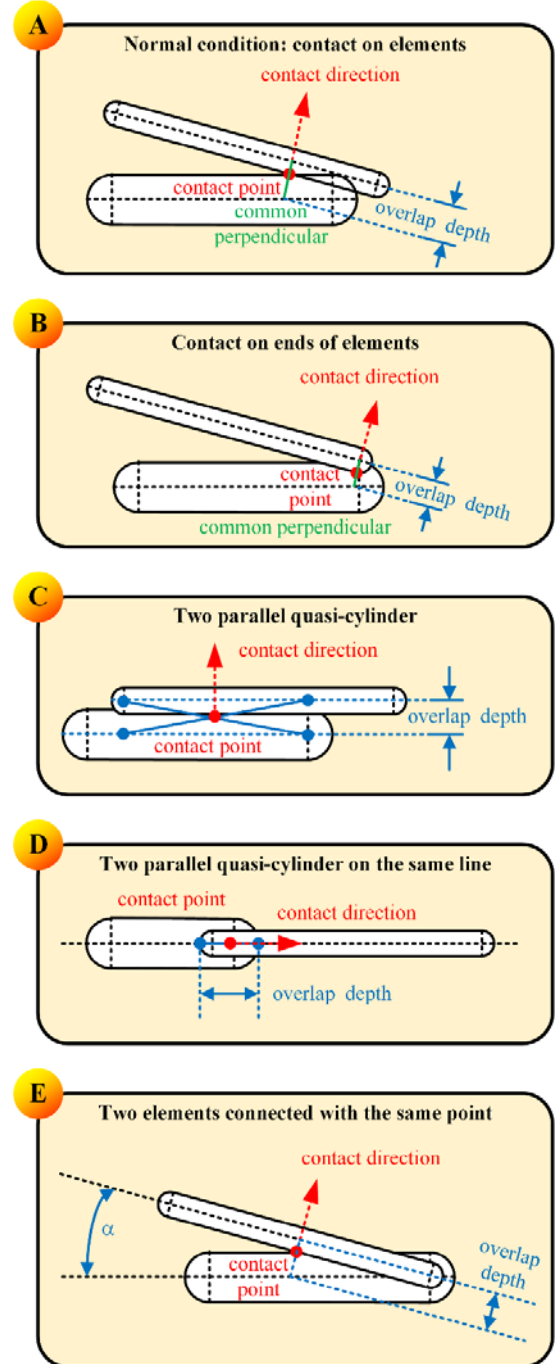


Fig. 3: Five contact conditions between two quasi-cylinders in this study.

$$D = \begin{cases} 10 \sin(10t) & t \leq 1 \\ 0 & t > 1 \end{cases}, \quad (2)$$

where t is the simulated time. The simulation time step is $\Delta t = 10^{-4}$ s.

To study the failure behavior of the truss members, this study uses a common linear spring–dashpot (LSD) interaction model in contact theory with a normal spring stiffness k_n of 10^4 kip/in and a normal damping ratio ζ of 0.02. The maximal allowable strain of each truss member in both compression and tension is 0.05. If the strain of a truss member exceeds the allowable strain, then it is considered to have failed and its ends will be released from the main truss system. The dynamic failure behavior is shown in Fig. 4. The first contact between the truss members occurs at $t = 0.2$ s, following which both trusses fail.

Conclusion

This study proposed a numerical procedure for modelling contact and collapse behavior of interactive truss systems using a coupled continuous–discontinuous method. A two-quasi-cylinder contact detection algorithm is designed to overcome the difficulty in determining the contact information between two truss members. By successfully modelling the collapse behavior of two-truss interaction systems under base excitation, it has been shown that the proposed procedure and algorithm are workable and acceptable.

References

Chang, W.-T., Wang, R.-Z., Hsieh, S.-H., Wang, C.-Y. and Chang, K.-C. (2013). Design of A VFIFE-DEM Coupled Simulation Platform,” *Proceedings of the Conference on Computer Applications in Civil and Hydraulic Engineering 2013*, National Taipei University of Technology,

Taipei, Taiwan, September 5-6, 2013, Paper No. 1131, 2013. (in Chinese).

Chang, W.-T., Wang, R.-Z., Hsieh, S.-H. (2014). Wang, C.-Y. and Chang, K.-C. “Design of A Versatile Engineering Simulation ENvironment for Coupled Continuous-discontinuous Simulation,” *Proceeding of the 2014 International Conference on Computing in Civil and Building Engineering*, Issa, R. R. ed., Orlando, Florida, United States, June 23-25, 2014, pp. 1328-1335, 2014.

Sun, H.-C., Chai, S. and Wang, Y.-D. (1995). *Discrete Optimum Design of Structures*, Dalian University of Technology.

Table 1 Initial areas of circular cross-sections of truss members in this study.

Truss member with serial number of joints (Sun, <i>et al.</i> , 1995)	Initial area (in ²)
(1, 5) (2, 6) (3, 7) (4, 8)	0.2
(2, 5) (1, 6) (3, 6) (2, 7)	0.6
(4, 7) (3, 8) (1, 8) (4, 5)	
(1, 2) (2, 3) (3, 4) (4, 1)	0.5
(1, 3) (2, 4)	0.5
(5, 9) (6, 10) (7, 11) (8, 12)	0.5
(6, 9) (5, 10) (7, 10) (6, 11)	0.6
(8, 11) (7, 12) (5, 12) (8, 9)	
(5, 6) (6, 7) (7, 8) (8, 5)	0.1
(5, 7) (6, 8)	0.1
(9, 13) (10, 14) (11, 15) (12, 16)	1.1
(10, 13) (9, 14) (11, 14) (10, 15)	0.5
(12, 15) (11, 16) (9, 16) (12, 13)	
(9, 10) (10, 11) (11, 12) (12, 9)	0.1
(9, 11) (10, 12)	0.1
(13, 17) (14, 18) (15, 19) (16, 20)	1.9
(14, 17) (13, 18) (15, 18) (14, 19)	0.5
(16, 19) (15, 20) (13, 20) (16, 17)	
(13, 14) (14, 15) (15, 16) (16, 13)	0.1
(13, 15) (14, 16)	0.1

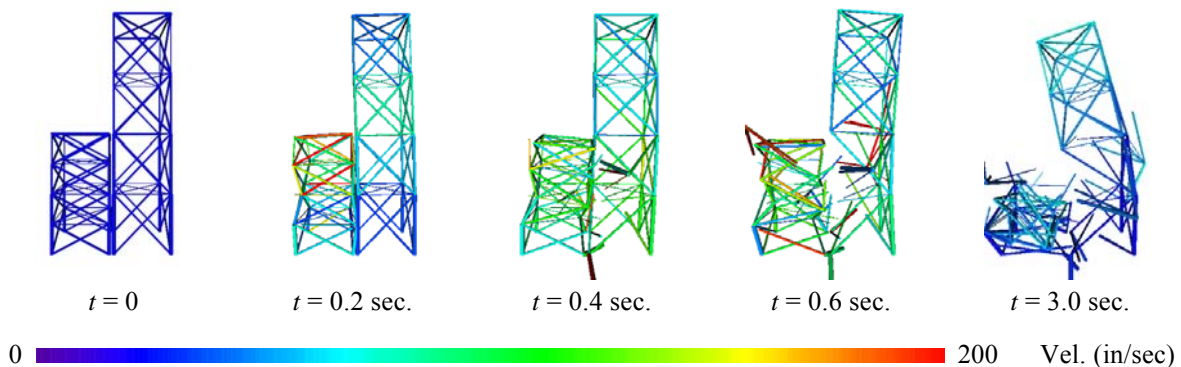


Fig. 4: Dynamic behavior of two neighboring truss systems excited by a sine wave on the ground.

A Study on Seismic Fragility of Water Distribution Reservoirs and Pipe Bridges

Gee-Yu Liu¹

劉季宇¹

Abstract

This study establishes an inventory of water distribution reservoirs and pipe bridges in central Taiwan in 1999. Details of their structural properties and damage states resulting from the 1999 Chi-Chi earthquake are calibrated. They are employed to develop the parameters of seismic fragility curves for these water supply facilities.

Keywords: water supply facilities, distribution reservoirs, water pipe bridges, seismic fragility

Introduction

The seismic performance of water supply systems relies not only on the ruggedness of the pipeline network but also on the robustness of the facilities in the systems. Water supply facilities consist of aqueducts, water treatment plants, water storage tanks (distribution reservoirs), pumping stations, pipe bridges, *etc.* For the purpose of seismic hazard mitigation of water supply systems, it is very important to take into account the seismic fragility of these facilities. In the literature, only the HAZUS Earthquake Model (FEMA, 2010) provides detailed fragility models for potable water systems. During the Chi-Chi earthquake, water distribution reservoirs and pipe bridges were severely damaged, having a huge impact on water transmission and distribution in central Taiwan. Improved fragility models for these facilities based on local characteristics and damage data are urgently needed.

In this study, a database of 38 major distribution reservoirs (including clear water tanks in water treatment plants) and four water pipe bridges in central Taiwan, as of 1999, as depicted in Fig. 1, is established. These facilities are under the Fourth Branch (Taichung and Nantou) of the Taiwan Water Corporation. Details of their structural properties and damage states resulting from the 1999 Chi-Chi earthquake were calibrated and are depicted in Fig. 2. Furthermore, the measured ground shaking and permanent ground deformation (洪祥瑗等, 2007) were used to determine the actual hazards of each of the facilities that were affected by the Chi-Chi earthquake. All of these data were employed to

develop the medians (M) and logarithmic standard deviations (LSD) of log-normal fragility curves at various damage states (FEMA, 2010) for each type of facility.

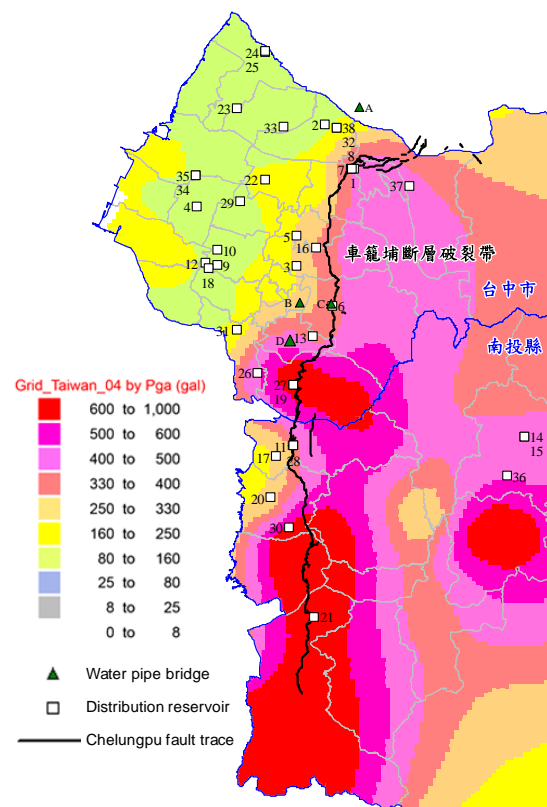


Fig. 1 Location of water distribution reservoirs and pipe bridges, and the distribution of peak ground acceleration during the Chi-Chi earthquake.

¹ Research Fellow, National Center for Research on Earthquake Engineering, karl@ncree.narl.org.tw



Fig. 2 Damages to water distribution reservoirs and pipe bridges due to the Chi-Chi earthquake.

Fragility of Water Distribution Reservoirs

In Taiwan, water distribution reservoirs (including clear water tanks) are reinforced concrete (RC) structures. Occasionally, pre-stressed RC structures are employed for large circular reservoirs. RC structures can be divided in terms of structure into two different classes. One is termed “framed” structures, as they share a moment-resisting base-wall system founded on a common mat. Accordingly, the other is termed “non-framed” structures, as they lack that feature. Theoretically, a framed structure has a better seismic performance than a non-framed structure. Water distribution reservoirs can also be divided into two classes based on the place of installation. The first is called “on grade” (*i.e.*, above ground) and the other is buried/partially buried. Due to the confinement effect from the surrounding soil, the later class of distribution reservoirs performs better than the former under seismic excitation.

As a result, it is recommended in this study that, for on-grade RC distribution reservoirs, the seismic fragility due to both ground shaking (peak ground acceleration, *g*) and permanent ground deformation (cm) should be considered. Meanwhile, for buried and partially buried RC distribution reservoirs, seismic fragility only due to permanent ground deformation should be considered. Accordingly, parameters for the fragility curves describing the probabilities of reaching or exceeding various damage states for each type of distribution reservoir are proposed, based on

the 38 samples, including seven damaged samples, as summarized in Tables 1 and 2.

Table 1 Parameters of the fragility curves at various damage states for on-grade RC distribution reservoirs.

Fragility due to ground shaking			
Class	Damage state	M (g)	LSD
Non-framed	Slight	0.40	0.55
	Moderate	0.60	0.60
	Extensive	0.80	0.65
	Complete	1.00	0.70
Framed	Slight	0.80	0.55
	Moderate	1.00	0.60
	Extensive	1.20	0.65
	Complete	1.60	0.70
Fragility due to permanent ground deformation			
Class	Damage state	M (cm)	LSD
Non-framed	Slight	10	0.50
	Moderate	20	0.50
	Extensive	30	0.50
	Complete	40	0.50

Framed	Slight	60	0.50
	Moderate	80	0.50
	Extensive	100	0.50
	Complete	120	0.50

Table 2 Parameters of fragility curves at various damage states for buried and partially buried RC distribution reservoirs.

Fragility due to permanent ground deformation			
Class	Damage state	M (cm)	LSD
Non-framed	Slight	30	0.50
	Moderate	40	0.50
	Extensive	50	0.50
	Complete	60	0.50
Framed	Slight	60	0.50
	Moderate	80	0.50
	Extensive	100	0.50
	Complete	120	0.50

Fragility of Water Pipe Bridges

In Taiwan, most water pipe bridges are very simply constructed. The pipe, with or without stiffening measurement, supports itself as the girder of a bridge. Under such circumstances, the entire superstructure is structurally weaker than the lower structure of the bridge. Since there is no deck in the superstructure, the width of the bridge is narrow and the piers consist of single-column bents instead of multiple-column bents or pier walls. In this study, they are termed as “simple/stiffened” pipe bridges. On the other hand, some water pipe bridges are complex in design. The water pipes in these bridges are supported by steel girders or arches, or they are trussed, cable-stayed, or suspended superstructures. These water pipe bridges are generally sophisticatedly engineered and, as a result, have elaborate seismic behaviors. In this study, these bridges are called “special” pipe bridges.

Compared to the classification of highway bridges proposed in an earlier study (交通部公路總局, 2008), simple/stiffened pipe bridges appear to be equivalent to the highway bridges with multiple spans, simply supported superstructures, and piers of single-column bents, while special pipe bridges appear to be equivalent to those classified as “special highway bridges”. The same study also recommended that highway bridges should be further classified according to their year of construction (before or after 1995), which decides whether or not they are seismically designed.

Based on the same study, the parameters of the fragility curves describing the probabilities of reaching or exceeding various damage states for each class of highway bridge can be modified to determine

those for water pipe bridges. Tables 3 and 4 summarize the proposed values based on four samples, including one damaged case. Fragility due to ground shaking (spectral acceleration at a structural period of 1.0 s, g) and permanent ground deformation (cm) have both been considered.

Table 3 Parameters of fragility curves at various damage states for simple/stiffened pipe bridges.

Fragility due to ground shaking			
Class	Damage state	M (g)	LSD
Conventionally designed (constructed before 1995)	Slight	0.474	0.55
	Moderate	0.599	0.50
	Extensive	0.683	0.45
	Complete	0.956	0.40
Seismically designed (constructed in or after 1995)	Slight	0.522	0.55
	Moderate	0.781	0.50
	Extensive	0.954	0.45
	Complete	1.336	0.40
Fragility due to permanent ground deformation			
Class	Damage state	M (cm)	LSD
Conventionally designed (constructed before 1995)	Slight	15	0.45
	Moderate	30	0.40
	Extensive	45	0.35
	Complete	60	0.30
Seismically designed (constructed in or after 1995)	Slight	20	0.45
	Moderate	40	0.40
	Extensive	60	0.35
	Complete	80	0.30

Table 4 Parameters of fragility curves at various damage states for special water pipe bridges

Fragility due to ground shaking			
Class	Damage state	M (g)	LSD
Conventionally designed (constructed before 1995)	Slight	0.560	0.55
	Moderate	0.718	0.50
	Extensive	0.824	0.45
	Complete	1.154	0.40
Seismically designed (constructed in or after 1995)	Slight	0.644	0.55
	Moderate	0.927	0.50
	Extensive	1.115	0.45
	Complete	1.561	0.40
Fragility due to permanent ground deformation			
Class	Damage state	M (cm)	LSD

Conventionally designed (constructed before 1995)	Slight	18	0.45
	Moderate	36	0.40
	Extensive	54	0.35
	Complete	90	0.30
Seismically designed (constructed in or after 1995)	Slight	20	0.45
	Moderate	40	0.40
	Extensive	60	0.35
	Complete	100	0.30

Concluding Remarks

In this study, the medians and logarithmic standard deviations of log-normal fragility curves at various damage states for water distribution reservoirs (including clear water tanks in water treatment plants) and pipe bridges were proposed. Seven damaged water distribution reservoirs and one damaged water pipe bridge during the Chi-Chi earthquake were re-examined using the proposed fragility curves and parameters. As summarized in Table 5, the simulated damage states for each facility agree well with the actual damage state. More details of this study and its research findings can be found in the technical report published by the Water Resources Agency, MOEA (經濟部水利署, 2015).

Table 5 Comparison between actual and simulated damage states of water distribution reservoirs and pipe bridges during the Chi-Chi earthquake.

ID	Facility name	Class	Actual damage state	Simulated damage state
1	50,000-ton Clear Water Tank, Feng-Yuan Second Water Treatment Plant	Non-framed, Buried	Extensive	Complete
6	Now-Guan 18,000-ton Distribution Reservoir	Non-framed, On-grade	Complete	Complete
7	17,000-ton Clear Water Tank, Feng-Yuan First Water Treatment Plant	Non-framed, Partially buried	Complete	Complete
8	15,000-ton Clear Water Tank, Feng-Yuan First Water Treatment Plant	Non-framed, Partially buried	Complete	Complete
11	6,000-ton Clear Water Tank, Cao-Tun Water Treatment Plant	Non-framed, Buried	Slight	Complete
17	4,000-ton Clear Water Tank, Lin-Zi-Tou Water Treatment Plant	Non-framed, Partially buried	Slight	Slight
37	1,000-ton Clear Water Tank, Dong-Shi Water Treatment Plant	Non-framed, On-grade	Extensive	Complete
C	Yi-Jiang Water Pipe Bridge	Simple pipe, Conventionally designed	Complete	Complete

Acknowledgements

Research funding from the Water Resources Agency, MOEA, under Grant MOEA-WRA-1040264, and assistance from the Taiwan Water Corporation and its 4th Branch in providing an inventory of water facilities and information regarding damage during the Chi-Chi earthquake are gratefully acknowledged.

References

- FEMA (Federal Emergency Management Agency) (2010), "Multi-Hazard Loss Estimation Methodology: Earthquake Model", HAZUS-MH MR5, Department of Homeland Security.
- 交通部公路總局, 2008, 「公路橋梁耐震能力評估及補強工程可行性研究」期末報告, 台灣世曦工程顧問股份有限公司, 台北。
- 洪祥瑗、文慶霖、柯明淳、劉季宇、葉錦勳, 2007, 「自來水地下管線、輸電鐵塔與震後火災之災損推估模式研究」, 國家地震工程研究中心研究報告, 編號 NCREE-07-020。
- 經濟部水利署, 2015, 「公共給水系統震災風險評估技術之研究」研究報告, 計畫編號 MOEA-WRA-1040264, 台北。

Reconstruction of Geographic Information System Module

Cheng-Tao Yang¹, Chin-Hsun Yeh² and Chi-Hao Lin³

楊承道¹、葉錦勳²、林祺皓³

Abstract

The study aims to reconstruct a kernel Geographic Information System (GIS) module of Taiwan Earthquake Loss Estimation System (TELES). TELES has integrated many analytical models and databases, including geology, bridge, building, and water system. The current GIS module is limited by file-size capacity and does not support parallel computing architecture. Seismic loss estimation requires considerably more computer resources with growing database size and increasingly complex models. Therefore, development of the new kernel module, named Geographic Information & Novel Notion Yolk (GINNY) had started since 2015. The new module is expected to improve computational efficiency and to extend file-size capacity. GINNY now is still in the development phase and is scheduled to be completed by 2017. In this report, the technologies for constructing GINNY will be first reviewed. Then, the requirement analysis, the design concept, and the current development progress of GINNY will be stated briefly.

Keywords: Geographic Information System, Earthquake Loss Estimation, Parallel Computing

Introduction

The National Center for Research on Earthquake Engineering (NCEE) has developed an earthquake loss estimation system in Taiwan, named "Taiwan Earthquake Loss Estimation System (TELES)" since 2003 (Yeh, 2003). TELES integrates various databases in a geographical information system (GIS) to simulate the distribution of ground shaking intensity, ground failure probability, building damages, casualties, post-earthquake fires, debris, lifeline interruptions, economic losses, etc. It has been successfully implemented in various seismic risk management practices in Taiwan. The current GIS module does not support parallel computing architecture, and is limited by file-size capacity. However, seismic loss estimation requires more computer resources with growing database sizes and increasingly complex models. Therefore, the development of a new GIS module, named Geographic Information & Novel Notion Yolk (GINNY) was started in 2015. The new module is expected to improve computational efficiency and extend file-size capacity. GINNY is still in the

development phase and scheduled to be completed in 2017. In the first section, the software technologies used to construct GINNY will be reviewed. The following sections will present the requirement analysis, the design concept and the current development progress of GINNY. The software technologies related to GINNY, including object-oriented technology, Shapefile, SpatiaLite, MapWindow GIS (MapWinGIS), and Quantum GIS (QGIS), are briefly stated below. More detail about these technologies can be obtained via search engines such as Google. This report discusses the features that are essential for GINNY.

1.1 Object-Oriented Technology: GINNY is developed using object-oriented technology. Based on the user experience in recent years, and the desired efficiency for the growing volume of data, the requirement of GINNY was analyzed at first. Based on the requirement analysis, the concept design and the prototype of GINNY was implemented to verify its feasibility. Compared with procedure programming, object-oriented programming is easier to understand as it is clearer how various objects collaborate to

1 Associate Researcher, National Center for Research on Earthquake Engineering

2 Researcher, National Center for Research on Earthquake Engineering

3 Assistant Researcher, National Center for Research on Earthquake Engineering

construct a software system, and how messages are exchanged across the objects. In the next section, OOT is adopted to explain how GINNY interacts with the interface of existing open software libraries and build its specific features.

1.2 Shapefile: Shapefile is developed by Environmental Systems Research Institute (ESRI) and is a popular format to store geospatial vector data for GIS. In Taiwan, almost all geospatial data, such as the digital road network, specific addressed location, and disaster potential map, are provided in the shapefile format. Hence, the shapefile is set as the input and output standard of GINNY. The term “shapefile” actually refers to a collection of files with a common file prefix, stored in the same directory. It mainly uses three extensions: shp, shx, and dbf files.

- .shp - contains feature geometry.
- .shx - contains shape index.
- .dbf - contains attributes.

In recent years, to cope with the coordinate system and projection information, and to specify the character encoding code, two extension files, .prj and .cpg, have also been included.

- .prj – defines coordinate system and projection information.
- .cpg - specifies the character encoding code.

In Taiwan, three geographic datums, i.e. TWD67, TWD97, and WGS84, are commonly used, which sometimes causes confusion. Moreover, there are more than two Chinese character encoding codes, such as the big5 and the utf8. To deal with the confusion due to various coordinate systems and Chinese character encoding codes, prj and cpg extensions are also regarded as essential components of the shapefile for GINNY along with the three main extensions.

1.3 SpatiaLite: SpatiaLite provides vector geospatial database functionality. It extends Sqlite’s existing spatial support to cover the Simple Features Access Standard (SFS) of Open Geospatial Consortium (OGC). It is applied as an essential part of GINNY due to its three features. (1) The whole SQL engine is directly embedded within the application itself. The database is simply a single file which can be freely copied (or even deleted) and transferred from one computer/OS to another without any special precautions. This feature helps simplify the installation process and geospatial data exchange in GINNY. (2) SpatiaLite provides in-memory-database operation. It might store the whole database in the memory in some circumstances. Using SpatiaLite, the efficiency bottleneck of hard drive input-and-output

can be ignored to develop parallel algorithms because it is not necessary to obtain any information from the hard drive. (3) Virtual-Shapefile table: SpatiaLite supports a Virtual-Shapefile driver. It has the capability to provide a SQL query for an external Shapefile. It uses very little computer resources to obtain query results from across multiple Shapefiles with no need to load any data.

1.4 MapWindow and QGIS: MapWindow and QGIS are both open-source desktop software applications of geographic information systems. These applications are adopted as the geographic map view-manage toolkit. MapWindow was developed on the Microsoft Window Environment. Due to its Compatibility with the graphic-user-interface of TELES, MapWindow is adopted as the map view-manage of GINNY at the prototyping stage. QGIS (previously known as Quantum GIS) is a cross-platform desktop application with a software instance on Microsoft Window Environment. In addition, QGIS supports data manipulation and analysis in Shapefile and SpatiaLite formats.

2. Requirements analysis

The requirements of GINNY can be divided into two groups, basic features and customer-specific features. Basic features describe the basic function of a geographic database, and customer-specific features state the specific need from experience of users and developer.

2.1 Basic features

GINNY is expected to have the basic features of a spatial database. The first key feature is to store spatial data and to manage geometric objects. GINNY should at least allow representation of simple geometric objects such as points, lines and polygons. In addition to typical SQL queries, GINNY is also expected to perform spatial queries and geometric operations. Spatial queries include “compute line length or the distance between geometries”, “allow true/false queries about spatial relationships between geometries”, etc. Geometric operations include “create new geometries”, “combine existing geometries into one geometry”, “modify existing features to create new ones, for example, by providing a buffer around the specific geometries”, etc. At last, Consistency-Check of datum (spatial coordinate system) is also a key feature of GINNY. In Taiwan, three datums, i.e. TWD67, TWD97, and WGS84, are commonly used. Geographic data based on various Datum often cause confusion because some geographic files do not contain datum information. Therefore, GINNY needs a Consistency-Check operation when loading geographic files to prevent datum confusion.

2.2 Customer-specific features

User-Friendly Software Framework: The software framework of GINNY should consider the needs of TELES customers such as government officials, postgraduates, firefighter, and rescuers. These customers are not necessarily trained in GIS technology. Therefore, the installation and configuration of any derived software should be as simple as possible, and geographic data should be exchanged and managed as conveniently as possible.

Concise Application Programming Interface: In general, a database provides four essential functions to manage data, which are view, table, index, and trigger. Beside the four functions for internal data, GINNY should also have other functions to read and to analyze external data such as Shapefiles, dbase-files, and csv-files. GINNY needs a good object-oriented design to simplify the process of manipulating all geographic data from various sources or files.

Compatibility: The current version of TELES was developed as a Microsoft Windows application, and its graphical user interface is implemented based on Microsoft Foundation Classes. The new kernel module should consider the compatibility of the current graphical user interface so as to carry out the installation of new software extensions smoothly for existing customers.

High Performance Computing: Finally, GINNY should also have the potential to support parallel and distributed computer architectures in order to cope with the growing size of the database and increasingly complex models.

3. Design and Prototype

Based on the requirement analysis as stated above, a conceptual software framework of GINNY has been designed as shown Fig. 1 and Fig. 2.

3.1 Virtual-Shapefile

A virtual-shapefile table is adopted as the bridge to standard geographic file of GINNY. The original Shapefile does not actually support spatial queries. However, using the virtual-shapefile table of SpatiaLite, GINNY has the extension capability to query spatial data from all Shapefiles, which are considered as geographic database tables as shown in Fig. 1.

3.2 Alias manage interface

To standardize management functions of various data sources such as Virtual tables (Shapefile, dbase file), a software facility, named “Alias”, has been implemented as shown in Fig. 2. The “Alias” provides the same application programming interface to manage geographic data and attribute data, no matter what format or source they are in.

3.3 Prototype Implementation

A GINNY prototype has been developed using the C++ programming language based on the concept software framework. As shown in Fig 3, by integrating GINNY with SpatiaLite and MapWinGIS, a simple window application instance has also been implemented. The window application involves three major GUI for manipulating geographic data: a tree panel for viewing/querying the geographic database table (left part of Fig. 3), a geographic map (middle part), and a list panel for vector layers (right part). The prototype windows instance shows the compatibility and feasibility of the GINNY framework design.

Conclusions

In this report, a software requirement analysis was carried out and a conceptual software framework of geographic information system module, named GINNY, has been proposed. A prototype of GINNY and a windows application instance have also been developed to verify the compatibility and feasibility of the GINNY framework design. These are essential for building a new geographic information system module with more efficiency and capability for big geographic data regarding seismic loss estimation.

References

- Yeh, C. H. (2003), Taiwan Earthquake Loss Estimation System - TELES, Technical Report NCREC 03-002, National Center for Research on Earthquake Engineering, Taipei (in Chinese).

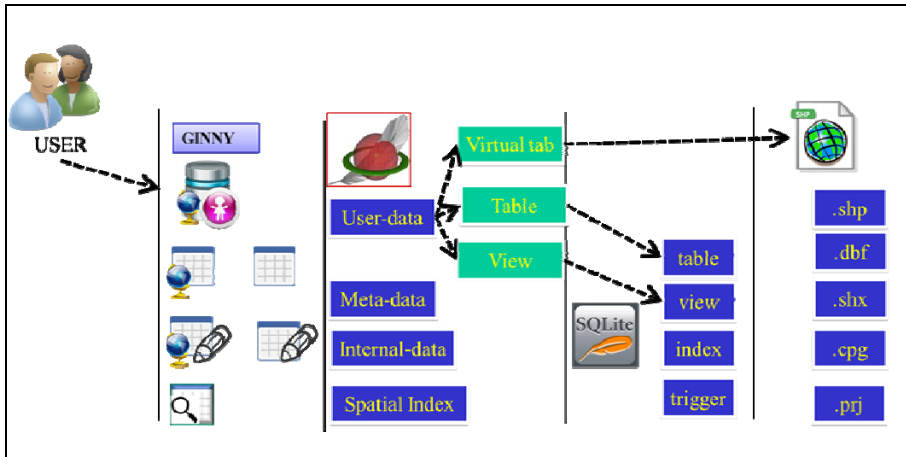


Fig 1. Concept Framework of GINNY

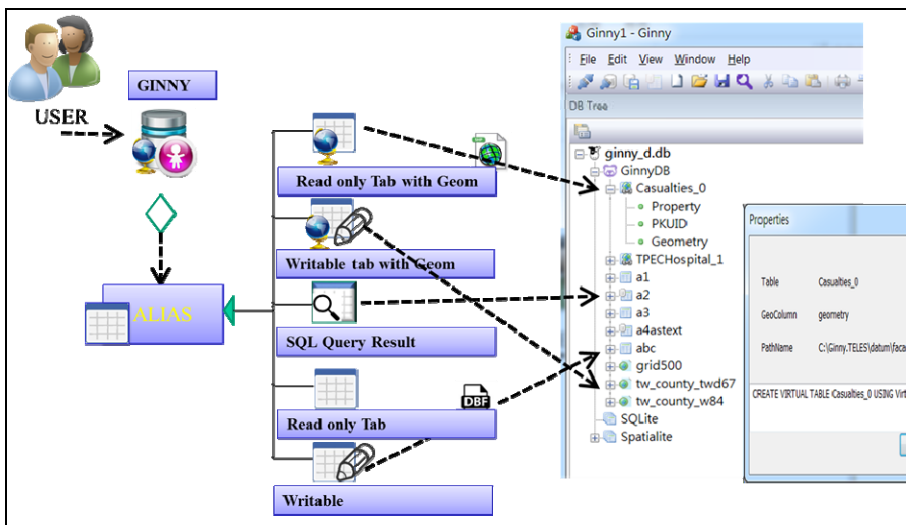


Fig. 2. Application Programming Interface of GINNY

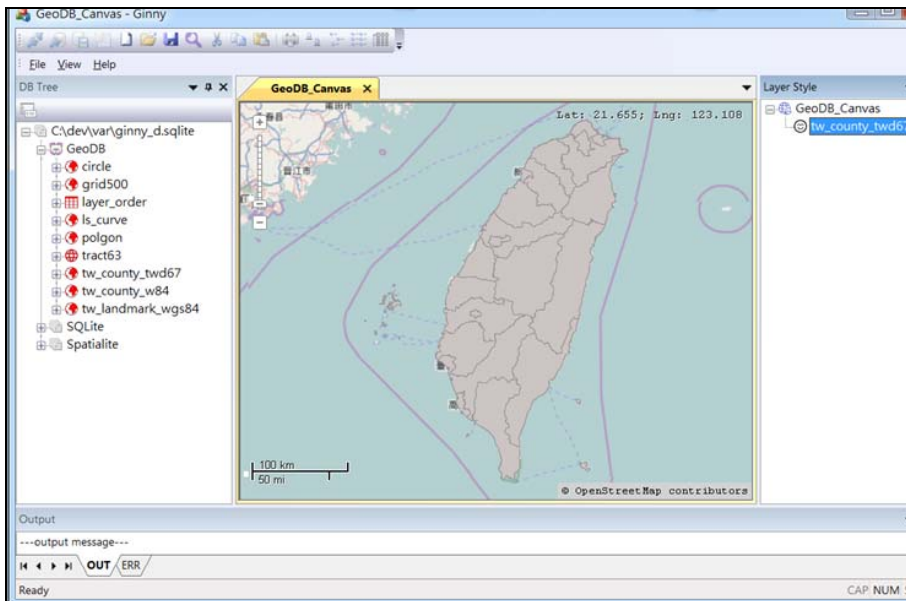


Fig. 3. A Simple GIS software instance based on GINNY